Tsunami induced failure of bridges

Determining failure modes with the use of SPH-modeling

J.T. Salet

Master of science

Tsunami induced failure of bridges

Determining failure modes with the use of SPH-modeling

by

J.T. Salet

Student number:	4225066	
Project duration:	September 3th, 2018 – July 15th, 2019	
Thesis committee:	Dr. ir. J. Bricker,	TU Delft, Chairman
	Dr. ir. Y. Yang,	TU Delft
	Dr. ir. A. Antonini	TU Delft
	Ir. N. Kostense,	Arcadis
	Dr. Ir. T. Suzuki	Flanders Hydraulics Research

TU Delft

ARCADIS Design & Consultancy for natural and built assets

Preface

This thesis is the conclusion of the master of science program in Hydraulic Engineering at Delft University of Technology. The research was conducted in a period of ten enjoyable months in which a lot of knowledge was gained and many activities have been conducted to full-fill the process of graduating.

First of all I wish to thank the chair of my assesment comittee, Jeremy Bricker, who I wrote an email to in which I expressed my interest and enthusiasm in hydraulic structures and tsunami's one year ago. It resulted in a great year, where Jeremy Bricker functioned as my daily supervisor from the TU Delft and was always available for in depth theoretical questions as well as for guidance on who to involve in the thesis and what decisions had to be made to continue on the right track. Thank you for the many valuable lessons you teached me in Otsuchi, Vlissingen and of course in Delft.

In September 2018 a group of multidisciplinary students went on a trip to Otsuchi, Japan with the goal of learning from the reconstruction of Otsuchi town which was severely damaged by the 2011 Tohoku tsunami. Thanks a lot for giving me the opportunity to be a part of this kind and inquisitive group of people. For this period i want to thank in particular Mio Kamitani who arranged a lot of very interesting meetings in and around Otsuchi which made the trip as interesting as it was. Of course, thanks to all the supervisors for their in depth knowledge and anecdotes which made it the valuable experience it was. The funding for the trip was provided by the Delft Infrastructure and Mobility initiative (DIMI).

After the Otsuchi trip there was a possibility for me to do physical tests at the Waseda university in Tokyo. With the help of Waseda university students, from who I want to thank Go Hamano and Hidenori Ishii especially for their unlimited patience. Also the guidance of Professor Shibayama, Miguel Esteban and Tokoyuki Takabatake were of great worth.

The writing and modeling part of this thesis is conducted in the Netherlands at Arcadis, one of the leading engineering and project management consultancies in the world. Here I got the expert supervision of Niels Kostense, whose daily supervision and guidance throughout the entire process of the research was of unmeasurable worth. I would like to thank Arcadis for providing an excellent working space and learning environment. Many thanks to my temporary colleagues at Arcadis and my fellow graduates at the TU, for the inspirational conversations and occasionally for the welcome distraction

Without the help of Tomohiro Suzuki, who is also a member of my assesment committee, and Corrado Altomare from Flanders Hydraulics Research I would never have been able to take my first steps in the SPH model of DualSPHysics. For which I am very grateful.

The continuation in this research in the form of a journal paper including 3D models of this thesis have been realized with the most compassionate Alessandro Antonini. Who despite the knowledge of my timepressure helped me going in the right direction with clear steps ahead of me.

From a concrete structure point of view there could be some interesting follow up thesis topics. Unfortunatly this theses lacked the in-depth calculation of concrete elements. Despite this, Yuguang Yang who is the last member of my assessment committee was always motivated to help me with problems and come up with interesting proposals to get my thesis at the level it became.

Last but not least, I want to thank all the people who supported me and played a role in forming me in to the person that I am today. To all my friends, many thanks for the great times we had and I hope shared memories will still be created. I want to thank my parents, Jack and Lily, and sister, Nienke, whose unlimited support and love helped me through all the tough moments.

Jesse Salet
Delft, July 2019

Abstract

Recent major tsunami events generated by earthquakes inundated coastal cities and caused extreme destruction and loss of human lives. The collapse of coastal bridges due to tsunami wave impact represents a huge obstacle for rescue works. The need to understand tsunami effects and develop tsunami-resilient bridges became apparent in the aftermath of extreme tsunami events in the Indian Ocean (2004), Chile (2010) and Japan (2011).

Different coastal topographies affect tsunami propagation near shore. Varying wave characteristics lead to various failure mechanisms of bridge decks. Together with the wave characteristics, the bridge properties and the settings around the bridge play a major role in this failure, think for example of shear keys, seawalls or inclination of the bridge.

To find out more about these failure mechanism and what role all these measures have in the failure, a laboratory experiment is executed and a numerical SPH model is set up to investigate the impacts of various wave characteristics, a seawall, shear key and inclination of the bridge deck. The numerical SPH model is validated with the help of wave gauge data and tracked bridge deck movement from the executed physical tests.

In this thesis the focus is on the movement of the bridge deck, what kind of effect do the different interventions have on the movement of the deck. Since the movement is highly dependent on the forcing on the bridge deck, the forces are analyzed thoroughly. From the force time series countermeasures are proposed and modeled in the SPH model.

Wave forces from different type of waves are simulated with the SPH model. The overall behavior of the hydrodynamics and the deck movement are validated and suited for qualitative analysis. Some disadvantages of the model are the lack of bottom friction and air bubbles in turbulent regions. The 3D model represented the movement on the deck in a very good way, runtimes and storage capacity formed an obstacle. A 2D model was used to do qualitative analysis of the changes of wave characteristics and the effects of the structural measures. The limiting factor in the commercial use of SPH is the computation time. In future models this could be accelerated by the use of GPU processors instead of CPU processors which are able to solve many parallel processes at the same time.

Apart from wave heights and inundation heights, the wave phase appeared to be a major decisive factor in the failure method of the bridge deck. If the wave breaks near the shore and reaches the bridge structure as a propagating wave front, the hydrodynamic situation results in high horizontal forces and a sliding failure mode is apparent. When a wave is still in a surging phase and the fluid particles still have their rotational movement, the dominant forcing on the bridge is in vertical direction. Since the vertical force applied to the bridge deck moves from seaside to shore side, the sea side of the bridge deck has a higher vertical velocity which initiates rotation. A seawall causes the water to confine underneath the bridge deck. Which will result in higher vertical forces, thus a rotational failure mode follows. Inclination of the bridge deck has significant effect on the vertical forcing. Positive inclination lead to a decrease of upward forcing and negative inclination lead to an increase of upward forces. The introduction of shear keys resulted in higher moments, since the point of rotation is set at the point the deck interacts with the shear key, which creates a larger distance around the point of rotation.

Possible countermeasures that are introduced are a sacrificial beam and a different geometry of the deck. A sacrificial beam was effective in lowering the total horizontal forces on the combined structures. The deck itself was not exposed to a high horizontal impact force. Different geometries are tested to see how the forces on the structure would chance. A wing shaped geometry has positive effects in mitigating the horizontal forces on the bridge deck.

Contents

List of Symbols

a	acceleration	m/s^2
A	surface Area	m^2
A_{bear}	plan area of the bearing	m^2
b_l	element length	m
b_w	element width	m
b_w	smallest web width	N
b_h	element height	m
C	wave celerity	m/s
c_l	clearance height between water level and deck	m
C_D	drag coefficient	-
CDV	empirical downward vertical force coefficient; 0.53	-
CUP	empirical uplift force coefficient; 0.77	-
C_L	lift coefficient	-
C_s	slamming coefficient	-
C_M	moment coefficient	-
$C_{Rk,c}$	coefficient derived from test (0.12)	-
C	coefficient between 1 and 2	-
Cvs	slamming coefficient in the vertical direction; 2.0	-
d	effective height of cross section	m
d	water depth	m
f_{ck}	characteristic concrete compressive strength	N
F	force	N
F_b	buoyancy force	N
F_D	drag force	N
F_i	inertia force	N
$FHmax$	maximum horizontal force	N
$FDVmax$	maximum downward vertical force	N
$FUPmax$	maximum uplift force	N
F_e	dynamic loading which reflects the loading characteristics and the deck response	N
Fh_hs	hydrostatic horizontal force	N
Fv_s	slamming vertical force	N
Fv_hs	hydrostatic downward vertical force	N
F_L	shear deformation	N
F_L	lift force	N
Fr	Froude number	-
F_s	$F_e * F_s$	N
F_v	vertical force	N
F_z	plan area of the bearing	N
g	acceleration of gravity	m/s^s
G	shear modulus of the elastomeric material	N/m^2
h	free-surface elevation	m
$h*$	inundation ratio	m
$h0$	difference between the tsunami water free-surface elevation and low chord of the bridge	m

h_u	water height	m
h_b	deck height	m
H	wave height	m
H_D	horizontal force against the bearing	N
$H_{max,F}$	horizontal capacity of the bearing (friction failure mode)	N
k	size factor = $1+\sqrt{(\frac{200}{d}}$	m
L	length of the structure	m
L	wave length	m
Lb	height of the bridge barrier	m
Lh	height of the bridge superstructure	m
Lsb	effective length of the bridge deck for a vertical slamming force; 4 × Lb	m
Lv	width of the bridge superstructure	m
Lg	height of the bridge girder	m
L_F	length of full scale model	m
L_M	length in the model	m
M_{cg}	moment around centre of gravity	Nm
p_{hyd}	hydrostatic pressure	Pa
p	maximum slowly changing pressure on the bottom of the plate	Pa
P	uplift pressure at impact	Pa
Pr	proximity ratio	-
S	thickness of deck	m
t	time	s
t_b	thickness of the bearing	m
t_d	duration of the impact loading	t
Td	thickness of the bridge deck	m
T_n	natural period of the deck	s
u	horizontal fluid velocity in wave crest	m/s
U	velocity of the fluid with respect to the object	m/s
v	Velocity	m/s
v	vertical water particle velocity	m/s
$\frac{\delta v}{\delta t}$	vertical water particle acceleration	m/s^s
V	volume of the structure	m^3
W	wetted width of the structure	m
W	width of the bridge	m
Wn	Weber number	-
x	position	m
z	deck height above the standing water line	m
$Z0$	low chord elevation of the bridge superstructure	m
Δx	shear deformation	m
η	elevation of the crest of the wave	m
η_{max}	maximum crest elevation	m
μ	friction factor between elastomeric material and mating surface	-
μ	dynamic viscosity of the fluid 0.001	$N*s/m^2$
ν	kinematic viscosity of the fluid	m^2/s
ρ	density	kg/m^3
ρ_l	longitudinal reinforcement ratio (=<0.02)	-
ρ_w	density of water	kg/m^3
σ	surface tension	N/m

In the lab tests and numerical tests the notation for the cases is done as d60h30 in which 60 is the water level in the tank in cm and 30 is the water level in the basin in cm.

1 Introduction

1.1. Background

Recent major tsunami events generated by earthquakes in the Indian Ocean (2004), Chile (2010) and Japan (2011) inundated nearby coastal cities causing extreme destruction and loss of human lives. The tsunami waves inundated a large number of bridges, damaged the connections of the superstructure to the substructure in many cases and washed away complete bridge decks [Kawashima, 2012]. In the aftermath of these disastrous events, the need to understand tsunami effects and develop tsunami-resilient bridges became apparent. Apart from earthquake-induced tsunami's, climate change leads to uncertainties in precipitation and storm patterns throughout the world. Extreme events like floods and storm surges appear more frequent which results in the collapse of bridges near rivers and coastlines [Istrati et al., 2017].

The 2011 Tohuku tsunami on the east coast of Japan resulted in more than 15,000 fatalities, missing more than 2,500 people and a total monetary loss accounted for $235 billion. The collapse of coastal bridges due to tsunami impact poses a major obstacle for rescue works. The 2011 Tohuku tsunami caused extensive and severe structural damage to various parts of infrastructure in north-eastern Japan. Especially in the coastal area of Iwate, Miyagi, Fukushima and Ibaraki prefectures, more than 250 bridges washed away. For example, Utatsu Bridge at Minami-Sanriku Town over Irimae Bay suffered extensive damage by a tsunami as shown in Figure 1.1 [Salem et al., 2014].

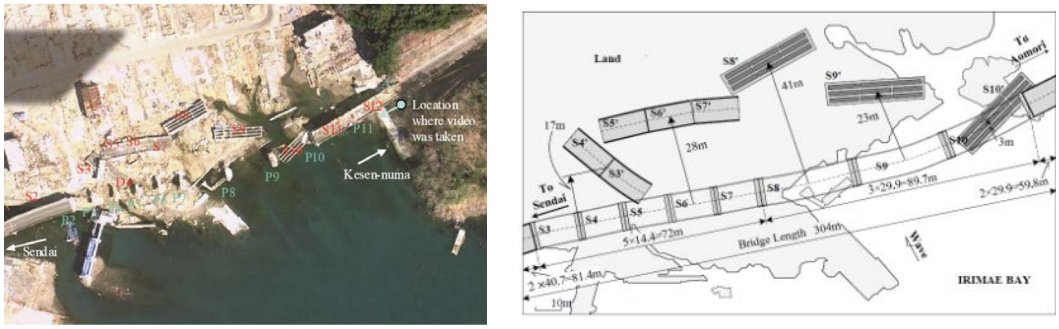

(a) Google earth

(b) Schematic

Figure 1.1. Utatsu bridge collapse [Salem et al., 2014].

As shown in the above figures the individual bridge decks all have different failure mechanisms. Possible factors that play a role in the failure of these superstructures were: inclination of the bridge, presence of a seawall and air entrapment between the girders which caused extra buoyancy forces on the bridge [Bricker and Nakayama, 2014].

Some studies have examined the thresholds of failure. However, little is known on the different failure mech-

anisms that occur. In Figure 1.2 the bridge sliding of its piers is visible and Figure 1.3 indicates that the superstructure has been lifted over the unseating prevention devices (UPD) since these are still intact.

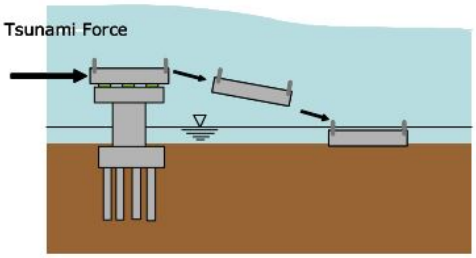

Figure 1.2. Transverse drag [Kawashima and Matsuzaki, 2012].

Figure 1.3. Bridge uplifted before lateral movement [Bricker and Nakayama, 2014].

In Figure 1.2 the main failure mechanism is sliding, which is caused by a large horizontal force. In Figure 1.3 it can be seen that apart from the horizontal force a vertical force must have been present at the moment that the bridge started moving. It is clearly visible that the bridge superstructure has made a vertical movement over the UPD's since these are not damaged. After a bridge deck makes a vertical movement it is likely that a rotational movement will follow before its final destination is reached.

Failure of bridges due to flood or tsunami damage can have multiple reasons. First, scour around the foundation of the bridge piers which causes the complete bridge structure to tumble over. Second, high water velocities around the bridge piers which cause significant forces that push over the whole structure. Third, debris colliding with the bridge during flooding events. Fourth, immerse pressure when the bridge is partly or fully submerged. Fifth, wave or tsunami forces on the piers or the decks when fully or partly submerged.

Generally speaking, two main bridge failure mechanisms are observed during tsunamis. First, failure of the connections attaching the bridge superstructure (i.e. the bridge deck and supporting girders) to the bridge substructure (i.e. the bridge piers and/or abutments). Second, scour around bridge abutments and supporting piers, failure of the foundation, failure of the bridge piers and failure due to debris impact [Lomonaco et al., 2016]. In this study, only the mechanisms inducing the first type of failure are examined.

Main causes of substructure failure are embankment settlement and scouring around the bridge piles [Lomonaco et al., 2016]. Regarding the failure of superstructures, failure is subscribed from the partial displacement of bridge decks to complete failure of decks where decks are dragged away hundreds of meters from its original location. The magnitude of these damages is related to both hydraulic characteristics and the bridge geometry. The focus of this thesis is on the failure of the superstructure of bridges and their failure mechanisms due to tsunami waves. Collapse of bridges due to scour near the foundation is out of the scope of this research.

Recent research of [Oudenbroek, 2018] indicates that the scale model of a bridge, in which the deck and piers were connected, did not collapse under any hydraulic conditions tested in that research. Even in the most extreme cases where a significant amount of debris was lodged against the bridge, no collapse was indicated. Instead, the bridge deck must have failed first, followed by the bridge piers.

1.2. Research significance/motive for this research

The failure of bridges often has a great effect on the transportation system of a region. In areas where disasters happen and bridges are collapsing, people need to evacuate and especially in the first aid phase after a disaster it is important for the rescue works to arrive at the location rapidly [Yim and Azadbakht, 2013]. The 2011 great east Japan earthquake and resulting Tohoku tsunami impacted more than 300 bridges along the Japanese coast, about 50% were destroyed and washed away. According to the post-tsunami surveys,

most of the bridges survived the earthquake but were completely destroyed by the tsunami, indicating that the current bridge design specification cannot provide bridges with sufficient strength to resist the tsunami loads [Yim and Azadbakht, 2013]. Historical reports of modern-design bridge damage and destruction by tsunamis can be found. This indicates that, in spite of the awareness of the problem, there is a lack of full understanding of the process and the difficulties in the implementation of design codes and recommendations for constructing tsunami-resilient bridges, particularly since some communities are vulnerable to tsunamis, although do not necessarily belong to a seismic hazard zone.

The behavior of bridges under the action of hurricane waves and storm surges has been studied over the past years, but fewer studies are present regarding tsunami loading and the dynamic response of the bridge superstructure. So far, the performed studies have covered on-site surveys analyzing the failure mechanisms, small-scale experiments with rigid bridge models, or numerical model simulations with limited validation where the bridge dynamics might not be included [Lomonaco et al., 2016]. Most of this work is done to discover the forces generated by the tsunami on the bridges. Not much research is done on the movement of the bridge superstructure. Therefore, in this research, the bridge will be modeled in Smoothed Particle Hydrodynamics (SPH) software in which the movement of the bridge deck can be simulated in a realistic manner.

A lot of factors play a role in the failure of the bridge superstructure, for instance, lateral restrainers, shear keys, seawalls, air entrapment, inclination of the deck, inundation factor, incoming debris impact, turbulence intensity, etc. Though for time limiting reasons only three factors will be examined in this research which will be the effects of a seawall, inclination and shear keys.

1.2.1. Otsuchi project

At 14:46 local time on March 11, 2011, a magnitude 9.0 earthquake occurred off the coast of northeast Japan. This earthquake generated a tsunami that struck Japan as well as various locations around the Pacific Ocean. With the participation of researchers from throughout Japan, joint research groups conducted a tsunami survey along a 2000 km stretch of the Japanese coast. More than 5300 locations have been surveyed to date, generating the largest tsunami survey dataset in the world. On the Sendai Plain, the maximum inundation height was 19.5 m, and the tsunami bore propagated more than 5 km inland. Along the ria coast from about 50 to 200 km north of Sendai, the narrow bays focused the tsunami waves, generating the largest inundation heights and run-ups. The survey data clearly show a regional dependence of tsunami characteristics [Mori et al., 2011].

The highest inundation levels in Otsuchi reached up to 22 meters. Two bridges in Otsuchi were destroyed by the tsunami. These bridges were located over the northern Otsuchi river, in which the Tsunami propagated severely. The Kozuch river, the southern river through Otsuchi, was protected by a barrier. This barrier was destructed by the tsunami but the bridges in this river experienced less damage.

According to a report by the Japan Bridge Association (JBA), 190 bridges out of the total surveyed 3,004 bridges in the area affected by the tsunami (i.e., 6% of the total) required some sort of treatment to remain operational, and 299 bridges (10%) were judged to require repairs to restore their load resistant capacity [JBA, 2011].

1.3. Research objective

The main objective of this research can be defined as follows:

Determine tsunami-induced failure mechanisms of bridge decks using SPH simulations

Research sub questions:

- Is smoothed particle hydrodynamics (SPH) an adequate way for analyzing tsunami-induced failure of bridges?

    - Can 2D SPH models simulate 3D effects accurately?

- What are the failure modes of a bridge deck with different tsunami wave impact loads and what is the effect of shear keys, inclination or seawalls?

- Based on the results of the SPH simulations, what kind of countermeasures can be proposed to prevent the failure mechanisms of a bridge deck due to tsunami waves?

The main research question emphasizes on tsunami-induced failure modes of bridge decks using SPH modeling. The first question that will be answered is: Is SPH a good way for analyzing tsunami-induced failure of bridges. A 2D model will be validated with the lab tests that are done at the Waseda university explained in Chapter 3. The sub-question is important since the 3D SPH models are computationally expensive to use, it would be more beneficial if the results from the 2D models can be used to analyze the failure modes of the superstructure.

The main research question will be the failure modes of the bridge deck. If the 2D model gives consistent results, these models can be used for the determining of the failure modes. The shear keys, inclination and seawalls are subsequently modeled in 2D to evaluate the performance.

The last research question is based on the results of the first and main objective of this thesis. If the failure modes are known, countermeasures are proposed to withstand the critical values of the wave forces.

1.3.1. Project outline

In this thesis the focus is on describing the waves that can be reproduced in a dam break-underflow test. The piers are assumed to be fixed in all cases, which is crucial for this study. It should be verified in later research if the foundations of bridges could withstand the forces that are assumed in these situations.

1.4. Research outline

The main objective of this thesis is to find the failure mechanisms of a slab-girder bridge deck which is subjected by an underflow dam break, in addition, adequate measures that can prevent these types of failure mechanisms are proposed. The following list displays the order of activities that are performed to attain conclusions and recommendations.

1. Laboratory experiments at Waseda university in Tokyo (Chapter 3)
2. Literature study (Chapter 2)
3. Modelling using an SPH model (Chapter 4)
4. Validate model by using the laboratory experiment data (Chapter 4)
5. Analyse the data from the numerical model (Chapter 5)
6. Study existing and new solutions for the lateral movement of the bridge deck (Chapter 6)
7. Model the suggested solutions, see what works best. (Chapter 6)
8. Study the feasibility of the proposed solutions. (Chapter 6)

The model that will be constructed will be similar to the bridge scale model that is used in the laboratory experiments for steady-flow stability of bridges [Oudenbroek, 2018]. This means that this research is limited to the three-girder bridge that is used in the experiment. Different variations on the standard bridge layout, namely shear keys and inclination of the deck will be studied.

Softwares which will be used to built the numerical SPH model are LS-Dyna and Dualsphysics. The model is constructed in such a way that it is similar to the flume which is used in the Waseda University to simulate the tests in this flume. These models are validated with data from the laboratory tests performed at the Waseda University in Tokyo.

After the 2D model is validated, the 3D model can be constructed. The important aspects, in this case, are the 3D effects around the piers. No measurements of forces have been done during the laboratory tests so this model can only be validated on a qualitative manner by the movement of the bridge deck.

2

Literature study

2.1. Preliminary research

Structural response of bridges to wave impact loading is influenced by various bridge parameters and also to the tsunami parameters at different bridge sites. This includes the hydrodynamic characteristics that determine the horizontal and vertical forces on the bridge as well as structural characteristics of the bridges such as span, height, weight of the girders, type of barrier rail, etc.

Preliminary to the start of this thesis, research is done in this field of work. Research has been done in a 2D numerical Ansys-Fluent model with a fixed deck by [Naderi, 2018]. In [Naderi, 2018] the focus is on the forces which are applied by a steady flow on submerged bridge decks due to strong currents. This reassembles waves with large wavelengths like tsunami's.

Physical model tests have been performed to study the effects of steady flow during river floods on bridge failure mechanisms and the effect of accumulating debris in front of the bridge by [Oudenbroek, 2018].

During the 2011 Tohoku tsunami in Japan, a large number of bridges failed in the coastal area which were hit by the tsunami. The Utatsu highway bridge was located 6.6m above the mean sea level. The unseating prevention devices were still intact and the displaced bridge decks were upside down on the landward side of the piers displayed in Figures 1.1 [Salem et al., 2014; Bricker and Nakayama, 2014]. This indicates that the bridge deck must have been rotated off its piers.

In the case of the Utatsu bridge, multiple parameters played a role in the failure mechanism of the bridge: inclination, the presence of a seawall, shear keys and the presence of air pockets underneath the bridge. In this case, the bridge failed by a long surging wave. These kinds of waves do not have a bore and no peak force is applied to the bridge. As a result, failure is subscribed to the high flow velocities of the water.

2.2. Variables effecting fluid-Deck interacting

2.2.1. Bridge types

In practice, various bridge types in different locations have different geometries. The Utatsu bridge is a girder slab bridge and the air entrapment underneath the bridge was an important factor for the uplift forces on the superstructure [Bricker and Nakayama, 2014]. The previous research with the physical model a slab-girder bridge is used [Oudenbroek, 2018]. These type of bridges often have a large total thickness. In the Netherlands, the challenge is to build bridges as slender as possible for economical and practical reasons. Therefore, in the Netherlands, also box girder bridges are often applied. This type of bridge has a hollow core. The most common bridge types are displayed in Figure 2.1. In Japan, the area which is prone to tsunami hazards, a girder slab type of bridge geometry is more common.

For hydrodynamic forces and buoyancy forces around a bridge superstructure, the bridge type is of importance. Boxed girder bridges are more sensitive to buoyancy forces during floods. In this study, only a three-girder-slab bridge is examined.

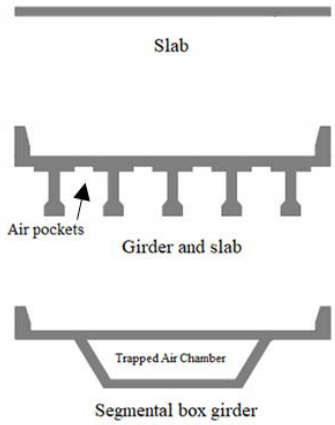

Figure 2.1. Three common bridge superstructure shapes [Naderi, 2018].

2.2.2. Wave impact

In research related to tsunami impact on coastal structures [Bricker et al., 2015], it is explained what the effects of tsunami waves on a slab girder bridge are. In this case study, the Hirouchibashi concrete girder bridge was used.

The results of the described scenario is shown in Figure 2.2. In this case, the deck is initially exposed above the water and a wave of 2m height with a flow speed of 5m/s approaches the bridge. According to the experimental study of [Hiraki et al., 2011] on wave forces on bridge decks, this is a situation where large vertical forces can occur. It is observed that a large upward force and overturning moment are built up when the wavefront impinges on the bridge deck from approximately t 0.6s to 1.2s. The force plots in Figure 2.3 show several peaks corresponding to the instances when the wave impinges on each of the four individual beams and the bottom surface. It should be noted that the air in the cavities between beams is assumed to be connected to the atmosphere and the pressure there is assumed to be atmospheric. The uplift force takes a maximum value at the second peak and the overturning moment reaches the weight momentarily. However, the uplift force gradually reduces and becomes slightly negative if t is 3.0s when the water starts to flow over the top surface of the deck (see t = 3.0s in Figure 2.2). This behavior of the lift force is consistent with the experiment of [Hiraki et al., 2011]. The horizontal force exceeds the static friction force during the two large peaks, but the present fluid-structure interaction analysis indicates that these will not initiate motion of the bridge deck itself.

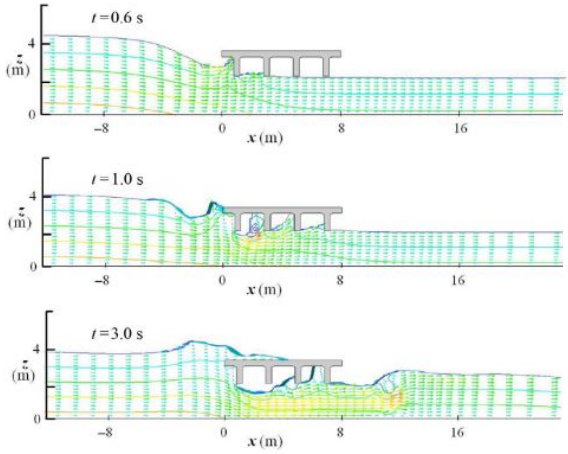

Figure 2.2. Tsunami impact on bridge deck h=2m v=5m/s [Bricker et al., 2015].

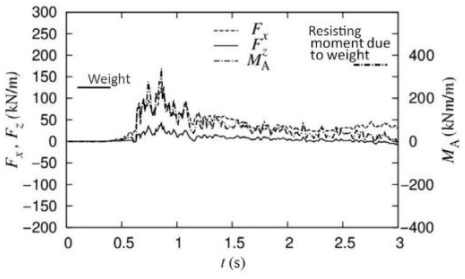

Figure 2.3. Tsunami force [Bricker et al., 2015].

Another scenario that was simulated is described as follows [Bricker et al., 2015]. The deck is initially fully submerged at a slow flow speed of 1m/s. This produces the full buoyancy force and a very small downward hydrodynamic force. The forces are relatively small and no motion occurs. Subsequently, a wave with a height of 1m and a flow speed of 5m/s approaches. The results of this simulation are shown in Figure 2.4. The pressure distribution around the bridge deck is initially close to a hydrostatic one. As the wave with the increased flow velocity approaches, the water surface rises due to blockage by the bridge deck and causes the pressure to increase at the seaward side of the deck. Due to this non-uniform increase of the pressure, see Figure 2.5, the overturning moment increases. At about t = 10.5s, the overturning moment exceeds the moment capacity and the deck starts to rotate. The uplift force increases due to this increased angle of attack. When t is 10.9s, the uplift exceeds the weight of the bridge deck. At This moment the whole deck is lifted off the abutments. The resisting horizontal friction force completely diminish and the deck starts to translate horizontally by the horizontal force despite the small value of the load, less than 1/5 of the weight. The forces (and the motion) after this fluctuate violently.

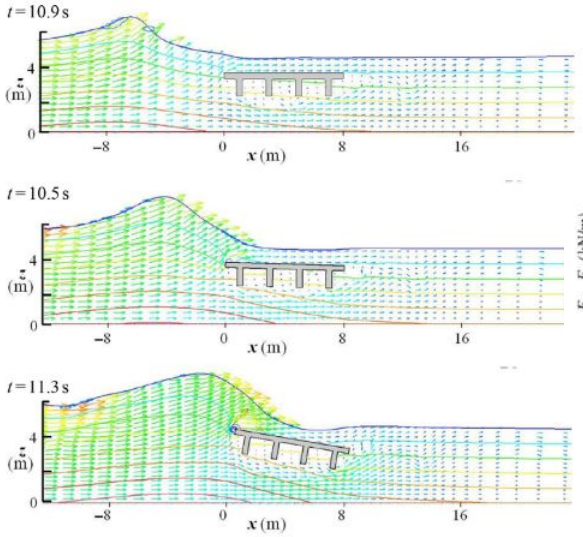

Figure 2.4. Tsunami impact on submerged bridge deck h= 1m v=5m/s [Bricker et al., 2015].

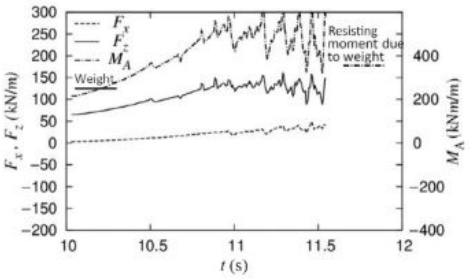

Figure 2.5. Tsunami force [Bricker et al., 2015].

2.2.3. Entrapped air pockets

The amount of trapped air between deck girders in the Utatsu Ohahshi bridge during the tsunami turned out to have a significant effect on the behavior of the bridge due to the buoyant force accompanied by the entrapped air [Maruyama et al., 2017].

Especially in case of an incoming wave or bore it is intriguing what the effect of the entrapped air underneath a bridge is on the vertical buoyancy forces on the deck. The total bouyancy of the bridge increases which lead to lower frictional forces. It is interesting to see what the differences are in the connections between the girders. This can be done by diaphragms as is done in the Utatsu bridge [Bricker and Nakayama, 2014; Kawashima and Matsuzaki, 2012]. Which can be observed in Figure 2.6. A different approach is the use of crosses so water can flow partially in and out of the hollow sections.

2.2.4. Inclination in bridges

Main roads with high-speed limits often have a minor inclination of the bridge deck in their alignment. Near the coast where the main roads are curvy, this is often the case. As is discussed in [Bricker and Nakayama, 2014] inclination of bridge decks has a significant effect on the failure modes of the bridge. The inclination of the bridge caused an increase in flow velocity over the top of the bridge and confined flow on the bottom, resulting in an upward force.

Regardless of the inundation ratio or Froude number, the negative inclination of the deck results in a smaller downward lift and a lower drag coefficient. Nevertheless, results of incipient failure analysis indicate that the overall stability of the deck is reduced when there is an inclination of the deck [Naderi, 2018].

Figure 2.6. Utatsu highway bridge with visible hollow compartments [Kawashima and Matsuzaki, 2012].

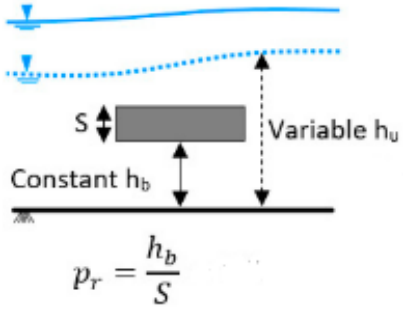

Figure 2.7. Proximity ratio definition [Naderi, 2018].

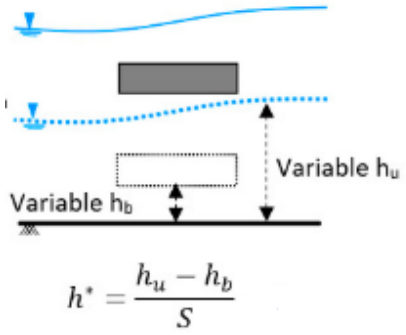

Figure 2.8. Inundation height definition [Naderi, 2018].

2.2.5. Effects of nearby structure on bridge failure

Another factor that potentially contributed to the failure of the Utatsu bridge was the presence of a seawall. As the distance of the seawall to the deck reduces, the flow forces on the bridge deck increases. This might explain the transverse variation of displaced deck locations of the Utatsu bridge [Bricker and Nakayama, 2014] in Figure 1.1.

Not much research has been done on the effects of seawalls on bridge failure, though studies have been done to the amount of overtopping over different coastal defense structures [Esteban et al., 2017]. When the seawall is on the land side of the bridge, the seawall can affect the upward forces of the superstructure of the bridge. If the seawall is located on the seaside of the bridge, supercritical flow can arise which have significant larger effects on the stability of the bridge deck than subcritical flow.

In practice, problems occur in the case of confined wave action to vertical walls. For instance, at the Afsluitdijk, a military beam which is located in front of the critical parts to protect it from bombing, gave unwanted confined impact forces underneath this beam [Hofste, 2012]. In the case of a seawall that is close to the bridge, an incoming tsunami could also start acting as a confined wave.

2.2.6. Submergence of the bridge deck

Figure 2.7 and 2.8 display how the proximity ratio and the inundation height are determined in the research of [Naderi, 2018] and [Oudenbroek, 2018].

The inundation factor plays an important role in the failure of the bridge deck [Naderi, 2018]. [Bricker and Nakayama, 2014] mentions that bridge failure could not have happened at all without being fully submerged and that the lift force increases when the submergence ratio increases, the drag force will grow initially when the submergence ratio increases but this reaches a constant value.

The combination of small flow velocity and inundation ratio higher than 2 results in the most critical situation for the vertical stability of the bridge deck [Naderi, 2018].

Figure 2.9. Osaka bridge failure due to collision with tanker [Mainichi, 2018].

[Naderi, 2018] states that regardless of the proximity ratio and the Froude number, the bridge deck collapsed when the inundation ratio ($h*$) was higher than 1.3. This indicates that the deck is more sensitive to high water levels than flood velocity or distance to the channel floor. Moreover, no failure of the bridge occurred for inundation ratios lower than 1.3, indicating that the deck has to be deeply submerged before failure occurs.

In cases of steady flow, vertical forces were found to be downward unless the deck is significantly submerged ($h* \geq .5$) and the upstream velocity is relatively small (Frd < 0.6). In fact, for $h* < 3.5$ the development of flow patterns on the upper side of the deck is constrained by the presence of the free surface which causes an asymmetric pressure distribution in the vertical direction and ultimately results in a downward force. An increase in velocity results in a more downward force and hence more stability of the bridge (given that the submergence of the bridge is not too high) which ultimately can exceed the upward buoyancy force when the Froude number is 0.97 or higher [Naderi, 2018].

As inundation ratio $h*$ increases, the overall magnitude of the drag forces and the negative lift forces increase. The net effect on the resistance against horizontal movement becomes negative when h* > 1.5 – 1.75. This indicates that the influence of the drag forces starts dominating over the influence of the negative vertical forces. Increasing h* (at constant Fr) only will cause the deck to fail at some point [Oudenbroek, 2018].

2.2.7. Distance between the deck and the channel floor

The contours representing the starting point of failure indicate that by increasing the proximity ratio, failure occurs at a lower h*. Proximity ratio is the ratio between the distance of the deck to the bottom and the thickness of the deck, see Figure 2.7. In fact, a lower level of water is enough to initiate the failure of the bridge when it is located further from the channel floor. This indicates that with a larger distance from the deck to the channel floor the stability of the bridge will decrease [Naderi, 2018].

2.2.8. Debris effects

The effect on bridge superstructures due to debris is in many cases the main failure mechanism in the case of floods, tsunami's or hurricanes. A good recent example for this is the failure of the highway bridge towards Osaka's airport, September 4, 2018 [Mainichi, 2018]. In Figure 2.9 the failure of this bridge is displayed.

The effect of debris and especially incoming debris like ships in Figure 2.9 on these structures is significant. This study will focus on other factors that play a role in the failure of bridge superstructures and not debris effects.

The accumulation of smaller debris around bridge piers or decks which increases the hydrodynamic loads on the complete system and has to be taken into account as an additional loading effect [Oudenbroek, 2018].

2.3. Bearing types between bridge deck and pier

The type of bearing is very important in determining the failure mechanism. When a bearing is applied with a low friction coefficient the bridge deck is likely to slide off the piers. On the contrary, when a high friction

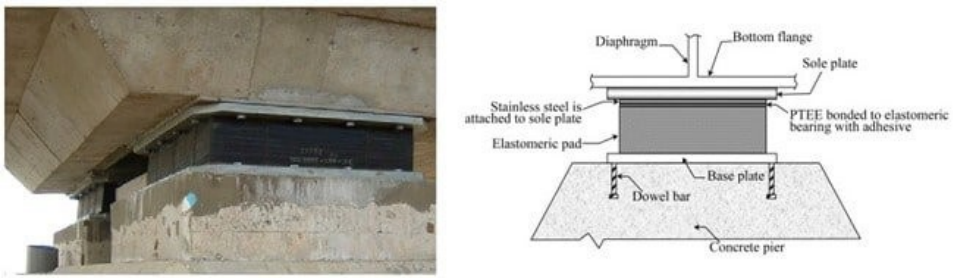

Figure 2.10. Elastomeric bearing for bridges [Hamakareem].

coefficient is used, the bridge deck has the potential risk to tip over. Shear keys or UPD's can be applied as counter measures. These are often used in earthquake sensitive areas to restrain the lateral movement of the bridge deck caused by earthquakes. With shear keys or UPD's it is impossible for bridge decks to slide off its piers without the shear keys or UPD's failing first.

The most common type of bearing which is used nowadays is the elastomeric bearing. It consists of elastomer manufactured from synthetic or natural rubber and can endure both translational and rotational movements through elastomer deformation. The ability of elastomer to carry large vertical loads is due to reinforcement provision that prevents lateral bulging of the elastomer. There are a number of elastomeric bearing pads classified based on types of reinforcements specifics. For example, steel reinforced, plain, fiberglass reinforced and cotton duck reinforced elastomeric bearing pads. Strength and response of each type are different, steel reinforced elastomeric bearing is the strongest one and the plain elastomeric pad is the weakest. Elastomeric bearing is neither expensive nor requires considerable maintenance, that is why it is the most desired bearing type. Figure 2.10 shows details of an elastomeric bearing and its application in bridge structure [Hamakareem].

Retrofitting existing bridges with bearings that can resist large horizontal forces, preventing the disconnection of the deck from the pier, will ensure that sufficient weight is mobilized to withstand the overturning moments by drag forces [Oudenbroek, 2018].

2.4. Force of an elastomeric bearing

Equation 2.1 shows the relation between horizontal force and displacement of an elastomeric bearing.

$$H_D = \frac{G * A_{bear} * \Delta x}{t_b} \tag{2.1}$$

H_D Horizontal force against the bearing [N]

G Shear modulus of the elastomeric material [N/m^2]

A_{bear} Plan area of the bearing [m^2]

Δx Shear deformation [m]

t_b Thickness of the bearing [m]

The maximum shear deformation of the bearing is defined by different design guidelines. Some define it as half of the bearing thickness which results in $\frac{\Delta x}{t} = 0.5$.

Movement of the bearing pad along its mating surface should be prevented. This is referred to as 'slippage' and will occur when the lateral forces are higher than the friction factor multiplied by the actual normal force [Oudenbroek, 2018].

$$H_{max,F} = \mu * (F_z - F_L - F_B) \tag{2.2}$$

$H_{max,F}$ Horizontal capacity of the bearing (friction failure mode) [N]

μ Friction factor between elastomeric material and mating surface [-]

F_z Plan area of the bearing [N]

F_L Shear deformation [N]

F_B Thickness of the bearing [N]

The friction coefficient of importance is the one between the elastomeric material and the steel sole plate. Different manufacturers of bearings refer to different friction coefficients, such as 0.20 [Cosmec]. [The Trelleborg Group, 2017] states a range of friction factors between 0.2 and 0.33.

Failure of the anchorage of the sole plates to the concrete bridge girders can induce failure. These anchors are steel headed studs which can easily be welded to a sole plate and cast into the concrete.

A governing failure mode in the total failure of a bridge deck is the frictional resistance of its bearings [Oudenbroek, 2018]. It needs to be stressed that this conclusion regarding the governing failure mechanism only applies for a bearing which is not fixed. Other types of bearings that are fixed (i.e. lateral movement in one or multiple directions is restricted) exist.

As is displayed in [Bricker and Nakayama, 2014] the unseating prevention devices in the Utatsu bridge were still intact after the failure of the bridge decks. From this can be concluded that the deck had to be lifted or rotated before undergoing the horizontal movement.

2.5. Shear keys

Exterior shear keys are designed to restrain the lateral displacements of bridge girders in the case of seismic events. The shear keys in bridge abutment structures are divided into two types, exterior or interior shear keys. An advantage of external shear keys is the ease of inspection and repair. The shear keys are designed as sacrificial elements and it is assumed that once their capacity has been exceeded, the shear keys would not provide further support [Bi and Hao, 2015]. As such, the bridge columns should be designed to provide lateral support once the shear keys have failed to function, or the deck will be allowed to move in a horizontal direction to prevent failure of the bridge pier or abutment.

Shear keys influence the seismic responses of bridge structures. Shear keys restrain lateral displacements of bridge decks and reduces its lateral-torsional responses, which result in smaller pounding forces and less severe pounding damages to bridge decks. Shear keys can significantly decrease the dislocation potential of bridge girders. Pounding between bridge girders and shear keys can increase the internal forces in the bridge piers in the transverse direction and therefore increase the damage potential of bridge piers.

Interior shear keys should be avoided in new construction projects as they are not as accessible as exterior keys [Megally et al., 2002].

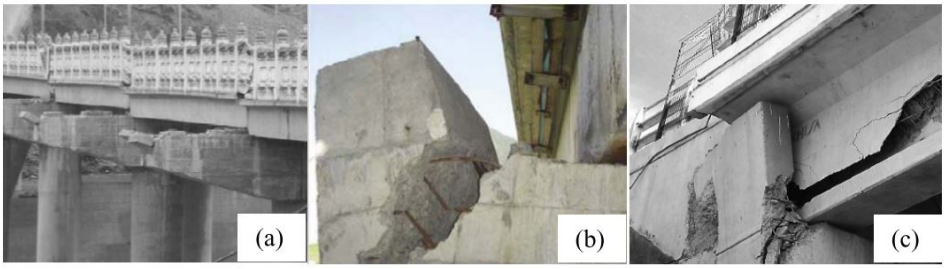

Figure 2.11. Typical shear key failure: (a) totally shear of; (b) diagonal shear failure; (c) flexural failure [Megally et al., 2002].

If concrete shear keys are applied, different failure modes of the shear keys can be observed [Bi and Hao, 2015]. In Figure 2.11 different types of shear key failure are displayed. UPD's (unseating prevention devices) can be placed in different locations underneath the bridge deck. These devices are often made of steel and are displayed in Figure 1.3.

2.5.1. Eurocode shear design resistance

Shear design value under which no shear reinforcement is necessary for elements unreinforced in shear can be calculated with Equation 2.3.

$$V_{Rk,c} = [C_{Rk,c} k (100 \rho_l f_{ck})^{1/3}] b_w d \tag{2.3}$$

$C_{Rk,c}$ Coefficient derived from test (0.12) [-]

k size factor = $1 + \sqrt{(\frac{200}{d}}$ [m]

ρ_l Longitudinal reinforcement ratio (=<0.02) [-]

f_{ck} characteristic concrete compressive strength [N]

b_w smallest web width [N]

d effective height of cross section [m]

2.6. Hydrodynamic flow forces of bridge decks

The Federal Highway Administration (FHWA) [Kerenyi et al., 2009] issued a report based on physical experiments and CFD Modelling. Three types of bridges were tested for their reaction to drag forces, lift forces, and moment-generating forces in relation to the degree of inundation. The inundation ratio is expressed as follows:

$$h^* = \frac{h_u - h_b}{s} \tag{2.4}$$

h^* Inundation ratio

h_u height of the free surface [m]

h_b distance from ground surface to bottom of the deck [m]

s height of the bridge deck [m]

The forces in horizontal (drag) and vertical (lift) direction are usually expressed in non-dimensional coefficient forms. In equation 2.5 the equation for a fully submerged bridge is shown.

$$C_D = \frac{F_D}{0.5 \rho v^2 (Ls)} \tag{2.5}$$

C_D Drag coefficient

F_D Drag force [N]

ρ Density [kg/m^3]

v Velocity [m/s]

L Length of the bridge [m]

In case of a partially inundated bridge $s = h_u - h_b$. The lift coefficient can be calculated as in equation 2.6.

$$C_L = \frac{F_L}{0.5 \rho v^2 (LW)} \tag{2.6}$$

C_L Lift coefficient

F_L Lift force [N]

W Width of the bridge [m]

The moment coefficient with respect to the center of gravity of the superstructure is defined in equation 2.7

$$C_M = \frac{M_{cg}}{0.5 \rho v^2 (LW^2)} \tag{2.7}$$

C_M Moment coefficient

M_{cg} Moment around centre of gravity $[Nm]$

Three different cross-sections of bridges were used in the research of [Kerenyi et al., 2009]; a six-girder bridge deck representing a typical U.S. highway bridge deck shape, a three-girder bridge deck with the same width but a larger frontal area and a streamlined bridge deck. The physical experiments were carried out at different values of the Froude number.

The physical experiments for the six-girder bridge deck showed a minimum of the drag coefficient C_D at values of h* ranging from 0.5 to 0.8, with a maximum of about 2.0 as $h* \geq 1.5$. As the Froude number increased, so did the drag coefficient. So the Froude number and the drag coeficient are positively correlated. Only one of the three numerical models used (the Fluent k-ϵ model), was able to reproduce these results fairly well.

The lift coefficient C_L remained negative for all inundation ratios, with a minimum between h* = 0.8 to 1.2, according to the experimental results. This indicates a net force pushing down on the structure at all times. None of the numerical models used corresponded well to the results of the physical experiments.

The moment coefficient C_M showed a peak around a value of h* equal to 0.8, indicating a tendency of the upstream part of the deck to move upwards and the downstream part downwards. As the values of h* increased, the value of C_M approached a constant value, which was smaller when the Froude number increased. This resulted in transitioning from positive to negative values of C_M around Fr = 0.3. The CFD results did not seem to be able to reproduce the peak value of C_M.

2.7. Hydrodynamic wave forces on bridge decks

A significant part of the research that has been done with regards to wave impact is done for offshore platforms. In most of these researches, forces on vertical piles and horizontal plates are studied. Horizontal plates represent a bridge deck to a certain extend. In the case of offshore platforms, the normative loading is often governed by dynamic loading on the structures whereas a tsunami is a one wave force on the structure.

Different wave characteristics resemble various force profiles. Firstly, in case of a surging wave, the water particles move in a circular path which results in horizontal and vertical forces. Secondly, a propagating bore has particles moving majorly in horizontal direction which results in horizontal forces and has a high peak force before a quasi-steady flow force. Thirdly, in the case of a breaking wave, the initial force has an even higher peak force also called a slamming force.

[Wang, 1970] studied the uplift pressure that waves cause on a horizontal plate that is suspended at distances of 0 to 0.04m above the mean water level. The experiments were conducted in a 27.5-meter by 27.5-meter square basin. Wave heights varied due to the method of wave generation. The waves were supposed to represent wave patterns from explosions, and typically had a height of 0.05m and a maximum height of 0.15m. Wang found that the uplift pressure has two components. The first is a large impact pressure from the initial impact of the wave on the bottom of the plate. The second is a slowly changing pressure component due to the specific wave height and time interval. The author found that the maximum magnitude of the slowly changing component was related to the hydrostatic pressure resulting from the difference between the elevation of the crest of the wave and the elevation of the bottom of the deck. The equation that has been found is:

$$p = C\rho(\eta - z) \tag{2.8}$$

p The maximum slowly changing pressure on the bottom of the plate

η The elevation of the crest of the wave

C A coefficient between 1 and 2

[Wang, 1970] also found that the impact pressure on the deck was caused by the change of momentum of the wave as it contacted the bottom of the plate. This uplift impact pressure can be expressed through the following equation:

$$P = \frac{\pi H \rho_w g}{2} \tanh\left(\frac{2\pi d}{L}\right)\sqrt{1 - \frac{4z^2}{H^2}} \tag{2.9}$$

P uplift pressure at impact

ρ_w density of water

H wave height

z deck height above the standing water line

d water depth

L wave length

[Wang, 1970] determined that only waves that had moderate steepness and were preceded by a trough caused these impact pressures. In cases where there was no impact pressure, there was only the slowly fluctuating pressure acting on the deck. Wang only considered the vertical forces acting on the plate. This was due to the flat plate lacking a substantial amount of vertical area for the water to contact. This made the horizontal forces on the plate very low and seemingly insignificant [Kallaka and Wang, 2011; Michael Henry; max Sheppard and Marin, 2009].

2.7.1. Solitary wave forcing

[McConnell et al., 2004] proposes a method to calculate the forces on a flat deck in coastal zones in an analytical manner. This method is only valid for solitary waves.

First, the pressures at the top and bottom of the deck are determined:

$$p_{top} = [\eta_{max} - (b_h + c_l)]\rho g \tag{2.10}$$

$$p_{bottom} = [\eta_{max} - c_l]\rho g \tag{2.11}$$

η_{max} maximum crest elevation

b_h element height

c_l clearance height between water level and deck

The vertical wave force can then be determined by:

$$F_v = \int_{b_w}\int_{b_l} p_{bottom}\,dA \cong b_w b_l p_{bottom} \tag{2.12}$$

$$F_h = \int_{b_w}\int_{b_l}^{\eta_{max}} p_{hyd}\,dA \cong b_w(\eta_{max} - c_l)\frac{p_{bottom}}{2}, \quad \text{if} \quad \eta_{max} \leqslant c_l + b_h \tag{2.13}$$

Or

$$F_h = \int_{b_w}\int_{b_l}^{c_l+b_h} p_{hyd}\,dA \cong b_w b_h \frac{(p_{top} + p_{bottom})}{2}, \quad \text{if} \quad \eta_{max} > c_l + b_h \tag{2.14}$$

b_l element length

b_w element width

p_{hyd} hydrostatic pressure

When applying this method to the bridge deck which is used in this thesis, the deck has to be schematized as a deck without the girders underneath. To simplify this deck, it is chosen that for the b_h the height of the bridge including girders is chosen when calculating horizontal forces. The value of b_h is chosen without girders in case of calculating vertical forces. This method results in the hydrostatic forces on the deck. No slamming forces are included which makes this method not suited to use as a tool in this research.

2.7.2. Bores

The wave forces from bores on horizontal decks is a research area where little knowledge is gained yet. Bores on vertical walls have been examined. Although, this is not comparable with forces on a flat deck.

[Bea et al., 1999] concentrated their research on offshore platform decks. An analytical model was presented as the sum of five forcing components: buoyancy, slamming, drag, lift and inertia. As the wave crest encounters the platform deck, there is a transfer of momentum from the water towards the structure that is reflected as the initial slamming force [Kjeldsen and Myrhaug, 1979]. As the wave continues to inundate the deck, buoyancy, drag and inertia forces are developed, see Figure 2.12. The magnitude of the slamming force relative to the peak wave inundation force is dependent on the characteristics of the deck.

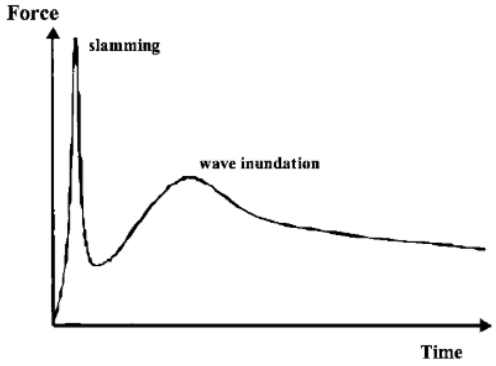

Figure 2.12. Idealized force development on platform deck. [Bea et al., 1999].

The main objective of the work of [Bea et al., 1999] was finding the horizontal component of the force.

$$F_{Drag} = 0.5\rho C_D A u^2 \tag{2.15}$$

$$F_{Inertia} = 0.5\rho C_M V \dot{u} \tag{2.16}$$

$$F_{Lift} = 0.5\rho C_L A u^2 \tag{2.17}$$

$$F_{Slamming} = 0.5\rho C_s A u^2 \tag{2.18}$$

C_D drag coefficient

C_M inertia coefficient

C_L lift coefficient

C_s slamming coefficient

u horizontal fluid velocity in wave crest

A frontal area of the structure

V volume of the structure

While the equations itself are quite simple, the importance of the dynamic characteristics of the structure and the wave were also included by using a multiplication coefficient to give an 'effective' slamming force. This requires knowledge of the structure's primary modes of vibration as well as the frequency of the slamming force among other variables.

In the case of tsunami impact, there is no repeated wave loading on the structure. Failure mechanisms of bridge decks due to tsunami are formed by the force of a single wave.

2.7.3. Initial slamming force

A tsunami wavelength is usually much larger than the width of a bridge. Therefore, it is reasonable to assume that, the entire bridge is inundated when the tsunami free surface elevation reaches a certain level. Nonetheless, when a bore has been formed in a more inland location, this slamming force will still exist.

An estimation for the slamming force is proposed by [Bea et al., 1999].

$$F_s = 0.5 * C_s * \rho * A * u^2 \tag{2.19}$$

C_s Slamming coefficient between π and 2π

A Vertical deck area

F_s $F_e * F_s$

F_e Dynamic loading which reflects the loading characteristics and the deck response

$$F_e = 2 * \pi * \alpha \frac{t_d}{T_n} \tag{2.20}$$

T_n Natural period of the deck

t_d Duration of the impact loading

This means the impact force is dependent on the dynamic behavior of the bridge deck. In this research, a model bridge is used which has a very small natural frequency.

[Cuomo et al., 2007] focused their research on the quasi-static pressure that occurs after the slamming force and introduced a factor that represents the slamming force and can be calculated for different cases. The '*' entails a dimensionless force and it is calculated for a 1 in 250 exceedance level.

$$F^*_{qs1/250} = a * \frac{\eta_{max} - c_l}{d} + b \tag{2.21}$$

In this equation, a and b are dimensionless factors that are deterministically determined values for different deck configurations. In the case of a beam, the horizontal pressures are calculated with the factors: a is 1.19, b is 0.43 and for the vertical forces on an exterior vertical deck: a is 1.23 and b = 0.51.

$$F^*_{max1/250} = a * F^*_{qs1/250} \tag{2.22}$$

For which the multiplication factor 'a' is 2.45 for horizontal force and 1.99 for vertical force.

$$F = F^* * (\rho_w g H_s A) \tag{2.23}$$

[Azadbakht and Yim, 2014] also developed a method to determine the wave forces of a tsunami on a bridge superstructure. In this method the wave is split into different stages, the first is the initial stage in which a slamming force hits the bridge deck. The second stage has a more gradual force and is dependent on the inundation height of the superstructure.

$$F_{Hmax} = F_{h\_hs} + F_d = 0.5\rho g(2h_0 - L_h)L_h + 0.5C_d\rho v^2 L_h \tag{2.24}$$

$$F_{DVmax} = C_{DV}(F_{v\_hs} + F_{v\_s}) = C_{DV}[(\rho g(h_0 - L_g - T_d)L_v + 0.5C_{v_s}\rho v^2 L_{sb}] \tag{2.25}$$

$$F_{UPmax} = C_{UP}(F_b + F_l) = C_{UP}(\rho g V + 0.5C_l\rho v^2 L_v) \tag{2.26}$$

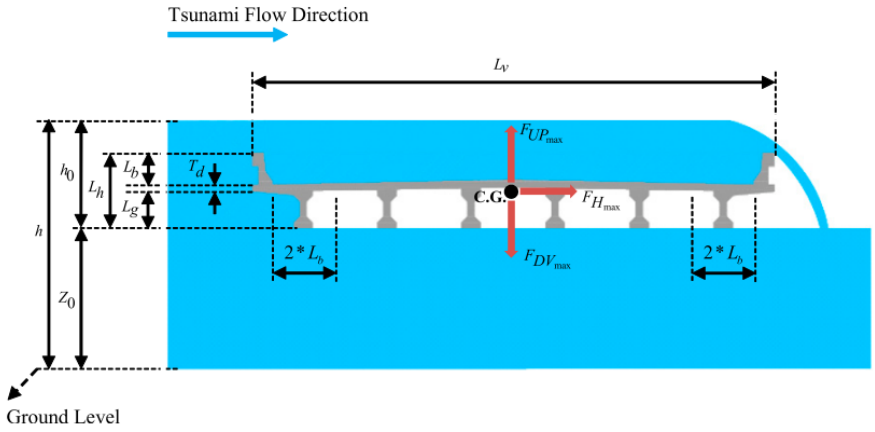

Figure 2.13. Sketch explaining parameters in equations 2.24, 2.25 and 2.26, [Azadbakht and Yim, 2014].

$FHmax$ maximum horizontal force

$FDVmax$ maximum downward vertical force

$FUPmax$ maximum uplift force

CDV empirical downward vertical force coefficient; 0.53

CUP empirical uplift force coefficient; 0.77

Fh_hs hydrostatic horizontal force

Fv_hs hydrostatic downward vertical force

Fd drag force

Fv_s slamming vertical force

Fb buoyancy force

FL lift force

Cd drag coefficient; 2.0

Cl lift coefficient; 1.0

Cvs slamming coefficient in the vertical direction; 2.0

g acceleration of gravity

V volume of the bridge per unit length

Lh height of the bridge superstructure

Lv width of the bridge superstructure

Lb height of the bridge barrier

Lsb effective length of the bridge deck for a vertical slamming force; 4 × Lb

Lg height of the bridge girder

Td thickness of the bridge deck

$Z0$ low chord elevation of the bridge superstructure

h tsunami water free-surface elevation resulting in maximum horizontal and downward vertical hydrostatic forces

v tsunami flow velocity

$h0$ difference between the tsunami water free-surface elevation and low chord of the bridge

Note that for box-section bridges, the height of the girder (Lg) is zero and the low chord elevation (Z_0) is calculated from the bottom of the bridge deck.

2.7.4. Dynamic wave force

Also, [Kaplan, 1979] and [Kaplan, 1992] did research on wave forcing on suspended cylindrical elements and suspended horizontal flat platform decks. [Kaplan 1995] expanded these methods for predicting the wave forcing. The total vertical forcing was described as follows:

$$F_v = \rho \frac{\pi}{8} \frac{LW^2}{\sqrt{1+\left(\frac{W}{L}\right)^2}} \frac{\delta v}{\delta t} + \rho \frac{\pi}{4} WLC \frac{1+\frac{1}{2}\left(\frac{W}{L}\right)^2}{[1+\left(\frac{W}{L}\right)^2]^{\frac{3}{2}}} v + \frac{1}{2} C_D \rho A v^2 \tag{2.27}$$

F_v Total vertical force

L Length of the structure

W Wetted width of the structure

v Vertical water particle velocity

$\frac{\delta v}{\delta t}$ Vertical water particle acceleration

C Wave celerity

A Projected area in the vertical direction

2.7.5. Conclusion relating to the forces on the bridge superstructure

With respect to the horizontal force it can be stated that there are three types of hydrodynamic forces present. One is a hydrostatic wave force caused by the difference in water level between the sea and the land side of the bridge. The second is the hydrodynamic drag force which is caused by the speed of the wave flow over and under the bridge. The third and most critical force on the bridge superstructure is the initial slamming force. This force is more difficult to determine and depends on the state of the wave when it is approaching.

2.8. Tsunami modelling

2.8.1. Different coasts, different tsunamis.

There are several types of patterns of tsunami effects on the land, depending on the local bathymetry and topography characteristics. Figure 2.14 shows a classification of tsunami inundation based on bottom topography. The type of tsunami mainly depends on the steepness of the sea bottom slope. If a sea bottom slope is gentle, a tsunami peak disintegrates into several waves due to wave dispersion effects (soliton fission) and the waves propagate to the shore, then the breaking waves run up on land. When a sea bottom slope is steep, the sea level changes generated by tsunami move only vertically. However, when the sea level exceeds the freeboard of coastal defense structures, overflowing sea water inundates onto land as a propagating bore [Mase et al., 2013]. The latter case in which there is a steep sea slope is the case in the Otsuchi area.

2.9. Wave forms

In the lifetime of a wave, one has multiple phases. In this research, the waves are categorized into five types of waves discussed below. The type of wave at the location of the bridge depends upon the relation between the depth and the wavelength. Various types of waves are displayed in Figure 2.15.

In which D = Depth of water, L = Length of wave and H = Height of wave.

Deep-water waves are waves traveling across a body of water where the depth is greater than half the wavelength (D > 1/2 L) displayed on the right in Figure 2.15. These waves are not treated in this research since the bridge is located on a shallow bottom.

Transitional waves are waves traveling in the water where the depth is less than half the wavelength but greater than one-twentieth the wavelength (1/20 L < D < 1/2 L). Transitional waves are often wind-generated waves that have moved into shallower water.

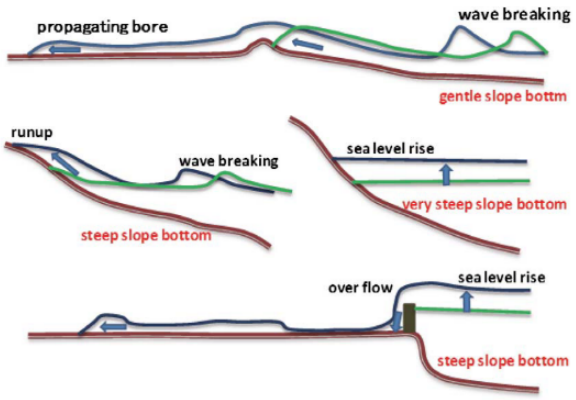

Figure 2.14. Types of tsunami effects for a gentle and a steep slope bottom [Mase et al., 2013].

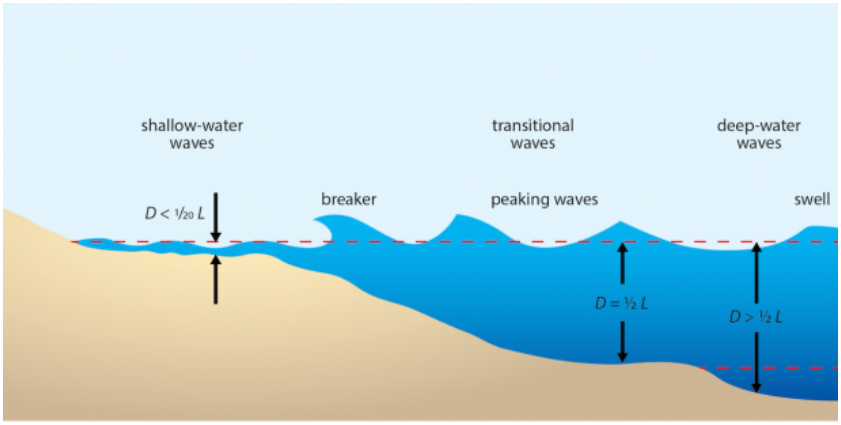

Figure 2.15. Wave phases along shore [Byron, 2019].

Shallow-water (quasi breaking waves/ peaking waves) waves are waves traveling in the water where depth is less than one-twentieth the wavelength (D < 1/20 L). Shallow-water waves include wind-generated waves that have moved into shallow, nearshore areas, tsunamis (seismic waves) generated by disturbances in the ocean floor and tidal waves generated by the gravitational attraction of the sun and moon.

Breaking shallow-water waves are unstable shallow-water waves. Usually, shallow-water waves begin to break when the ratio of wave height to wavelength is 1 to 7 (H/L = 1/7), when the wave's crest peak is steep (less than 120°), or when the wave height is three-fourths of the water depth (H = > 3/4 D). A breaking wave occurs when one of three things happen: The crest of the waveforms an angle less than 120°, the wave height is greater than one-seventh of the wavelength (H > 1/7 L) or the wave height is greater than three-fourths of the water depth (H > 3/4 D).

Breaking unstable deep-water waves are waves that begin to break when the seas are confused (waves from mixed directions) or when the wind blows the crests of waves, forming whitecaps. These types of waves do not occur in this research since the waves are generated in a controlled manner without wind or other limiting factors for the propagation of waves.

Once the wave is broken near the shore a wavefront will occur. Normally a fully developed bore will only exist when there is a constant flow from both sides and the bore height will be constant. In a coastal area, there will not be a backflow. So, the propagating bore will always lose its energy and thus its height because of the bottom roughness.

From these six types of waves, three are recognized in this research namely the shallow water waves, breaking shallow water waves and the propagating wavefront.

2.10. Scaling factors

Ideally, a physical model would have the same dimensions as the real-life case. And all the scaling factors would be met. Though scale factors are dependent on different values. Here, the most important scaling factors are given for hydraulic physical tests.

2.10.1. Geometrical similarity

The model and the full-scale structures must have the same shape.

$$\lambda = \frac{L_F}{L_M} \tag{2.28}$$

L_F length of full scale model

L_M length in the model

2.10.2. Kinematic similarity

The flow velocity and models will have geometrically similar motions in the model and full scale. For example, flow speeds in x and y-direction must have the same ratio so that circular motion does not become an elliptical motion.

2.10.3. Froude number

The ratio between inertia and gravity.

$$\frac{Inertiaforce}{Gravityforce} = \frac{F_i}{F_g} = \frac{\rho U^2 L^2}{\rho g L^3} = \frac{U^2}{gL} \tag{2.29}$$

$$\frac{U_M}{\sqrt{gL_M}} = \frac{U_F}{\sqrt{gL_F}} = Fr \tag{2.30}$$

F_i inertia force

F_g gravity force

Fr Froude number

Equality in the Froude number in the model and full scale will ensure that gravity forces are correctly scaled. Surface waves are gravity driven, equality in Fr will ensure that wave resistance and other wave forces are correctly scaled.

2.10.4. Reynolds number

The ratio between inertia and viscous forces.

$$\frac{Inertiaforce}{Viscousforce} = \frac{F_i}{F_v} = \frac{\rho U^2 L^2}{\mu UL} = \frac{UL}{\nu} = Re \tag{2.31}$$

With:

$$\nu = \frac{\mu}{\rho} \tag{2.32}$$

In which:

U velocity of the fluid with respect to the object

L Length of the structure

μ Dynamic viscosity of the fluid 0.001 $[N * s/m^2]$

ν Kinematic viscosity of the fluid $1 * 10^{-6}$ $[m^2/s]$

Equality in the Reynolds number will ensure that viscous forces are correctly scaled. The Reynolds number will determine when a laminar flow will translate into a turbulent flow.

2.10.5. Weber number

The ratio between inertia and surface tension forces.

$$\frac{Inertiaforce}{Surfacetensionforce} = \frac{F_i}{F_s} = \frac{\rho U^2 L^2}{\sigma L} = \frac{\rho U^2 L}{\sigma} \tag{2.33}$$

$$\frac{U_M}{\sqrt{\frac{\sigma_M}{(\rho L)_M}}} = \frac{U_F}{\sqrt{\frac{\sigma_F}{(\rho L)_F}}} = Wn \tag{2.34}$$

Wn Weber number

σ surface tension

Equality in the Weber number will ensure that surface tension forces are correctly scaled [NTNU, 2014].

Unfortunately, not all these similarities can be met when conducting less than full-scale experiments. This is due to the fact that in the expressions of some forces, geometric quantities and kinematic quantities are raised to different powers.

In hydraulic flow experimental tests, gravity is the most important influence factor. Therefore, the scaling of these tests will be done with the help of the Froude number.

2.11. Numerical models.

Numeral computational models can be used to model a tsunami wave against a bridge. A couple of these models will be treated in this section.

CFD (computational fluid dynamics) is a branch of fluid dynamics in which numerical analysis and data structures are used to solve and analyze problems that involve fluid flows to perform calculations. This is a cell-based model. The primary research of [Naderi, 2018] about the failure of the bridge deck due to steady flows is done with a CFD model.

ICFD (incompressible computational fluid dynamics) focuses on the solution of CFD problems, where the incompressibility constraint may be applied.

DEM (discrete element method) is a particle-based Lagrangian solution and is used to simulate a wide variety of granular flow and rock mechanics. By direct contact between two particles in the model, the particles interact with each other. These interactions are modeled as a spring-dashpot system [Wu et al., 2016]. The discrete element method is majorly used in the simulation of granular flows and not as much in fluid flows. In DualSPHysics the DEM method is used to model the rigid bodies.

SPH (smoothed particle method) is a Lagrangian way of modeling. Though, in comparison with the DEM, the effect of the particles on each other is smoothed. Particles have a domain around them in which they have an influence on each other, the closer these particles are, the higher the influence will be. This is a proper method to apply in the case of modeling moving structures.

ALE (Arbitrary Lagrangian-Eulerian methods) is a finite element formulation in which the computational system is not a prior fixed in space (Eulerian based) or attached to the material (Lagrangian based). In the ALE technique, the computational mesh inside the domains can move arbitrarily to optimize the shapes of elements while the mesh on the boundaries and interfaces of the domains can move along with materials to precisely track the boundaries and interfaces of a multi-material system.

2.12. SPH modelling

SPH (smoothed particle Hydrodynamics) is a computational method used for simulating the mechanics of continuum media, such fluid flows. It was developed by Gingold and Monaghan [Gingold and Monaghan, 1977] and Lucy [Lucy, 1977], initially for astrophysical problems. SPH is a meshfree Lagrangian method (where the coordinates move with the fluid particles).

Advantages
SPH guarantees the conservation of mass without extra computation since the particles themselves represent mass. SPH computes pressure from weighted contributions of neighboring particles rather than by solving linear systems of equations. Unlike grid-based techniques, which must track fluid boundaries, SPH creates a free surface for two-phase interacting fluids directly since the particles represent the denser fluid (usually water) and empty space represents the lighter fluid (usually air). For these reasons, it is possible to simulate fluid motion using SPH in real time. However, both grid-based and SPH techniques still require the generation of renderable free surface geometry using a polygonization technique such as metaballs and marching cubes, point splatting, or 'carpet' visualization.

Disadvantages
One drawback over grid-based techniques is the need for large numbers of particles to produce simulations of equivalent resolution. In the typical implementation of both uniform grids and SPH particle techniques, many particles will be used to fill water volumes that are never rendered. Accuracy can be significantly higher with sophisticated grid-based techniques, especially those coupled with particle methods (such as particle level sets) since it is easier to enforce the incompressibility condition in these systems.

2.12.1. Kernel approximation [Liu and Liu, 2003]

The formulation of SPH is made up of two important steps, kernel approximation and particle approximation. First, the Kernel approximation will be discussed.
The concept of integral representation of a function $f(x)$ used in the SPH method starts from the following identity.

$$f(x) = \int_{\Omega} f(x')\delta(x - x')dx' \tag{2.35}$$

Where f is a function of the three-dimensional position vector x, and $\delta(x - x')$ is the dirac delta function [Liu and Liu, 2003]. When x = x', $\delta(x - x') = 1$ and otherwise $\delta(x - x') = 0$.

If the Delta function kernel $\delta(x - x')$ is replaced by a smoothing function $\Omega(x - x', h)$, the integral representation of f(x) is given by

$$< f(x) >= \int_{\Omega} f(x')W(x-x',h)dx' \tag{2.36}$$

The smoothing function W is usually chosen to be an even function for reasons given later. It should also satisfy a number of conditions. The first one is the normalization or unity condition that states:

$$\int_{\Omega} W(x-x',h)dx' = 1 \tag{2.37}$$

The second condition is the Delta function property that is observed when the smoothing length approaches zero.

$$\lim_{h\to 0} W(x-x',h) = \delta(x-x') \tag{2.38}$$

And the third condition is the compact condition:

$$W(x-x',h) = 0 \ \ when \ |x-x'| > \kappa h \tag{2.39}$$

Where κ is the constant related to the smoothing function for a point at x and defines the effective (non-zero) area of the smoothing function. This area is called the support domain. See Figure 2.18.

Note from equation 2.36 that the support domain of the smoothing function is $|x'-x| < kh$, the errors in the SPH integral representation can be roughly estimated using the Taylor series expansion of $f(x')$ around x, where f(x) is differentiable. Using equation 2.36 leads to:

$$\begin{aligned} < f(x) > &= \int_{\Omega} [f(x') + f'(x)(x'-x) + r(((x'-x)^2)]W(x-x',h)dx' \\ &= \int_{\Omega} W(x-x',h)dx' + f'(x)\int_{\Omega}(x'-x)W(x-x',h)dx' + r(h^2) \end{aligned} \tag{2.40}$$

In which r is the residual. W is an even function with respect to x, hence $(x'-x)W(x-x',h)$ should be an odd function, hence we should have

$$\int_{\Omega}(x'-x)W(x-x',h)dx' = 0 \tag{2.41}$$

from equations 2.35 and 2.41 follows:

$$< f(x) >= f(x) + r(h^2) \tag{2.42}$$

From the above equation, it can be seen that, in the SPH method, the integral representation or kernel approximation of a function is of second-order accuracy. However, this kernel approximation is not necessarily of second-order accuracy if the smoothing function is not an even function, or if the normalization condition is not satisfied.

Integral representation
The approximate for the spatial derivative $\nabla f(x)$ is obtained by substituting $f(x)$ with $\nabla f(x)$ in equation 2.36.

$$< \nabla f(x) >= \int_{\Omega} [\nabla f(x)]W(x-x',h)dx' \tag{2.43}$$

The divergence on the integral is operated with respect to the primed coordinate.

$$[\nabla f(x')W(x-x'h)] = \nabla[f(x')W(x-x',h)] - f(x')\nabla W(x-x',h) \tag{2.44}$$

From equation 2.43 the following is obtained:

$$< \nabla f(x) >= \int_\Omega \nabla[f(x')W(x-x',h)dx' - \int_\Omega f(x')\nabla W(x-x',h)dx' \tag{2.45}$$

the first integral on the right side of Equation 2.45 can be converted using the divergence theorem into an integral over the surface S of the domain of the integration.

$$< \nabla f(x) >= \int_S f(x')W(x-x',h)\vec{n}\,dS - \int_\Omega f(x')\nabla W(x-x',h)dx' \tag{2.46}$$

Where $\vec{n}$ is the unit vector normal to the surface S.

Since the smoothing function W is defined to have compact support, when the support domain is located within the problem domain Figure 2.16, the surface integral on the right-hand side of Equation 2.46 is zero. If the support domain overlaps with the problem domain Figure 2.17, the smoothing function W is truncated by the boundary and the surface integral is no longer zero. Under such circumstances, modifications should be made to remedy the boundary effects if the surface integration is treated as zero in equation 2.46. Therefore, for those points whose support domain is inside the problem domain, 2.46 is simplified as follows.

$$< \nabla f(x) >= -\int_\Omega f(x')\nabla W(x-x',h)dx' \tag{2.47}$$

From the above equation, it can be seen that the differential operation on a function is transmitted to a differential operation on the smoothing function. In other words, the SPH integral representation of the derivative of a field function allows the spatial gradient to be determined from the values of the function and the derivatives of the smoothing function W, rather than from the derivatives of the function itself.

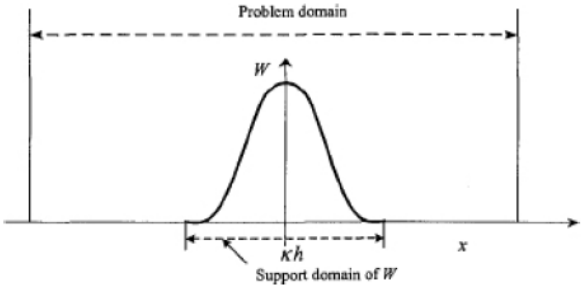

Figure 2.16. The support domain of the smoothing function W and problem domain. The support domain is located within the problem domain. Therefore, the surface integral on the right-hand side of equation 2.46 is zero. [Hobbs]

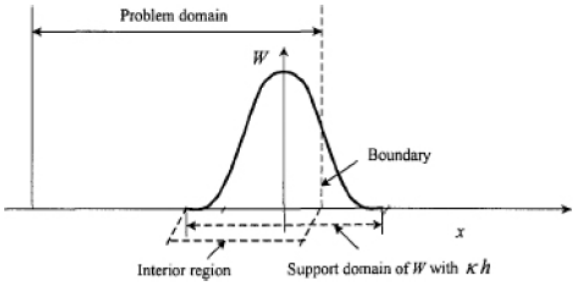

Figure 2.17. The support domain of the smoothing function W and problem domain. The support domain intersects with the problem domain. Therefore, the smoothing function W is truncated by the boundary and the surface integral on the right-hand side of equation 2.46 is no longer zero. [Hobbs]

2.12.2. Particle approximation [Liu and Liu, 2003]

In the SPH method, the entire system is represented by a finite number of particles that carry an individual mass and occupy an individual space. This is achieved by the following particle approximation, which is a key operation in the SPH methods.

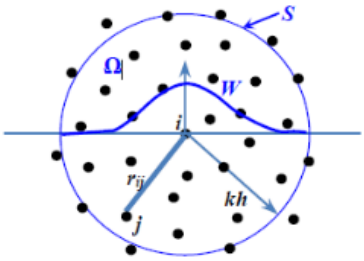

Figure 2.18. Particle approximation for a particle i within the support domain kh of the kernel function W. r_{ij} is the distance between particle i and j, S is the surface of the integration domain, Ω is the circular integration domain, j is the constant related to the kernel function and h is the smooth length of kernel function. [Hobbs]

The continuous integral representations concerning the SPH kernel approximation, expressed in equations 2.36 and 2.47 can be converted to discretized forms of summation over all the particles in the support domain shown in Figure 2.18. The corresponding discretized process of summation over the particles is commonly known as particle approximation in the SPH literature [Liu and Liu, 2003; Gingold and Monaghan, 1977; Monaghan, 1992]. This process is carried out as follows:

If the infinitesimal volume dx in the above integrations at the location of particle j is replaced by the finite volume of the particle V_j that is related to the mass of the particles m_j by

$$m_j = \Delta V_j \rho_j \tag{2.48}$$

Where j is the density of particle j (=1, 2, ..., n) in which n is the number of particles within the support domain of particle j. The continuous SPH integral representation for f(x) can be written in the following form of discretized particle approximation.

$$\begin{aligned} f(x) &= \int_\Omega f(x')W(x-x',h)dx' \\ &= \sum_{j=1}^{N} f(x_j)W(x-x_j,h)\Delta V_j \\ &= \sum_{j=1}^{N} f(x_j)W(x-x_j,h)\frac{1}{\rho_j}(\rho_j V_j) \\ &= \sum_{j=1}^{N} f(x_j)W(x-x_j,h)\frac{1}{\rho_j}(m_j) \\ &= \sum_{j=1}^{N} \frac{m_j}{\rho_j} f(x_j)W(x-x_j,h) \end{aligned} \tag{2.49}$$

The particle approximation for a function at particle i can ultimately be written as:

$$< f(x_i) >= \sum_{j=1}^{N} \frac{m_j}{\rho_j} f(x_j) W_{ij} \tag{2.50}$$

In which $W_{ij} = W(x-x_j,h)$.
Equation 2.50 states that the value of a function at particle i is approximated using the average of those values

of the function at all the particles in the support domain of particle i weighted by the smoothing function. Following the same argument, the particle approximation for the spatial derivative of the function is

$$< \nabla f(x) >= -\sum_{j=1}^{N} \frac{m_j}{\rho_j} f(x_j) \nabla W(x - x_j, h) \tag{2.51}$$

Where the gradient ∇W in the above equation is taken with respect to the particle j. The particle approximation for a function at particle i can finally be written as

$$< \nabla f(x_i) >= -\sum_{j=1}^{N} \frac{m_j}{\rho_j} f(x_j) \nabla W_{ij} \tag{2.52}$$

In which

$$\nabla W_{ij} = \frac{x_i - x_j}{r_{ij}} \frac{\delta W_{ij}}{\delta r_{ij}} = \frac{x_{ij}}{r_{ij}} \frac{\delta W_{ij}}{\delta r_{ij}} \tag{2.53}$$

Equation 2.52 states that the value of the gradient of a function at particle i is approximated using the average of those values of the function at all the particles in the support domain of particle i weighted by the gradient of the smoothing function W.
It can be seen that the particle approximation in equation 2.50 and 2.51 actually converts the continuous integral representations of a function and its derivatives to the discretized summations based on an arbitrary set of particles. This use of particle summations to approximate the integral is, in fact, a key approximation that makes the SPH method simple without using a background mesh for numerical integration.
Note that the particle approximation introduces the mass and the density of the particle into the equations. Which can be conveniently applied to hydrodynamic problems in which the density is a key parameter. This is probably one of the major reasons for the SPH method being particularly popular for dynamic fluid flow problems.
The particle approximation is, however, related to some numerical problems inherent in the SPH method, such as the particle inconsistency and the tensile instability. It may be mentioned here that the number of sampling points for integration should be more than the field nodes (particles). This is at least true for mesh free methods based on weak forms for solid mechanics problems. Otherwise, it may (not always) lead to some kind of instability problems. In summary, for a given particle i, according to the particle approximation, the value of a function and its derivative for particle i are approximated as

$$< f(x_i) >= \sum_{j=1}^{N} \frac{m_j}{\rho_j} f(x_j) W_{ij} \tag{2.54}$$

$$< \nabla f(x_i) >= \sum_{j=1}^{N} \frac{m_j}{\rho_j} f(x_j) \nabla W_{ij} \tag{2.55}$$

$$W_{ij} = W(x_i - x_j, h) = W(|x_i - x_j|, h) \tag{2.56}$$

$$\nabla W_{ij} = \frac{x_i - x_j}{r_{ij}} \frac{\delta W_{ij}}{\delta r_{ij}} = \frac{x_{ij}}{r_{ij}} \frac{\delta W_{ij}}{\delta r_{ij}} \tag{2.57}$$

In which r_{ij} is the distance between particle i and j. It should be noted that $\nabla_i W_{ij}$ is taken with respect to particle i, so the negative sign in equation 2.51 and 2.52 is removed in equation 2.55. It should be noted that if replacing the function f(x) with the density function in equation 2.54, the SPH approximation for the density is obtained as

$$\rho_i = \sum_{j=1}^{N} m_j W_{ij} \tag{2.58}$$

Equation 2.58) is one of the most popular forms of obtaining density in SPH and is generally referred to as a summation density approach. Note that W_{ij} has a unit of the inverse of volume. Equation 2.58 states that the density of a particle is a weighted average of those of all the particles in its support domain.

2.12.3. Support domain and influence domain

The support domain is where all particles inside this domain are used to determine the information at point x and the influence domain is defined as the domain where a particle exerts its influence.

The influence domain is associated with a node in meshfree methods and the support domain with any field point x. As SPH is a particle method that approximates field variables only on particles (or nodes) the support and influence domains are the same. For SPH the smoothing length h multiplied by the factor κ determines the support domain. As can be partially seen from the figure the smoothing length can vary both spatially and temporally.

2.12.4. Equation of state

The fluid in the SPH formalism defined in DualSPHysics is treated as weakly compressible and an equation of state is used to determine fluid pressure based on particle density. The compressibility is adjusted so that the speed of sound can be artificially lowered. This means that the size of the time step taken at any one moment (which is determined according to a Courant condition, based on the currently calculated speed of sound for all particles) can be maintained at a reasonable value. Such adjustment, however, restricts the sound speed to be at least ten times faster than the maximum fluid velocity, keeping density variations to within less than 1% and therefore not introducing major deviations from an incompressible approach.

The equation of state is defined as follows:

$$P = k_0 \left(\left(\frac{\rho}{\rho_0} \right)^{\gamma} - 1 \right) \tag{2.59}$$

With P = pressure, $\gamma = 7$ and $\rho 0$ is the reference density. To determine the pressure constant k_0 equation 2.60 is used.

$$c_0 = \sqrt{\frac{\gamma k_0}{\rho_0}} \geq 10 v_{max} \tag{2.60}$$

Where c_0 is the speed of sounds at the reference density and γ is 7. The pressure constant k_0 governs the relative density fluctuation. To determine values for k_0 we use the maximum flow velocity v_{max} [Yreux, 2018].

3

Physical model

The physical tests which were executed in the laboratory of Waseda University in Tokyo were carried out with the goal of the validation of the numerical SPH model. Results from the lab tests are discussed here and are compared to the results of the SPH model in Chapter 5.

The hydrodynamic data is extracted from several points in the flume. The movement of the failing deck which is filmed with high definition and high-speed cameras. With a tracker software, the movement of the deck is determined in a later stage.

In Table 3.1 it is displayed what kind of tests have been done in the limited time that was available. In Appendix A a table can be found with the main observations with regards to the failure modes from these physical laboratory tests.

Table 3.1. Overview of performed lab tests.

clean	shear key back	shear key middle	negative inclination	positive inclination
d50h20	d50h20	d50h20	d50h20	d50h20
d50h25	d50h25	d50h25	d50h25	d50h25
d50h30	d50h30	d50h30	d50h30	d50h30
d50h35	d50h35	d50h35	d50h35	d50h35
5x d60h20	d60h20	d60h20	d60h20	d60h20
5x d60h25	d60h25	d60h25	5x d60h25	d60h25
d60h30	d60h30	5x d60h30	d60h30	5x d60h30
d60h35	d60h35	d60h35	d60h35	5x d60h35
d70h20	d70h20	d70h20	d70h20	d70h20
d70h25	d70h25	d70h25	d70h25	d70h25
d70h30	d70h30	5x d70h30	d70h30	d70h30
d70h35	d70h35	d70h35	d70h35	d70h35

3.1. Description of the experiment

These experiments were executed in the water lab at the Waseda University in Tokyo, Japan. With the help of an underflow, a tsunami was created and propagated towards the bridge structure. The bridge structure is based on the 30 m long Yabitsu river Bridge in Iwate, Japan. This bridge collapsed following a flood after torrential rainfall on the 9th and 10th of August 2013. Remains of the mostly intact bridge deck segments were discovered approximately 50m downstream.

The physical tests are performed in an 11m long flume with a width of 40cm. A sketch with dimensions is given in Figure 3.1. On the left of the figure a 4.5m long water tank with a variable water height (d). The water is kept in the basin by a gate with a 15cm opening. The underflow is released by quickly opening the

gate. This is done by releasing a large mass M that pulls the gate open. The water flows out of the gate with significant velocity. A 1:10 slope is used to slow the water down and to represent a sloping beach. This slope starts directly at the gate. At a height of 20cm, the false bottom becomes flat again. The water level (h) on the false bed is measured from the bed level near the gate. In this research, the different cases are indicated as for instance d70h30. In this case, the water level in the tank is 70cm and the water level in the basin is 30cm. The slope and the false bed have a roughness by having stones on it with a diameter between 2 and 5mm. The bridge structure is placed at 4.45 m from the gate. This location gives the possibility to do water level measurements in front of the structure on the flat bed.

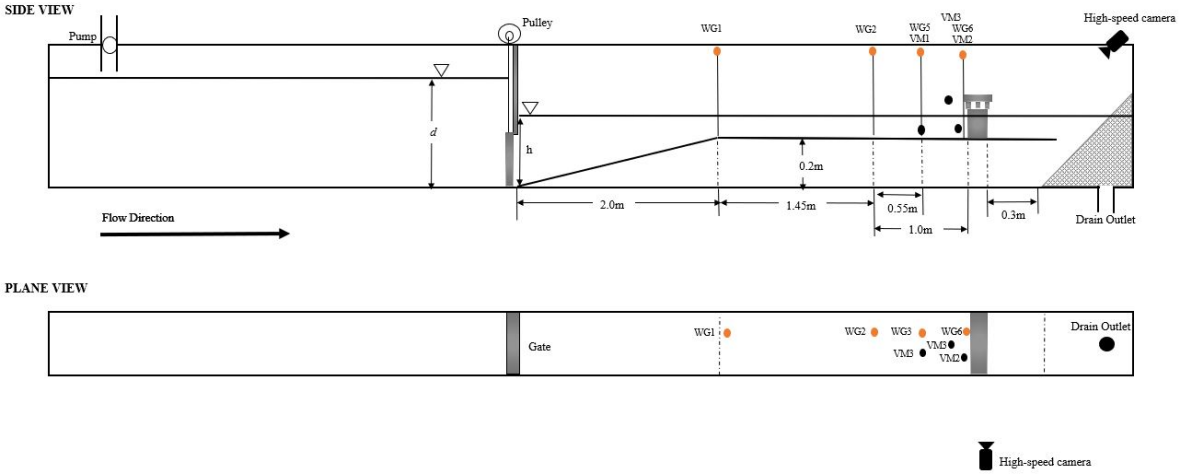

Figure 3.1. layout of the physical test setup.

Wave gauges and velocity meters are used to measure the water height and the velocity at several locations along the flume. The wave gauges are placed before the structure. No measurements could be done behind the bridge since the deck will be moving in that direction. The velocity meters in front of the bridge are placed as follows: one on 20mm from the floor with a horizontal distance to the front of the bridge deck of 48mm and one velocity meter on the same level as the bridge deck 170mm from the ground and 79mm from the bridge deck.

The wave gauges are placed in the following manner: WG1 is placed directly at the top of the slope, the second (WG2) is placed 1.45m behind WG1, WG5 is placed 2.00m from WG1 and the last wave gauge is placed directly before the bridge structure so 2.45m from WG1. The wave gauges were calibrated before every test so the water level that is displayed in the output data has 0 as start value which corresponds to the initial water level.

The bore can be changed by using different heights in the water basin or by using a layer of water in front of the gate. For this test, the water height in the basin is varied between 50, 60 and 70 cm. The height of the water layer in front of the gate is varied between 20, 25, 30 and 35 cm, the height of the basin has a large influence on the velocity and height of the bore, because the water flows with a bigger pressure through the gate and this results in higher velocities and discharge. The water layer behind the gate is used to have different wave speeds of the incoming tsunami wave $\sqrt{gh}$. These wave conditions are tested in five different situations. These situations are displayed in the following Figure 3.2.

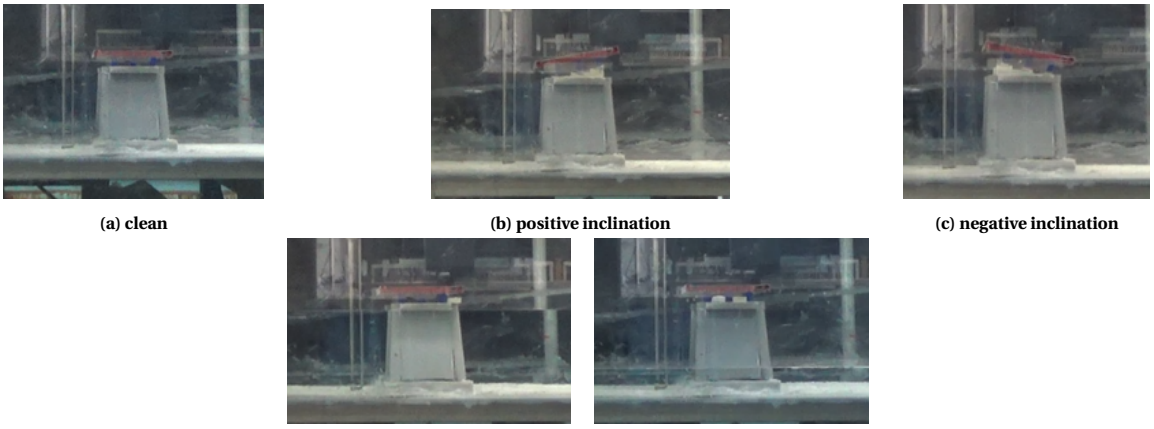

(a) clean (b) positive inclination (c) negative inclination

(d) shear key back (e) shear key middle

Figure 3.2. Physical test bridge layouts.

In Figure 3.3 different snapshots are shown of the wave propagation and the bridge movement of the physical test with case d70h30. In Figure 3.3a it can be observed that the wave is breaking when it approaches the bridge deck.

The shear keys are constructed from ABS plastic and are mounted on the bridge pier with a rigid connection. So, no failure of these shear keys can occur. In Figure 3.3 is displayed how a bridge deck in the case of d70h30 is moved off its piers and in Figure 3.4 the wave height in the four different wave gauges are shown.

In Figure 3.3 the step by step failure of the bridge is displayed. At t = 0.00s the wave just broke and some splashing up from the wave can be seen. At t = 0.56s the roughly disturbed wavefront is arriving at the bridge. Directly after impact, the bridge deck starts its movement and slides of its pier. At t = 1.11s the deck slide of its pier and moves to the bottom by its gravity and has a horizontal movement in the flow. At t = 1.66s one corner has hit the bottom and therefore a rotating moment occurs which makes the deck rotate. In the last timestep of t = 2.22s the deck lays on its back and a clear disruption of the water level can be seen which is created by the narrowing of the flow by the bridge piers.

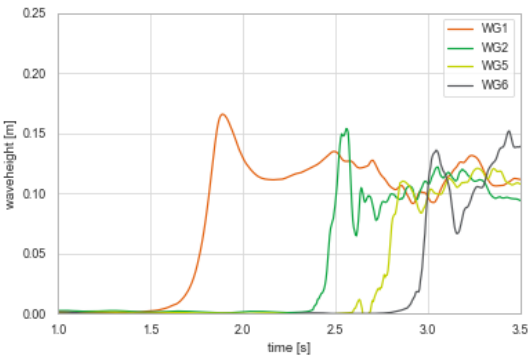

Figure 3.4. Outcomes wavegauges physical tests d70h30.

Wave breaking takes place between WG1 and WG2 which explains the noise in the data for WG2, WG5 and WG6. With these data, the wavefront velocities can be determined by dividing the distance between wave gauges over the time between the wave peaks. This results in a wave speed of 2.15 m/s between WG1 and WG2 and a wave velocity of 1.83 m/s between WG2 and WG5. It is logical that a wave with less height has less speed, though while the wave is breaking in between the wave gauges the exact wavefront speed is not accurate.

(a) t = 0.00

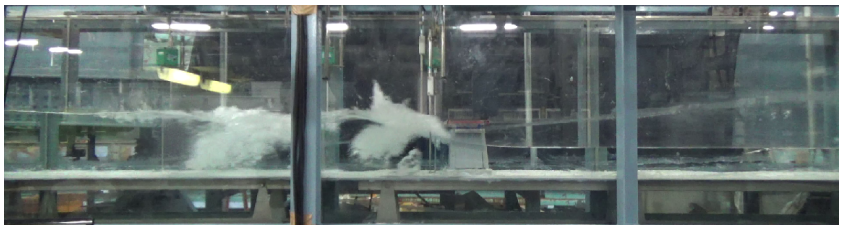

(b) t = 0.56

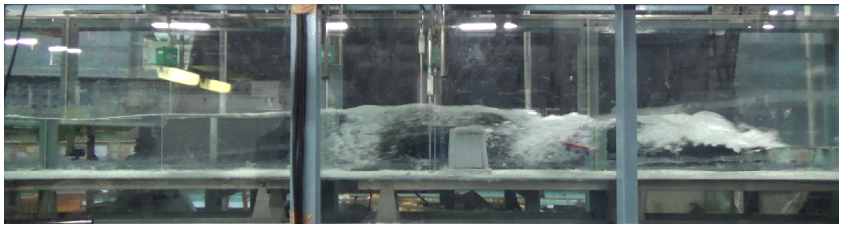

(c) t = 1.11

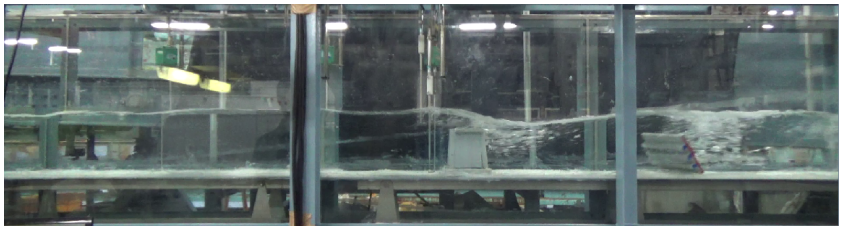

(d) t = 1.66

(e) t = 2.22

Figure 3.3. d70h30 dambreak test

The output of the velocity measure instruments was not correct due to air entrainment within the turbulent bore. Instead, the bore front velocity [vfront] is used calculated from the wave gauges. The wave is breaking between wave gauge 1 and 2 which makes these calculations of the wave speed inaccurate. Apart from this, the wave speed of a bore is different from the wave speed of a propagating wave [Okamoto et al., 2008].

3.1.1. Friction factor of the deck/pier connection

The friction factor is determined by tilting the whole construction until it starts to slide off. This procedure is executed six times. To determine the final value for this friction force, the highest and the lowest value of the tests were not included and the average of the middle 4 values is taken. This results in an angle of 16.91°.

Table 3.2. Threshold of motion angles.

test number	angle of sliding
1	16.60°
2	16.50°
3	19.10°
4	17.45°
5	16.20°
6	17.10°

The mass of the bridge deck is 1180 grams. When the angle of sliding and the weight of the deck are known the friction force can be calculated.

$$F_{friction} = sin(\alpha) * m * g \tag{3.1}$$

With known m is 1.180kg is $9.81 m^3/kg/s^2$ and the angle is 16.91° the friction force is determined on 3.37 N. Then the maximum friction force and the normal force are known, so the friction factor can be determined.

$$F_{friction} = F_{normal} * \mu \tag{3.2}$$

This results in a friction factor of 0.29. The weight of the bridge deck used in the tests is 1180 grams and the bridge has a width of 254 mm. Per meter width, the gravitational force will be 45.57 N. The connection between the deck and the pier has a friction factor of 0.29. When the wave does not result in any vertical forces a horizontal force of 13.2N per meter width is needed to move the bridge deck.

3.1.2. Scale model

The scale model of the bridge which is used in the physical tests is the same bridge that is used in the research to bridge stability in steady flow [Oudenbroek, 2018]. The bridge is based on the 28-meter-long Yabitsu Bridge displayed in Appendix D.1 which was part of prefectural road 162 in the Iwate Prefecture in Japan, crossing the Yabechi River. The bridge collapsed during the floods that occurred as a result of torrential rainfall on the 9th and 10th of August 2013. This bridge consists of three segments modeled at a 1:37 scale. One model bridge deck segment is 254mm wide and the flume which is used is 400mm wide. Which limited the lab tests to use only one bridge segment, including one bridge deck and two bridge piers (see Figure D.2). The foundation, which was embedded in the false bottom during the steady flow tests was glued on the false bottom during the wave tests in Waseda. This makes the distance between the deck and the false bottom larger.

3.1.3. Technical specifications of the bridge model

The main material for the scale model is ABS (Acrylonitrile butadiene styrene). Next to this, a small amount of hardwood is used for the model. The model is made up of different components namely the base of the pier, the pier foundation and the deck segments. Since plastic has a lower density than concrete, the material used for the bridge in reality, each component has a hollow cavity that can be filled with a material having a higher density than concrete to achieve the correct weight. A shortcoming of the scale model is that the railings that were on the sides of the bridge are not modeled. These railings would be too weak and fragile during the experiments if scaled down to the correct dimension. Nevertheless, it can be assumed that the

influence of the railings on the hydraulic forces on the deck as a whole is small, given that the effective area that is blocked by the railings is small. Thus, the omission of the railings in the scale model is justifiable. Only when the accumulation of debris is studied, the railings can have a significant contribution. Skin friction is not accurately modeled by these scale models since the surface roughness of the plastic model is much less than the surface roughness of the concrete bridge in the field. However, it is assumed that most of the horizontal forces on the bridge decks and piers are caused by form drag instead of skin friction, so this is justifiable.

3.2. Analysis of the water level in the tank

In this analysis, the water height in the tank before the gate will vary. This results in a different initial head difference at the location of the gate, which results in different wave characteristics.

3.2.1. Hydrodynamics

In Figure 3.5 and 3.6 the hydrodynamic conditions are displayed for the locations of WG1 and WG6. The time is adjusted such that the wave peak at WG1 is at the same moment for all the cases. It is visible that the wave height and wave speed increases as the water level in the tank rises.

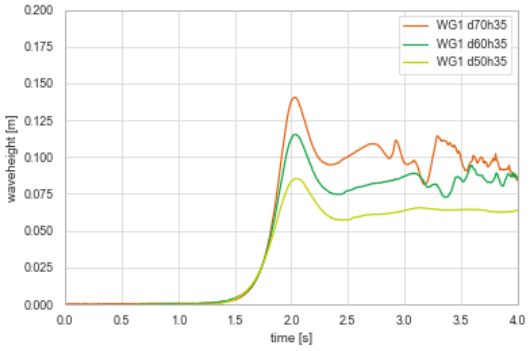

Figure 3.5. Wave heights at WG1 for different water levels in the tank.

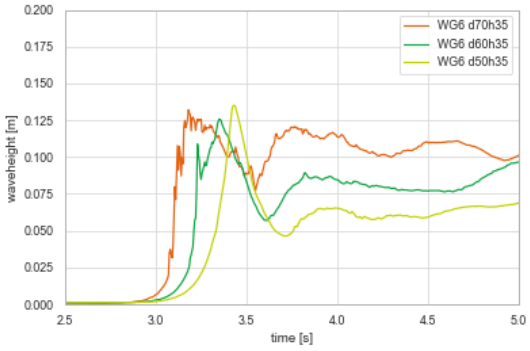

Figure 3.6. Wave heights at WG6 for different water levels in the tank.

3.2.2. Analytical estimated force on bridge deck

The wavefront speed is determined by dividing the distance over the time difference between the wave peaks at WG1 and WG6. The bore front velocity of the d70h35, d60h35 and d50h35 cases are respectively 2.14m/s, 1.86m/s and 1.76m/s.

Velocity meters were placed in the flume as well, the maximum wave velocities read by these devices were in the order of 0.40 m/s This is measured at a location 5mm from the bed. The velocity meter that was placed at the height of the deck, unfortunately, didn't give any useful results since this device is exposed to air in turbulent regions of the wave.

In section 2.7 different ways for calculating the forces on the bridge deck are mentioned with different assumptions. The outcomes of these calculations are displayed in Table 3.3. The scatter between these outcomes is very large.

Table 3.3. Force calculation from literature review, d70h30 case.

	McConnel et al., 2004	Azadbakht and Yim, 2014	Cuomo et all 2007	SPH LS-Dyna
Fv [N]	100.1	201.85	96.99	59.54
Fh [N]	15.6	91.78	109.9	77.35

When using the method of [Cuomo et al., 2007] explained in section 2.7 for the determination of the wave forcing. The outcomes for $F^*_{qs1/250}$ are given in Table 3.4. For the calculation of the forces on the bridge deck,

the velocity of the bore front is used, even when the flow velocity is actually meant. The maximum wave height of the wave at the location of WG6 is used. Forces calculated in Table 3.4 are calculated per meter width of the bridge deck.

Table 3.4. Analytical calculation of forces on bridge deck in [N].

				Horizontal			Vertical		
	η	d	cl	$F^*_{qs1/250}$	$F_{qs1/250}$	$F_{qs1/250max}$	$F^*_{qs1/250}$	$F_{qs1/250}$	$F_{qs1/250max}$
d70h35	0.132	0.15	0.005	1.44	55.84	136.82	1.55	60.27	119.93
d60h35	0.126	0.15	0.005	1.39	51.54	126.28	1.50	55.70	110.85
d50h35	0.135	0.15	0.005	1.46	58.06	142.25	1.58	62.62	124.60

For the horizontal force calculations, a =1.19, b = 0.43 and a_{max} is 2.45 since it is taken as an external beam element. And for the vertical calculation: a = 1.23, b = 0.51 and a_{max} = 1.99 since it is taken as an external deck element, these values are deterministically determined by [Cuomo et al., 2007] for his specific physical experiments, A is also 30mm since this is the distance between the edge of the slab and the first girder. In both cases from the dimensionless to the real force A = $0.03m^2$ and $H_s = \eta$. In Table 3.4 the other variables are displayed together with the resulting forces. In this particular comparison, the only variable that is changing is the wave height. It is important to notice the different phases of the waves since in the d50h35 case the wave is still surging and in the other two cases it is already a propagating bore, the analytical calculation does not make any distinction in this difference. The threshold of failure based on the friction coefficient will arise when a horizontal force of 13.2N is applied and no vertical forces are generated by the hydrodynamics of the wave.

3.2.3. Movement of bridge deck

The movement of the bridge deck with a varying water level in the tank is shown in Figure 3.7, the time series of the x and z coordinates can be found in the appendix in Figures D.3 and D.4.

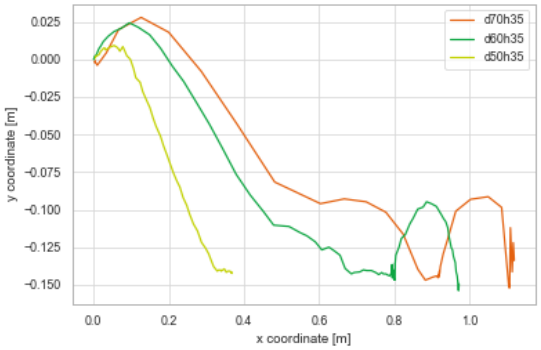

Figure 3.7. Physical tests varying d, h35 bridge movement path.

Concluded from Figure 3.7 can be that the traveled distance of the bridge superstructure is dependent on the water height in the basin. Larger water height in the basin results in a larger water mass which transports the bridge superstructure over a larger distance. Another interesting remark can be made about the vertical uplift of the bridge. The higher the water level in the basin the higher the upward movement is on the bridge deck.

3.3. Analysis of the water level in the basin

Another parameter that is varied in the tests is the water level on the false bottom. The hydrodynamic results of these tests are visualized in Figures 3.8 and 3.9. The movement of the superstructure is displayed in Figure 3.10.

3.3.1. Hydrodynamics

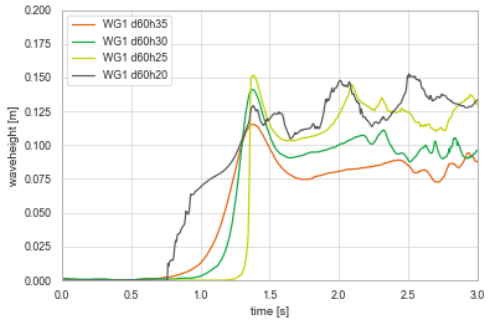

Figure 3.8. Wave heights at WG1 for different initial water levels in the tank.

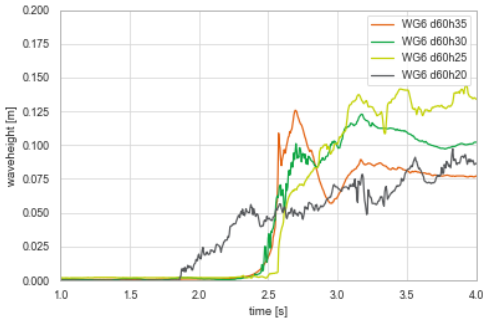

Figure 3.9. Wave heights at WG6 for different initial water levels in the tank.

In the d60h20 case, the wave is a propagating bore, no water is present at the bed level. Therefore, it is shown in Figure 3.8 that the wave has a different incoming pattern than the other waves. Since the wave height of this wave is so low that it does not reach the bridge deck, the movements of the deck are not displayed in Figure 3.10.

3.3.2. Analytical estimated force on bridge deck

In Table 3.5 the analytically calculated forces are displayed. These forces are determined in the same way as the last section.

Table 3.5. Analytical calculation of forces on bridge deck in [N].

				Horizontal			Vertical		
	η	d	cl	$F^*_{qs1/250}$	$F_{qs1/250}$	$F_{qs1/250max}$	$F^*_{qs1/250}$	$F_{qs1/250}$	$F_{qs1/250max}$
d60h35	0.126	0.15	0.005	1.39	51.54	126.28	1.50	55.70	110.85
d60h30	0.101	0.1	0.055	0.98	29.05	71.18	1.08	31.98	63.64
d60h25	0.137	0.05	0.105	1.19	48.04	117.71	1.30	52.30	104.08

The wave force of the d60h25 case is relatively big in comparison with the other cases. While this has a lower water depth at the location of the bridge. Though the head difference near the gate is the biggest so the initial flow out of the basin will be the highest of the cases compared in this analysis. it is also shown in Figure 3.8 and 3.9 that the crest height of this wave is the highest.

3.3.3. Movement of bridge deck

In Figure 3.10 the movement path of the different water levels in the basin can be observed.

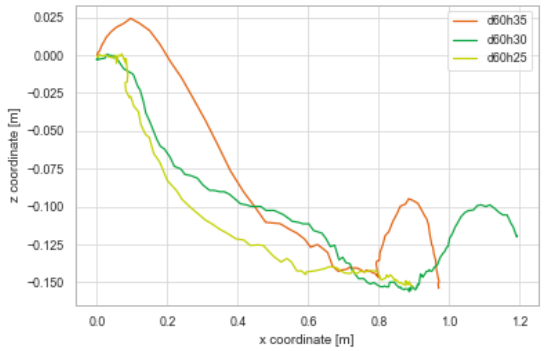

Figure 3.10. Physical tests bridge movement, constant d varying h.

A d60h20 test is performed as well. The wave which was formed in this test did not affect the bridge to make it move. From this analysis, it is clear that only in the case of a water level in the basin of 35cm, the wave height is strong enough to result in a vertical upward movement of the deck. In other cases, the hydrodynamic conditions only result in sliding of the bridge deck.

3.4. Analysis shear keys

In Figure 3.10 it is visible that the bridge deck in cases d60h25 and d60h30 only has horizontal movement and barely vertical uplift. Expected would be that in these cases the shear key would work pretty well since this measure would withstand the horizontal movements of the bridge decks. Expected could be that the bridge deck would still fail in the d60h35 case since a significant uplift movement is observed. As displayed in Figure 3.11 the vertical uplift in case of the shear key at the back side is minor in the d60h30 case. In the d6025 case, no movement is observed of the bridge deck.

3.4.1. Movement of bridge deck

When the middle shear keys are applied to the piers there is no movement observed from the deck at all in the d6025 and d60h30 cases. The movements of the deck in the d60h35 case with different layouts of the shear keys are displayed in Figure 3.12.

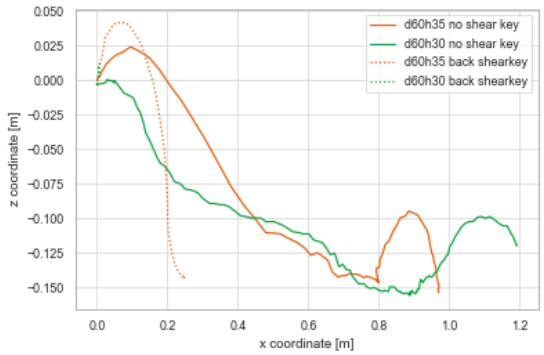

Figure 3.11. Movement of the deck with and without shear key on the shore side.

In this analysis, it is chosen to compare the results of two tests, d60h35 and d50h35. The magnitude of the forces should be in the same order as the computed forces in section 3.2. Apart from the lab test execution insecurities. It is chosen to analyze these specific cases since here it is visible what the effects of the shear keys are with different types of waves.

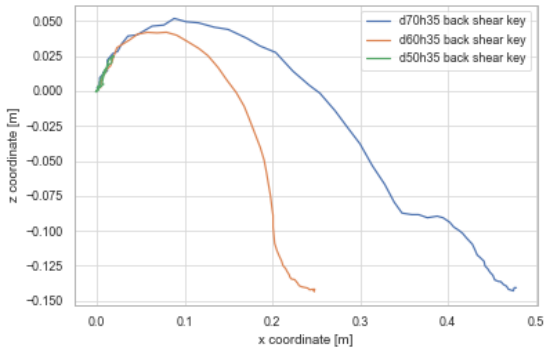

Figure 3.14. Movement of bridge deck d varying h35 for shearkeys backside.

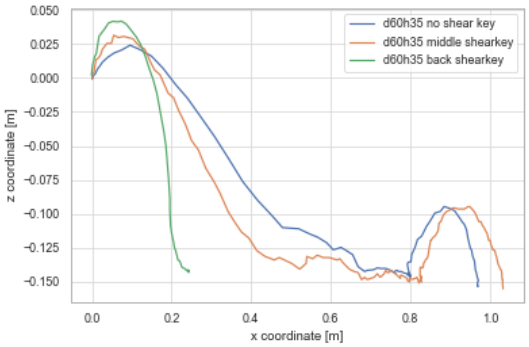

Figure 3.12. Movement of bridge deck including shear keys in d60h35 case.

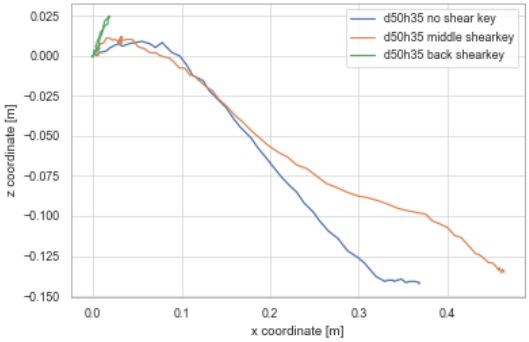

Figure 3.13. Movement of bridge deck including shear keys in d50h35 case.

In Figure 3.13 it is shown that the back shear key prevents the bridge from complete failure. The bridge makes a rotation around the point where it connects the shear key, but it does not rotate around it completely. The middle shear key prevents the bridge from failing by the initial wave, but a less large rotation is needed to lift the deck over the shear keys, which does happen in the initial wave. The secondary wave then slides the deck completely of the pier.

When analyzing both Figures 3.12 and 3.13 it can be concluded that the middle shear key does not affect the path of the bridge significantly. In cases with shear keys, it is clear that the vertical force is the dominant failure mechanism.
In appendix A it is shown that even if the main failure mode of a bridge without a shear key is sliding, still some rotational movement can be observed in case shear keys are applied.

In Figure 3.14 the movement of the deck is shown in case of different water levels in the tank. It follows that a significant movement of the deck occurs in the d50h35 case. A d40h35 case has also been executed, though no movement of the deck is observed in that case. The threshold of failure is with a basin height between 50cm and 60cm. The wave heights in front of the deck do not differ much from each other, see Figure 3.6. Though the bore front velocities are different.

3.5. Analysis inclination

The inclination that is used in this research is 10 degrees. in both positive and negative directions. To realize the inclination of the decks some help-pieces have been constructed so the bridge was inclined. The disadvantage of this help pieces are that the center of mass of the bridge deck was lifted. In addition to this the case of positive inclination, the help pieces functioned as shear keys which made sliding of the piers impossible. On the bridge girders is also a small piece of abs attached to realize a flat surface to the pier to make sure the

friction factor would be the same in case of inclination and no inclination.

3.6. Bridge behind a seawall

Several tests on the effect of a seawall on the bridge deck have been done. Behind the seawall a supercritical flow emerged which did not interact with the bridge deck causing it not to fail, in Figure 3.15 the d60h30 case is displayed of this test. Concluded from these tests can be that a seawall in front of the dike has a positive effect on bridge safety. During these tests, no wave properties could be reached so that the supercritical flow could hit the bridge deck. When this supercritical flow will hit the deck, the force will be significantly larger than when a subcritical flow hits the deck. Bridges with low height can be affected by this.

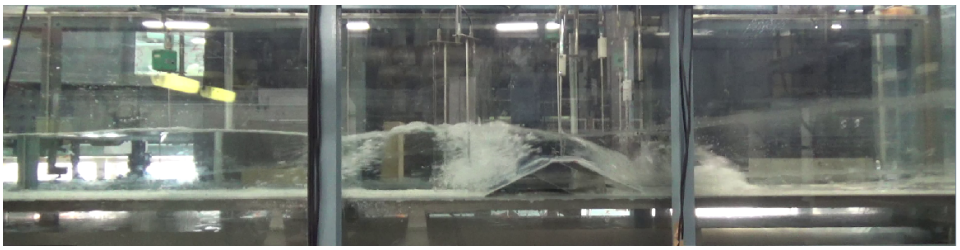

Figure 3.15. Snapshot of supercritical flow underneath bridge caused by seadike.

3.7. Discussion of the lab test

A dam break underflow test is used in this research to find tsunami-induced failure mechanisms of bridge superstructures. It can be questioned in what way a dam break underflow method simulates a tsunami in a correct manner. The waves created by this dam break underflow are not long enough to be compared to a tsunami in a steep slope ria coast area like the coast near Otsuchi.

Some factors in the execution of the lab tests are inaccurate. The gate opened with the use of a concrete block attached to the gate. Though, when analyzing the movies of the tests in a later stage of the research it was unclear if the gate opened consequently with the same opening size. Some inaccuracies were present at the water level. Since some water was always leaking from the tank, the water level in the tank was never 100% constant. This leakage made it hard to keep the water level on the right level and execute the tests exactly in the moments that the water levels were what they should be. The accuracy of the wave gauges can be questioned. The wave height is determined by electric conductivity. So, if any air bubbles were present the outcomes are not 100% accurate. The total amount of water in the column is displayed as the water height.

Another factor of insecurity is the bridge itself. Some scenarios were performed five times to see if the movement of the deck was constant. The bridge movement is never completely the same since this is also dependent on the exact position of the bridge on the pier, so the friction force is exactly the same. The way a bore propagates is never exactly the same so if the bridge is hit from the bottom or the front is of great importance when analyzing these bridge forces and movements. Also the forming of the wave at the opening of the gate is dependent on a great amount of factors. The effect of small deviations in this location will magnify and can have significant differences in the movement of the deck.

4

Numerical SPH Model setup and validation

The main research question of this research is to find out the failure methods of bridges with the help of an SPH model, multiple SPH models exist and are developed by different parties. At the beginning of this research, two different models have been set up with different software's. The first SPH model is called DualSPHysics and is a free to use open-source software developed by a collaboration between Universidade de Vigo, The University of Manchester, Instituto Superior Tecnico, Università degli studi di Parma, Universitat Politecnica de Catalunya and New Jersey Institute of Technology. The second SPH model is a commercial model, developed by LSTC (Livermore software technology company, called LS-Dyna.

4.1. Setup

In this section, the most important aspects of the SPH models are explained and some differences between LS-Dyna and DualSPHysics are highlighted. For more in depth theoretical background of the models [Domingues et al., 2018](dualsphysics), [Hallquist, 2006] (LS-Dyna) and [LSTC, 2019b] (LS-Dyna) could be consulted.

4.1.1. Dualsphysics

SPH simulations can be split into three main steps: 1) generation of the neighbor list, 2) computation of the forces between particles (solving momentum and continuity equations) and 3) update of the physical quantities at the next time step. As can be seen in Figure 4.1 these three steps will be performed iteratively until the total runtime is fulfilled.

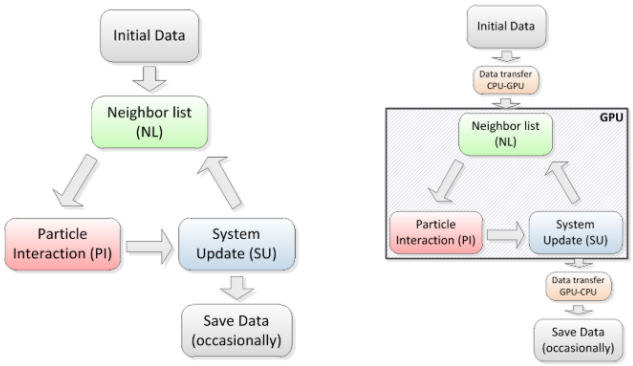

Figure 4.1. Flow diagram of the CPU (left) and total GPU implementation (right) [Domingues et al., 2018]

Dualsphysics is a WCSPH based model, this means it is quasi compressible. In the equation of state which is explained in section 2.12.4, this means that the density fluctuation is dependent on the pressure constant k_0 which in its turn is dependent on the speed of sound.

In DualSPHysics the boundary is described by a set of particles that are considered as a separate set to the

fluid particles [Domingues et al., 2018]. The Dynamic Boundary Condition (DBC) is the default boundary method provided by dualsphysics. This method treats boundary particles in such a way that they have the same equations as fluid particles. However, they do not move according to the forces exerted on them. Instead, they remain fixed in position. When a fluid particle approaches a boundary and the distance between its particles and the fluid particle becomes smaller than twice the smoothing length (h), the density of the affected boundary particles increases, resulting in a pressure increase. This results in a repulsive force being exerted on the fluid particle due to the pressure term in the momentum equation.

To reduce density fluctuations in Dualsphysics a delta-SPH formulation is applied. This introduces a diffusive term (of 0.1) in the equation for mass conservation to reduce density fluctuations in a very stiff density field.

For time stepping in DualSPHysics, a Verlet scheme is used, the common Verlet method is split into two parts and benefits from a low computational overhead compared to some other integration techniques. The predictor step calculates the variables according to:

$$\frac{dr_a}{dt} = v_a \tag{4.1}$$

$$v_a^{n+1} = v_a^{n-1} + 2\Delta t F_a^n \tag{4.2}$$

$$r_a^n = r_a^n + \Delta t \frac{dv_a^n}{dt} + 0.5\Delta t^2 \frac{dv_a^n}{dt} \tag{4.3}$$

$$\rho_a^{n+1} = \rho_a^{n-1} + 2\Delta t \frac{d\rho_a^n}{dt} \tag{4.4}$$

In which the F_a and D_a are calculated according to the artificial viscosity scheme and continuity equation [Domingues et al., 2018]. This is calculated for every time step. Though once every 50 time steps variables are calculated according to:

$$v_a^{n+1} = v_a^n + \Delta t F_a^n \tag{4.5}$$

$$r_a^{n+1} = r_a^n + \Delta t \frac{dv_a^n}{dt} + 0.5\Delta t^2 \frac{dv_a^n}{dt} \tag{4.6}$$

$$\rho_a^{n+1} = \rho_a^n + \Delta t \frac{d\rho_a^n}{dt} \tag{4.7}$$

This part is designed to stop the divergence of integrated values through time as the equations are no longer coupled. If numerical instability is an issue it may be sensible to increase the frequency at which the second part of this scheme is applied.

The Dualsphysics module can be solved with GPU. This means a lot of processes can be calculated at the same time. The advantage of GPU over CPU is that with a GPU lots of computations can be processed in a parallel way. With CPU this amount is limited to the amounts of cores that are available.

The GPU implementation presents some key differences in comparison to the CPU version. One GPU execution thread computes the resulting force of one particle performing all the interactions with its neighbors.

The pier and the deck are designed as SPH particles. These particles are given the properties of concrete and are bound to each other en thus resemble a solid structure with the characteristics of concrete or any other given properties.

In the 2D model, the pier has to be designed as a solid. This pier has to be made as small as possible to not disturb the fluid-solid interaction between the fluid particles and the deck. Some problems occurred here

since the pier should be as small as possible so it would affect the water the slightest. The particles were placed in a Cartesian grid at an initial stage. The size of the bridge pier was dependent on the particle size.

A gap occurred between the fluid and the rigid particles. Rigid particles were given a higher mass and thus have a larger density. Therefore, the force on their neighboring fluid particles is larger and a gap occurs. This influenced the buoyancy force of the bridge deck. This effect could be mitigated by modeling with smaller particle sizes and this would directly affect the runtime.

4.1.2. LS dyna

The SPH model in LS-Dyna is based on a WCSPH model. This works with a pressure constant which is dependent on the speed of sound in the equation of motion.

Boundaries in LS-Dyna are resolved as SPH symmetry planes. This means that from the other side of the plane particles with the same characteristics (speed, mass, etc) react with the particles that are interacting with the boundary plane.

In LS-Dyna an artificial viscosity is introduced when a shock is present. Shocks introduce discontinuities in functions. The role of this artificial viscosity is to smooth the shock over several particles. An artificial viscous pressure term Π_{ij} is added such that $p_i = p_i + \Pi_{ij}$ [Hallquist, 2006].

In LS-Dyna no turbulence model is applied for the small scale velocity fluctuations.

Sorting, in the SPH model the location of the neighboring particles is important. The sorting consists of finding which particles interact with each other at a given time. A bucket-sort is used which consists of the domain where the sort is performed. With this method of partitioning, the closest neighbors will reside in the same or in the nearest boxes. This method reduces the number of distance calculations and therefore computational time.

In LS-Dyna a simple classical first order scheme for time integration is used. The maximum time step for SPH is determined by the expression:

$$\Delta t = \frac{\alpha l}{c} \tag{4.8}$$

In which α is the Courant number, l is a characteristic length, and c is the sound speed [Tokura, 2014]. Although, multiple factors play a role in the determination of the time step like the element size of the solid structures in the model. Since these are modeled relatively large the normative time step is dependent on the SPH nodes.

LS-Dyna is known for its MPP (Massively Parallel Processing) capacities, MPP is a type of computing available for LS-DYNA that uses many separate CPUs running in parallel, each with their own memory to execute a single analysis. In order to solve large implicit SPH analyses. It is important to provide a good CPU scalability in order to accelerate the analysis and save computational time.

In LS-Dyna the particles are modeled as nodes. The contact algorithm which is applied between the SPH particles and the rigid body is called 'automatic node to surface'.

In LS-DYNA, a contact is defined by identifying what locations are to be checked for potential penetration of a slave node through a master segment. A search for penetrations, using any of a number of different algorithms, is made every time step. In the case of a penalty-based contact, when penetration is found a force proportional to the penetration depth is applied to resist, and ultimately eliminate the penetration. Unless otherwise stated, the contacts discussed here are penalty-based contacts as opposed to constraint-based contacts. In Figure 4.2 is schematized how propagating nodes react with a master surface.

Contact between the SPH particles and the rigid surfaces 'AUTOMATIC_NODES_TO_SURFACE' are modeled with the contact option where no friction factors are applied for the interaction between particles and solids apart from the interaction with the false bottom in which a bed roughness should be simulated induced by 2-5mm stones glued on the false bottom. A static friction of 0.5, a dynamic friction of 0.05 and an exponential decay coefficient of -0.01 is suited for this type of bottom, see section 4.3.2 .

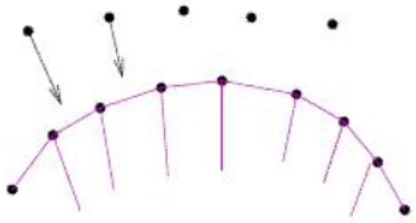

Figure 4.2. Node to surface contact in LS-Dyna [LSTC, 2019a]

The other important contact in the determination of failure is the contact between the bridge deck and the bridge pier. Especially the frictional behavior is important since this determines the moment of failure. An 'AUTOMATIC_SURFACE_TO_SURFACE' contact is used. The friction model between the surfaces is based on coulomb friction. In which static friction FS of 0.295 and a dynamic friction FD are allocated [LSTC, 2019b]. The counteracting penetration force is determined by the stiffness of the materials and the penetration depth. Since the stiffness of ABS that is used in the model is rather large (3GPa), a soft constraint penalty formulation approach is used [Hallquist, 2006]. In this approach a softscale (SOFSCL) of 1E-6 is used to compensate the instabilities which are formed by the large stiffness of the material.

The contact between the deck and the bottom is defined as 'AUTOMATIC_SURFACE_TO_SURFACE' contact with a static and dynamic friction parameter of 0.9 which is higher than a Coulomb based surface to surface friction of the two materials. A high value is chosen since the bridge hits the bottom in an angle and is than immediately stopped by the coarse pattern of the stones.

4.2. Model comparison LS-Dyna/Dualsphysics

At the start of this research, two different software's were used to run the SPH modules, Dualsphysics and LS-Dyna, these models were modeled parallel and at a certain point the models were compared to each other and one model is chosen to optimize for the use of this study. Important aspects of this study are the hydrodynamic behavior of the fluid particles and fluid-structure interaction. The results of both models until the point that the decision is made to continue with the SPH module by LS-Dyna are displayed in Appendix C.

A major difference between the different models is the fluid-structure interaction. In LS-Dyna all the contacts between different elements of the model can be defined with its own characteristics. The structure can be modeled as a rigid structure and the fluid is defined as particles.

In Dualsphysics a rigid-solid is build up out of SPH-particles in a cartesian grid. The size of the rigid is very much dependent on the resolution of the particles. Since there is a gap between the fluid and the structure it gave difficulties to get the buoyancy (density and volume) at the right value. There are options to make this work by making a dynamic flow inlet that has fewer particles as result and therefore refines the resolution of the particles which has a positive effect on this density problem in the model.

The numerical SPH model which is used in the rest of this thesis is made in the finite element modeling (FEM) software package LS-Dyna. Dependent on the number of particles the 3D models will be computationally expensive, therefore it is tried to get useful results from the 2D models so no run time will be wasted on unnecessary 3D runs.

4.3. Sensitivity of LS dyna model

In this section, some sensitivity analysis are executed to see what parameters will be the best fit for this research. Different sensitivities have been executed, to start with different particle sizes followed by a roughness level of the bed and thirdly, the size of the opening of the gate. Different outcomes of these analyses are compared to the lab data: hydrodynamics, forces on moving deck, forces on constraint deck and movement of the deck.

It is chosen to take the d70h30 case as reference case since here the bridge is failing due to a large broken wave, apart from the hydrodynamics the movement of the lab test and the model can be compared as well.

4.3.1. Particle size

Three different particle sizes are tried in this analysis, 3mm, 5mm and 10mm. The particle size determines the run time of a model for a significant part. The runs are all performed with a 31 core computer. For reference, the height of the bridge deck is 30mm.

The model with a particle size of 3mm has 444 907 SPH particles and a total runtime of 5 hours and 25 minutes. The model with a particle size of 5mm has 160 763 SPH particles and a total runtime of 1 hour and 1 minute. And the model with a particle size of 10mm has 40 474 SPH particles and a runtime of 6 minutes.

To compare the different models, two simulations for each case have been run. One with a moving deck to analyze the bridge movement and one with a constraint deck to analyze the forces on the deck over time. These forces can then be compared to the analytically calculated forces in chapter 3.

In Figure 4.3 the wave heights near WG1 can be compared. The maximum levels of the lab test, dp3, dp5 and dp10 are respectively 0.168m, 0.195m, 0.189m and 0.188m. The case in which the particle size is 10mm the measurement of the wave height is more coarse. If it is assumed that the maximum wave height measured in the lab test is taken as normative than the total water level of the three model cases are respectively 2.7cm, 2.1cm and 2.0cm off. In a local water level of 28.9cm, this has an error of 7.3%.

The water level at WG6 is harder to compare since the wave is already broken and the water level data is really scattered because of the way the water heights are extracted from the LS-Dyna software. Therefore, this data is not shown.

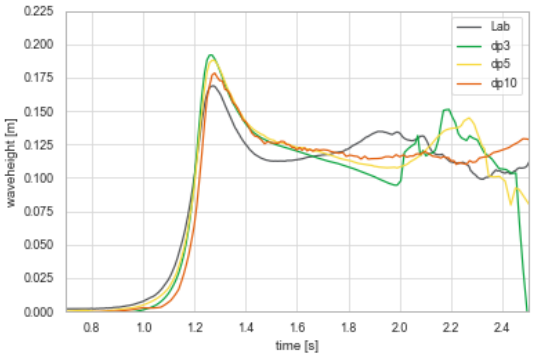

Figure 4.3. Waveheights at WG1 with different particles sizes compared to lab test.

The forces which are shown are extracted from a model in which the deck is a constraint. In Figure 4.4 the forces are normalized over a one meter bridge width. The calculated analytical forces for this case, determined with the use of [Cuomo et al., 2007], are $F_{qs1/250}$ is 45N and $F_{qsmax1/250}$ is 110 N. The analytically calculated forces are overestimated, though the quasi-static force which is present after the peak force is close to the model outcomes for the cases with 5mm and 3mm particle size. See Figure 4.4. The 10mm case gives lower values for the forces along the whole initial time span which makes the large particle size less suited for this research.

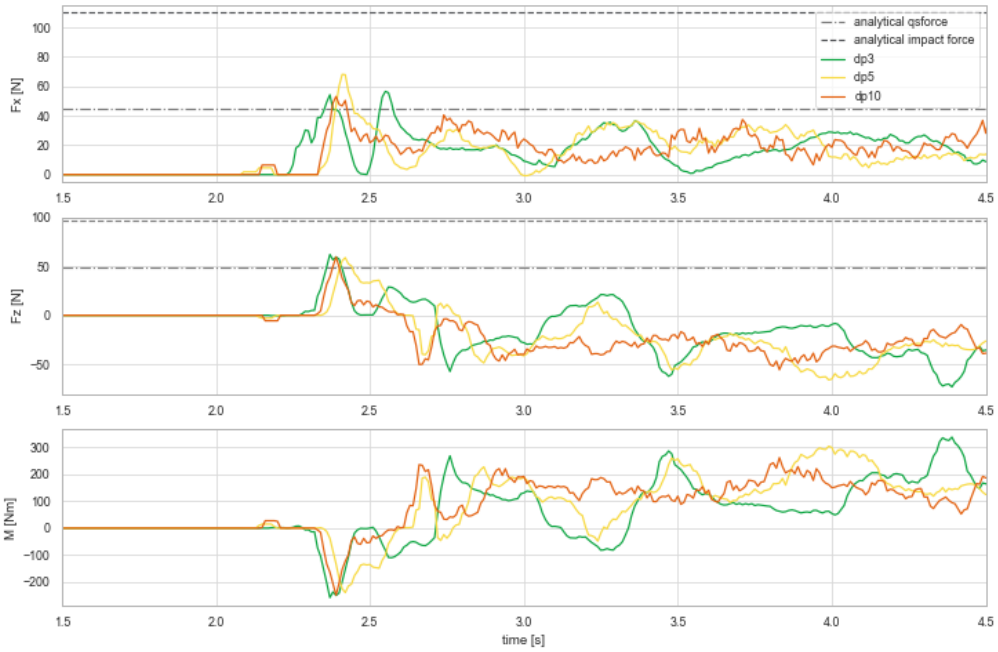

Figure 4.4. Forces on the bridge deck for different particle sizes.

The gray lines in the figures are the analytically calculated forces for the case d70h30. As can be seen, they are as in the figure with horizontal forces overestimated.

In Figure 4.5 the path of the center of gravity of the deck is shown, for reference the movement of the center of gravity of the deck during the lab test is displayed.

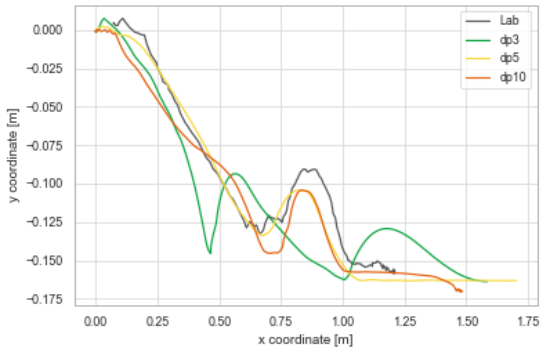

Figure 4.5. Movement of deck with different particle sizes.

It can be concluded that the movement of the deck in the case with particle size 10 mm and 5 mm is according to the lab test.

We will move on with the model in which a particle size of 5mm is used. The smaller the particle size the closer the model simulates the real-life case. Though the run times should be realistic. The model with a particle size of 5mm has a duration of approximately one hour which is acceptable to do multiple simulations with for the analysis in this research.

4.3.2. Roughness of the bed

During the lab tests, a rough bed is used. This causes waves to slow down. A rough bed has an effect on the shape of the wavefront. This roughness has an effect on the wave, especially when the water levels are low. It is not possible to model this turbulence that occurs near the bed in the SPH model. Though, a function exists in which the friction between the particle nodes and the solid false bottom can be defined:

$$\mu = F_D + (F_S - F_D)e^{-D_C * v_{rel}} \tag{4.9}$$

In which μ is de coefficient of friction, F_D is the dynamic coefficient of friction, F_S is the static coefficient of friction, D_C is the exponential decay coefficient and v_{rel} is the relative velocity. DC should be a negative value since the friction coefficient has to become higher in case the relative velocity increases. This is when assuming F_S is bigger than F_D.

Since the stone size diameter is not directly related to this formula some variants need to be tested to see how this friction formula can be applied in the best way.

Variant 1, F_S = 0.1, F_D = 0.05 and D_C = -0.01. These factors are determined when assuming maximum particle velocities near the bottom of 3m/s. With such a small dynamic coefficient of friction, the friction near the bottom will constantly be around 0.1. In this case, it is seen that near the bottom after the particles reach a certain speed they completely freeze. When this happens, the bed reacts as if it is one dp higher and the reaction to this layer of fluid particles is dependent on the viscosity of the fluid.

Variant 2, all the friction parameters are taken as 0. In this case, no friction is present between the false bottom and the liquid particles.

Variant 3, F_S = 0.01, F_D = 0.005 and D_C = -1. In this variant, a more dynamic approach is applied. The static friction is chosen as a low value, but the dynamic friction coefficient has an important role since the D_C is high. If the relative velocity is 3m/s the friction coefficient is also 0.1.

Variant 4, F_S = 0.5, F_D = 0.05 this just has an even larger static friction compared to case 1. The exponential decay coefficient will be -0.01 again so the varying relative velocity stays low.

variant 5, F_S = 1.5, F_D = 0.5 and D_C = -0.01. The friction near the bed is simulate as a high friction.

In the case of high frictional parameters, no movement of the particles near the bed occur. This means physically that the bed level is one dp higher and the viscosity between the fluid and the 'new' boundary conditions is the viscosity of the fluid. Only at the location of the gate where extreme high velocities occur the particles move along the false bottom. When the effect of this node to surface connection is just that the water height is different. This can have an effect on wave height and wave speed. It is important to compare the wave speeds to the lab tests since this has a large effect on the forcing on the deck.

From Figures 4.6 and 4.7 it becomes clear that with higher friction near the bottom a higher match occurs between the model and the lab test.

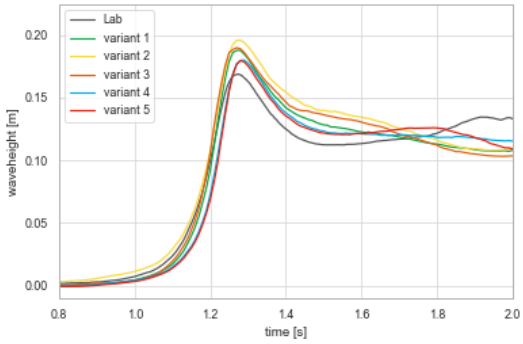

Figure 4.6. Hydrodynamics WG1 for different node to surface contact definitions.

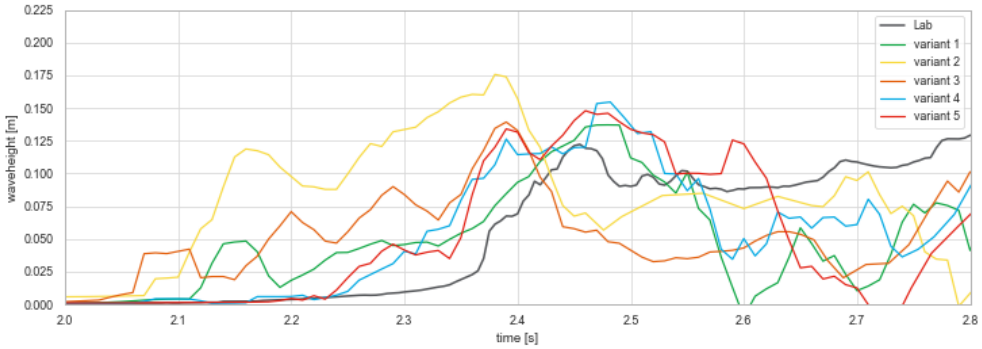

Figure 4.7. Hydrodynamics WG6 for different node to surface contact definitions.

Apart from wave height wave speed is also an important aspect that is dependent on the friction between the bottom and the fluid layer. As can be seen in Figure 4.7 variant 2 without any friction arrives first at WG6. Variants 1, 4 and 5 resemble the wave speed of the lab tests reasonable. Since the wave heights are still too high the wave speed will also be too high.

In this section, no forces or movements are discussed because the effect of the bottom friction only directly affects the hydrodynamics. Since the hydrodynamics change, the forces and therefore movements of the deck also change. In some cases the bridge deck is in a horizontal position on the bottom surface, When this happens there can be a layer of fluid particles between the deck and the bottom. In case this happens in a non-frictional model. The deck can slide frictionless in the horizontal direction. Since the best results are from the tests with large frictional coefficients, the final run will be run with the frictional coefficients from variant 4.

4.3.3. Opening of the gate

Since there is some insecurity about the opening of the gate there has also been done a sensitivity analysis on the size of the opening of the gate since this is a direct influence on the wave height and wave speed since this determines the discharge of the water coming into the basin.

The maximum opening of the gate is 15cm since this was the size of the opening. It is observed that not in all cases the door was fully opened. So three cases are investigated to see the sensitivity of this parameter.

Hydrodynamics

The differences with regards to wave height are significant. With a gate opening of 0.13m, the maximum wave height at the location of WG1 is 0.179m and in the case in which the gate opening is 0.15m the wave height is 0.191m. Additionally, the speed of the wave is different because of these wave height differences. It can be seen that the wave heights and wave velocity are most accurate in the case of a gate opening of 0.13m.

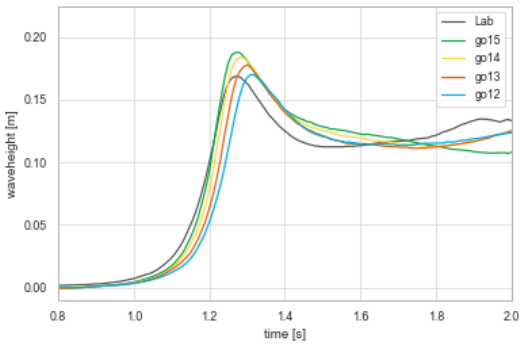

Figure 4.8. Hydrodynamics WG1 with different gate opening sizes.

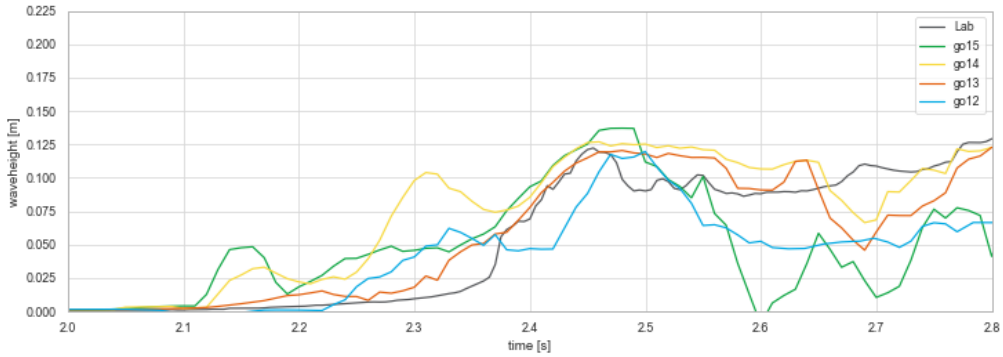

Figure 4.9. Hydrodynamics WG6 with different gate opening sizes.

4.3.4. Conclusion

In the first sensitivity study about the particle size, a trade-off has to be made between a longer run time or more accuracy in the results. The outcome that suited this research best is the 5mm particle size. The run times of the model were still manageable in range of 50 minutes and also the results were close to the lab tests. The second sensitivity study was about hydrodynamics. The behavior between the fluid and the false bottom which had a rough bed during the lab tests were modeled in different ways to discuss the outcomes and see which is the most accurate. The conclusion of this study was that a high roughness was most accurate independent of the exponential decay coefficient. A last sensitivity is done with regards to the insecurity about the opening of the gate, four different runs have been done and the conclusion is that an opening of 15cm, which should be the size, is not representable of the real case that is executed in the lab tests. An opening of 13 cm would be more accurate as the opening size. In addition to this, from the movies of the test, 2cm blockage of the opening by the gate that did not open fully seems correct. With the knowledge of these sensitivity analyses, a final model has been developed to run all the cases with different tank and basin heights. The final validation of this model is displayed in the following sections.

4.4. Other variables

During the laboratory wave tests, a wave damper was placed at the back of the flume to withstand the reflection of wave and backwaters due to flows. This damper could not be reproduced in LS-Dyna. Therefore, the wave flume is made 2m longer to eliminate these reflective effects. A wall is placed with the same height as the initial water level so that no water can flow out in the initial phase. When the wave arrives the water level will be higher, and the excess water will flow out of the calculation domain.

4.5. Validation of the final 2D model

After opening the gate a turbulent field will occur behind the bridge. This is displayed in Appendix E.1. As can be seen from timestep t = 0.49s to 1.29s some air bubbles occur in the water directly behind the gate. This is a phenomenon that cannot occur in reality. A vacuum will occur and this will make sure the water stays connected. In SPH air is not modeled as particles but as empty space so no additional air pressures are present in the model. Though it is possible to model air in a so-called two-phase model, this requires even more computational power since a lot more particles need to be calculated.

In Figure 4.13 the final model of the SPH model and the Waseda test of the d70h30 case are displayed next to each other.

4.5.1. Hydrodynamics

The results of the hydrodynamics in the final case that is used for validation are displayed in Figures 4.10 and 4.11. At WG1 the maximum wave height is 0.169m during the laboratory tests and in the SPH tests, it was 0.171m. At WG6 the wave height in the laboratory tests was 0.122m and in the SPH model, it is also 0.122m. As can be seen in Figure 4.11 the speed of the wave and the water level when the wave is passed are not completely similar.

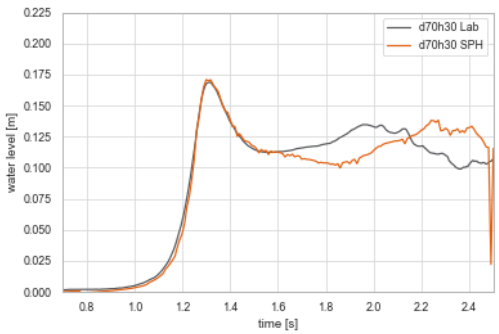

Figure 4.10. d70h30 WG1 water height.

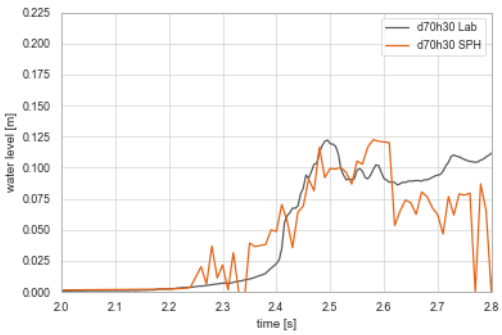

Figure 4.11. d70h30 WG6 water height.

In Figure 4.10 the shape of the water height near wave gauge one is accurate till the moment after the wave peak. Then the water heights are somewhat different. A possible explanation for this could be the turbulent air bubbles that occur behind the opening in the gate. In reality, no air voids occur in the water and therefore some vacuum areas will form which affects the water surface. In this SPH model, this is not modeled and therefore the water behaves in a way that does not match reality.

4.5.2. Forces on deck

The 1/250 exceedance forces are calculated by the method of [Cuomo et al., 2007] explained in section 3.4. These analytical forces are expected to be a lot higher than the forces that are calculated by the model since these are 1/250 exceedance forces. The forces shown in Figure 4.12 are extracted from a model in which the superstructures movement is constraint in all directions. All the force figures displayed in this report are the resulting forces from the SPH fluid particles on the bridge deck, no deck-pier or deck-bottom forces are displayed. As is displayed in Figure 4.12 it can be observed that an initial impact force is present after which a quasi-steady flow occurs because of the wave movement. Thereafter the water level difference before and behind the wavefront causes a flow of water which results in the force over a longer time interval.

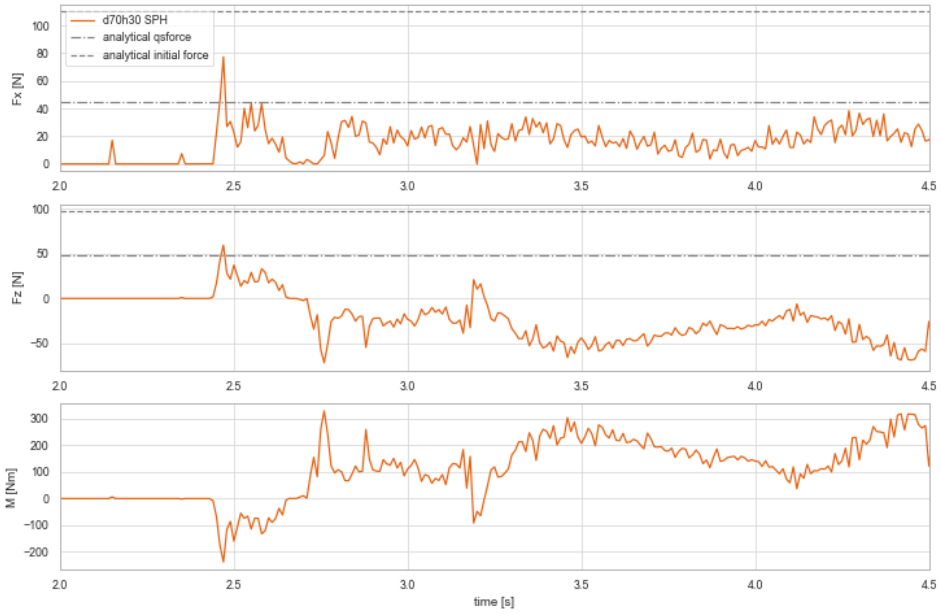

Figure 4.12. Forces on the bridge deck for the d70h30 case.

The vertical forces are also calculated analytically by the method of [Cuomo et al., 2007]. This resulting force is significantly higher than the calculated force as can be observed in Figure 4.12. It is clearly visible that the wave results in a positive (upward) force and the flow that follows results in a negative (downward) force on the bridge deck. This means that the initial wave is more likely to cause the superstructure to fail.

From LS-Dyna the resulting moments on the whole superstructure can be determined. This is displayed in Figure and 4.12.

4.5.3. Movement of bridge superstructure

The movement of the deck is extracted from the movies of the lab tests and can be compared to the movement of the deck in the SPH model. This movement of the deck is displayed in Figure 4.14. The path of the decks are comparable, only when the bridge deck in the model hits the bottom it is not turning directly. This can be the result of an inaccurate friction factor between the bridge deck and the bottom or fluid particles can be stuck between the deck and the bottom which makes the deck sliding along the bottom without interacting

directly with the bottom.

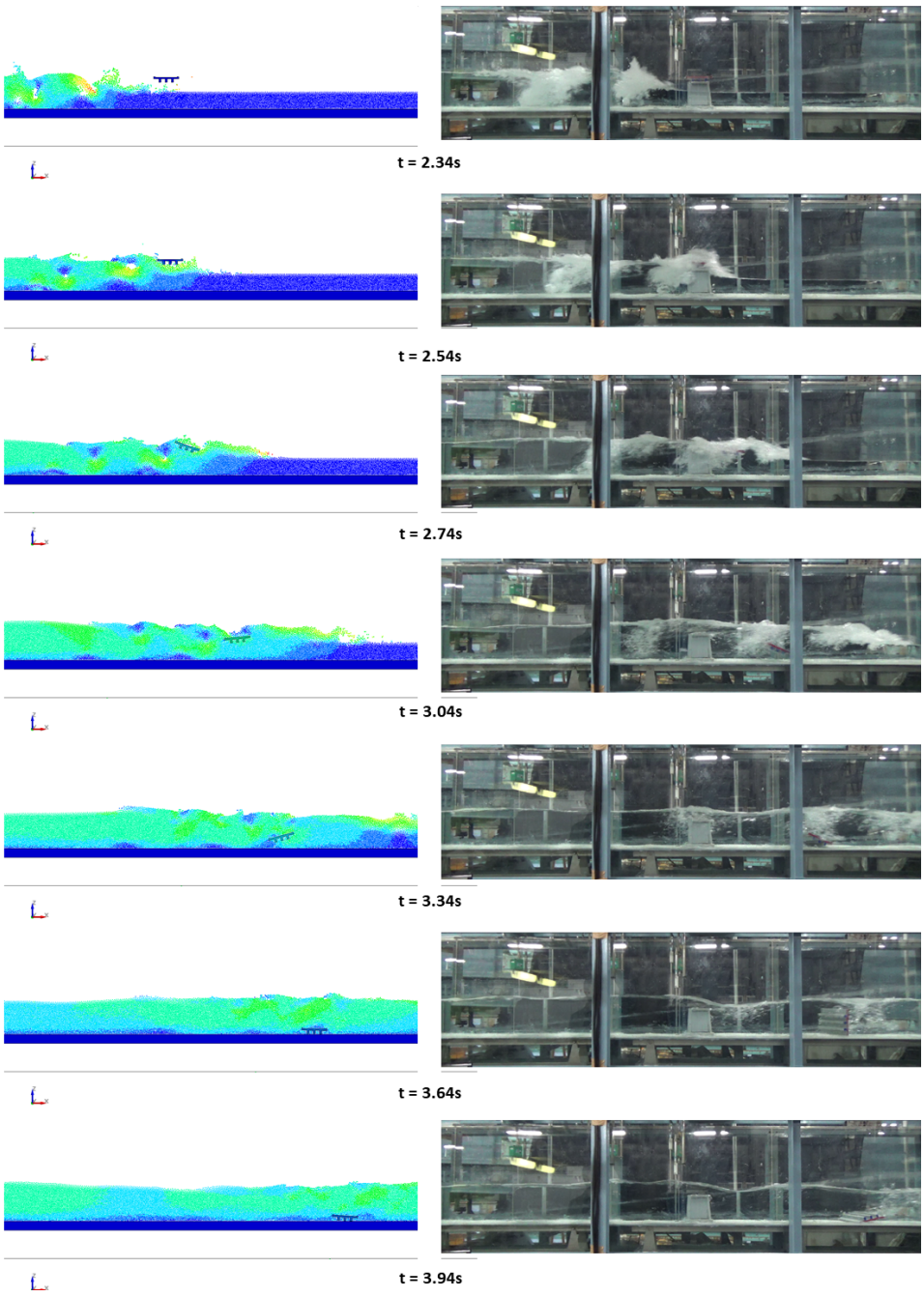

Figure 4.13. Movement of bridge deck for d70h30 case, numerical simulation (left), and physical test (right).

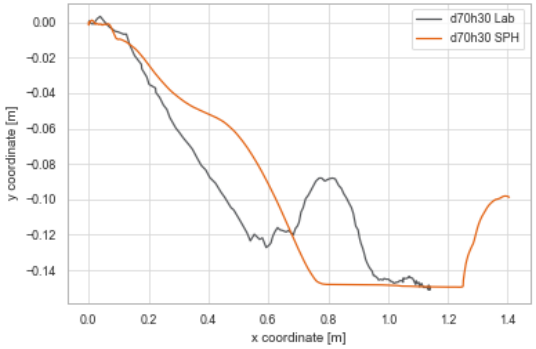

Figure 4.14. d70h30 resulting deck movement.

4.6. 3D model

The transition from a 2D to a 3D simulation means that the wave flume needs to be 40cm wide and the bridge has two piers underneath which restrain the free fluid flow through the wave flume. In some cases, these changes could have more effect than in other cases. The effect of this change is dependent on the failure mode as well as on the cause of failure. In the lab tests, it was evident that sometimes the bridge fails at wave impact and in some cases, it fails after impact while there is a strong fluid flow against the bridge. For this validation, the d70h30 case is run. The main failure mode, in this case, is caused by the wave impact. Therefore, not much difference is expected in the failure mode of the bridge.

The 3D model is constructed with water particles with a size of 10mm, this is twice as large as the particles of the 2D models used in this research. The run time of the model took 14 hours. If the same particle size as in the 2D models was used, this would be scaled up with a minimum of factor 8, dependent on the difference in the time-step this factor could be even higher. These runs would not be manageable any more to do a qualitative analysis with.

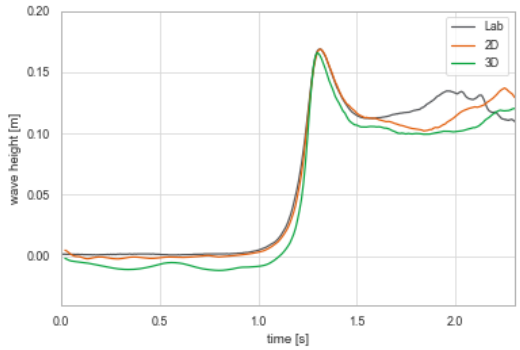

Figure 4.15. WG1 comparison 2D versus 3D for d70h30 case.

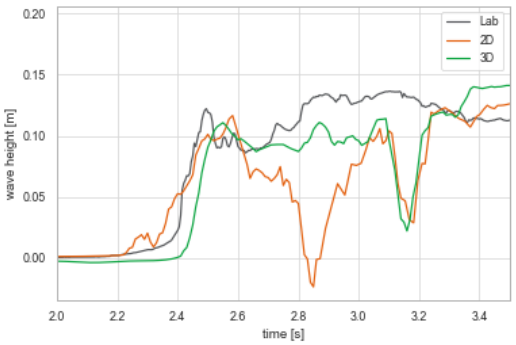

Figure 4.16. WG6 comparison 2D versus 3D for d70h30 case.

From Figure 4.17 the deck is exposed to a high impact force and slides of the deck. Then it hits the bottom still in flat position. The vertical force keeps pretty high since there are water particles between the deck and the false bottom. When deck gets stopped by the friction by the bottom. again a large horizontal force by the fydrodynamics is created (around 3.3s for 2D and 4.5s for 3D).

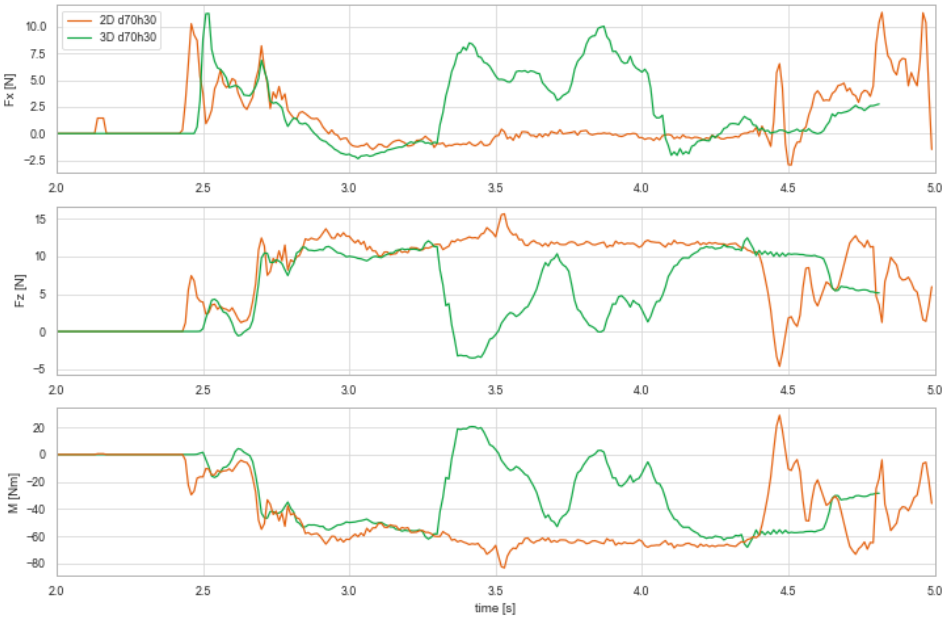

Figure 4.17. Forces on moving bridge deck comparison 2D-3D for d70h30 case.

As expected, the peak force that introduces the vertical movement in the deck is somewhat different (see Figure 4.17) in the 2D case relative to the 3D case since the flow is confined at the location of the bridge piers.

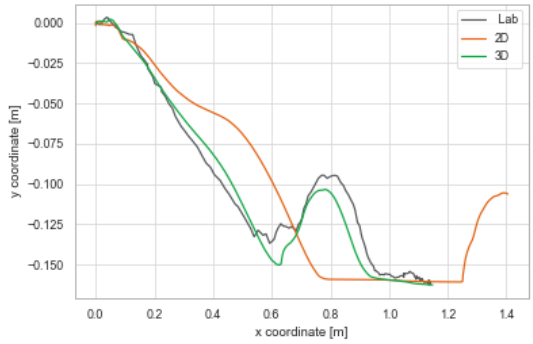

Figure 4.18. Deck movement.

In the 2D model, the deck stays flat after sliding off the pier. When it hits the bottom, the deck is still flat and starts sliding. Then, when the friction between the deck and the bottom creates a rotational point the deck will rotate. In the 3D model, the deck is sliding off the pier in a similar manner. The deck is in a slight negative angle when it moves towards the bottom. Only the right point of the deck hits the bottom and rotation occurs immediately without sliding over the bottom.

The differences between a 2D and a 3D model are clearly visible in Figure 4.19 especially in the last frames it is clear that there is some confinement of the fluid flow and therefore the water will locally have a higher velocity and the water level will decrease. This situation is comparable with steady fluid flow. As can be observed in the first few frames of Figure 4.19 the fluid behavior does not differ much, it only looks somewhat wilder since in the 3D model only the closest particles against the flume wall can be seen.

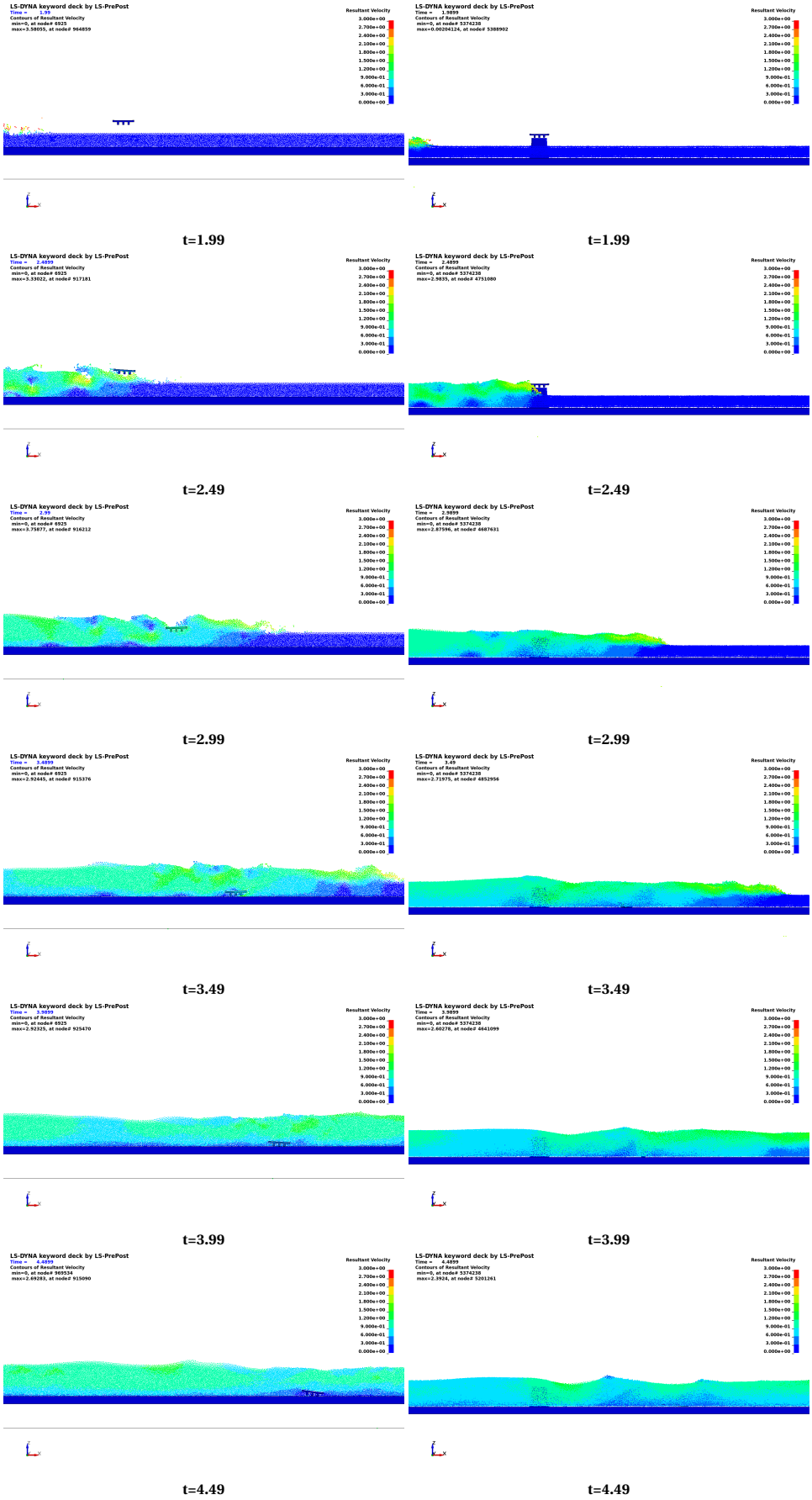

Figure 4.19. Differences between 2D (left) and 3D (right) model.

4.7. Full scale model

After scaling the geometry with a factor 37 some other parameters have to be scaled as well.

When scaling the model to real scale the Froude scaling (Equation 2.30) is applied. This influences the maximum flow velocities by a factor of $\sqrt{37}$ and thus the equation of state for the determination of the relationship between density and pressure changes as well. The initial value of k_0 is determined by equation 2.60. In the scaled situation k_0 is 1.5e5 based on a maximum velocity of 3.25m/s. In the full-scale simulations velocities are theoretically raised by a factor $\sqrt{37}$ which means k_0 is scaled with a factor 37. This results in k_0 = 5.55e6.

For the determination of a scale factor of the forces, Equation 2.5 is taken as reference. This equation states that the force is dependent on the drag coefficient, geometry squared and the velocity squared. [Naderi, 2018] stated that the drag coefficient remains the same in steady flow when scaling is applied. It is assumed that this is true for a dam break wave as well. Froude force scaling means that the velocities in a real scale model are $\sqrt{37}$ times as fast than in a 1:37 scaled model. Since the forces displayed in the Figures in this research are presented as Forces per meter width of the deck, the scale factor is $\sqrt{37}^2 * 37 = 1369$.

In Figure 4.20 and 4.21 the Lab scaled simulations have been scaled with the scaling factors obtained above, so the time is scaled by $\sqrt{37}$ and the water level is scaled by 37.

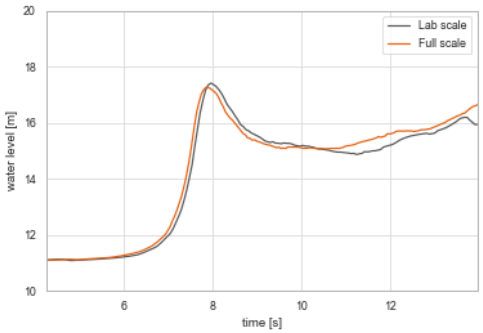

Figure 4.20. WG1 comparison full scale-lab scale for d70h30 case.

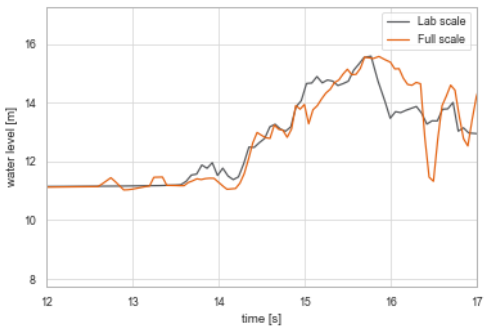

Figure 4.21. WG6 comparison full scale-lab scale for d70h30 case.

The figures do not show exact representation since there are more scaling laws like the Reynolds number that cannot be met all at the same time. Weber number is of none importance since no surface tension is present in an SPH model.

The forcing is plotted in the same manner only here the force is scaled with a factor 1369.

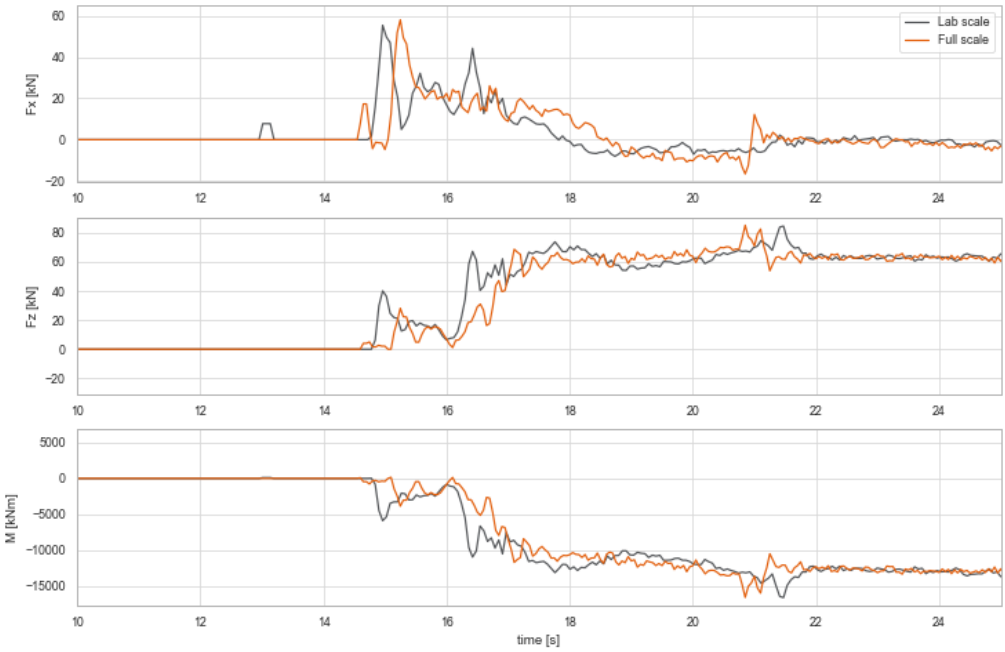

Figure 4.22. Forces on moving deck for different scales in d70h30 case.

From these figures the Froude scaling is represented really well, only the time step is not 100% accurate.

Since the forcing is quite accurately scaled the deck movement of the bridge also has a similar path. Which is shown in Figure 4.23. If this is compared to Figure 4.14 It can be observed that the deck movement of the full-scale case is closer to the deck movement. Though, this cannot be explained at the hand of the scale factors.

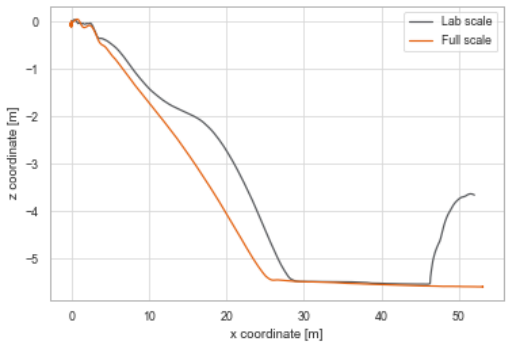

Figure 4.23. Movement of bridge deck in different scales for d70h30 case.

The other dimensionless scale factors are of importance in a scaled model as well. The Reynolds number is related to the amount of turbulence that occurs in the water.

Since the most important dimensionless scaling factor in this model is the Froude number, the Reynolds scaling cannot be met. The flow velocity is scaled by $\sqrt{37}$ and the length scale is scaled by 37. The kinematic viscosity of the fluid is in both scale models the same. This results in Reynolds numbers in the full-scale model which are 225 times as high as the lab-scale. The laminar-turbulent transition usually occurs when Re

$= 5 * 10^5$ at locations where the low fluid velocities occur the Reynolds effect has a significant scaling effect. Since there is not a constant flow velocity in the flume in a dam break test it is hard to determine the exact locations where this scale effect plays a clear role.

No surface tension model is present in the SPH model, aggregation of particles cannot be seen because of the lack of the surface tension effect. To get the behavior of water in splashing models this could be of importance. The Weber number is dependent on surface tension. This cannot give any scaling effects.

4.8. Discussion

The differences between the laboratory tests and the numerical models can have multiple reasons, the most obvious would be that the numerical model is not capable to simulate the reality perfectly. A numerical model is always a schematization of reality, SPH particles are originally not designed to have interaction with boundaries or rigid structures like bridges. The friction between the fluid and false bottom is modeled in a way that it is calibrated to the exact wave height of the lab test. To simulate the realistic behavior of the bed this bottom can be modeled as a very fine saw tooth to initiate interaction. Though, a sawtooth with a size between 2 and 5mm will not have much effect when the particles are modeled with a 5mm diameter.

The initial location of the deck is of importance, this location is determining the friction with the deck. This deck should have the same circumstances in every test. The opening of the gate in the lab tests is done with a mass that pulls the slide open. In the numerical simulations, the first frame is the complete opening of the gate. This small differences can have a significant effect to the results. During the lab tests, some leakage of the reservoir occurred which made it hard to execute the tests at the exact moment the water height was the one that is stated.

All these small inaccuracies can add up to large failure margins. The physical tests are now assumed to be the truth. Though, these tests also have their flaws. In this chapter, the validation of just one case is displayed. If the model was calibrated on a different case, there is a possibility that other parameters would have been chosen.

Forcing of waves on structures is for a large part determined by air which determines the impact forces on solid elements. In the SPH model, no air is present, air bubbles will occur but no pressure differences in this air will cause sudden impact forces.

5

SPH results and analysis

In this chapter, all the numerical simulations that are executed in this thesis are shown. In table 5.1 all the simulations that are run to obtain the answers to the research questions are shown.

In this chapter different analysis are displayed, varying water levels in the tank and basin, effects of shear keys on failure mode, effects of a seawall behind the bridge and the effect of an inclined bridge deck on the formed forces.

Table 5.1. Overview performed simulations in SPH

	d40h35	d50h35	d60h20	d60h25	d60h30	d60h35	d70h30	d70h35
clean	x	x	x	x	x	x	x	x
shear key back					x	x		
shear key middle					x	x		
seawall				x	x	x		
negative inclination					x	x		
positive inclination					x	x		
scaled							x	
3D							x	
boxgirder					x	x		
geometry sc1					x	x		
geometry sc2					x	x		
geometry sc3					x	x		
geometry sc4					x	x		
geometry sc5					x	x		
geometry sc6					x	x		
sacrificial beam					x	x		

5.1. Analysis varying water levels in the tank

The same analysis as in Section 3.2 has been performed with a 2D SPH model. From this chapter will follow if the SPH 2D model is suited to do these types of analysis.

5.1.1. Hydrodynamics

In Figure 5.1 and 5.2 the hydrodynamic conditions are displayed for the locations of WG1 and WG6. It is visible that the wave height and wave speed increase as the water level in the tank increases.

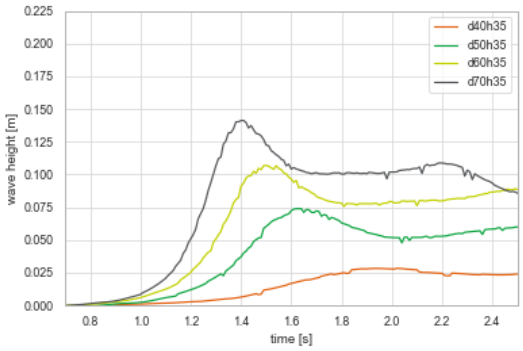

Figure 5.1. Wave heights at WG1 for various water levels in the tank and constant basin height.

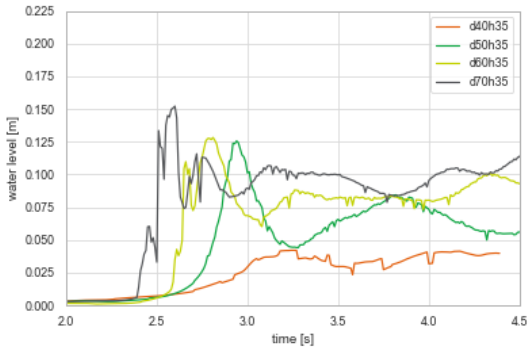

Figure 5.2. Wave heights at WG6 for various water levels in the tank and constant basin height.

5.1.2. Wave forces on bridge deck

The forces from the waves on the bridge are displayed in Figure 5.4. As expected, the maximum forces on the superstructure are higher when exposed to higher wave height. The wave forces are representative for a bridge deck of one-meter width. The maximum horizontal forces for the d40h35, d50h35, d60h35 and d70h35 are respectively 3.79N, 32.19N, 46.77N and 65.38N. Another aspect that stands out from these figures is when a wave is not fully broken yet, like the d50h35 case, the initial peak force is not very accurately visible in the graphs, but the force will gradually grow to its peak force.

5.1.3. Movement of bridge deck

The decks in this analysis all have their separate paths, as can be seen in Figure 5.3, the d70h35 case is clearly making a vertical lift after which the deck rotates and makes a downward movement. The d60h35 case is also making a clear horizontal movement but gains more horizontal distance when it moves towards the bottom. In the d50h35 case, the deck moves just enough to slide off the pier and then moves towards the bottom along with the flow. The deck did not display any movement in the d40h35 case.

In Figure 5.4 the displacement, acceleration and forces on the bridge deck are displayed. It can be stated from this that the initial impact force has enough energy to move the deck. Only in the d40h35 case. The frictional force is 13.2N and this is never exceeded in the d40h35 case thus this is not displayed. The data from Figure 5.4 are extracted from a case with a moving bridge deck, the forces that are shown are the resulting forces from the fluid particles on the bridge deck, no resulting forces from interaction between the deck and the pier or the bottom. Around 3.3s a large downward force can be observed that occurs when the bridge deck hits the bottom. The horizontal movement of the deck stops abruptly and the water mass travelling in the same direction pushes the deck in the flow direction.

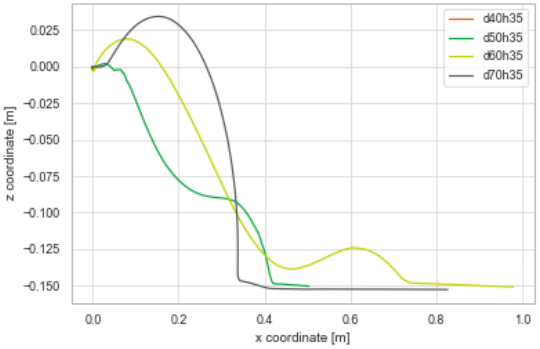

Figure 5.3. Movement of deck for different water levels in the tank.

Figure 5.4. X coordinate, acceleration and forces on moving bridge deck for different water levels in the tank.

Stated from this analysis can be that the wave height has a direct relation to the wave force on the structure. The horizontal force is not the only decisive factor in the distance the deck can travel. As can be seen in Figure 5.3 the orientation of the bridge to the flow is decisive of the interaction between the fluid particles and the deck.

From the lab test followed that if the water level in the tank was higher this resulted in larger wave height and therefore larger forces on the deck and the deck would cover a longer distance. From the results of the model, the same thing can be said about forces. Though, the distance covered by the bridge deck seems random. It looks like the traveled distance is dependent on the angle that the deck makes regarding the incoming flow.

5.2. Analysis different water levels in the basin

This analysis has been done for the laboratory tests in Section 3.3. And the same dam break properties have been applied in this section so the conclusions from the lab test can be compared with the conclusions from the numerical model.

5.2.1. Hydrodynamics

In Figure 5.1 and 5.2 the hydrodynamic conditions are displayed for the locations of WG1 and WG6. It is clearly visible that the wave height and wave speed increase as the water level in the tank increases. The results for the d60h20 case are strange since this is an incoming wavefront without the initial water level.

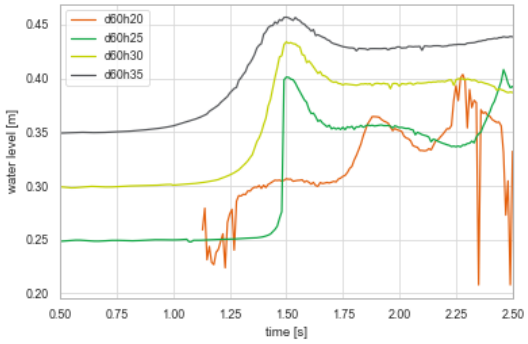

Figure 5.5. Wave heights at WG1 for various water levels in the basin.

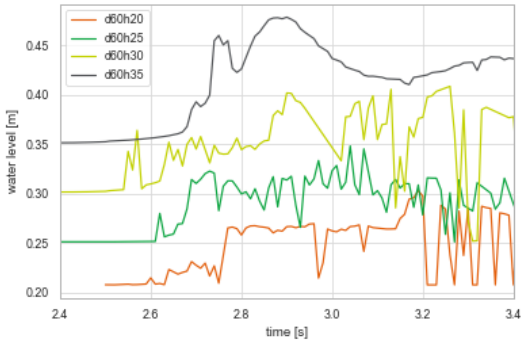

Figure 5.6. Wave heights at WG6 for various water levels in the basin.

From the figures can be concluded that in the d60h35 case the wave is not broken yet when it arrives at the bridge. This results in a larger timespan between the peaks of the waves between WG1 and WG6. In other cases, it is clearly visible that the wave is formed in a propagating bore since the signal is rough.

5.2.2. Wave forces on bridge deck

The forces from the waves on the bridge are displayed in Figure 5.10. As expected the maximum forces on the superstructure are higher when a higher wave height is exposed to the bridge. The wave forces are representative for a bridge deck of one-meter width. Since the wave in case d60h20 does not interact with the bridge, there are no forces displayed for this case. The maximum horizontal forces for the d60h25, d60h30 and d60h35 are respectively 28.73N, 67.16N and 46.77N. So, the largest wave does not result in the highest horizontal force. Meanwhile, when the vertical forces are analyzed the maximum vertical forces for the d60h25, d60h30 and d60h35 are respectively 48.58N, 38.19N and 98.60N It is clear that the d60h35 case has the largest vertical force.

From Figure 5.7 can be seen that the wave is roughly disturbed when it hits the bridge deck. No clear surging wave can be distinguished. Just after the wave hits the deck a high-pressure field can be seen at the front of the bridge. This results in the high horizontal force. In Figure 5.8 the sinusoidal waveform can be distinguished. The circular motion of the wave particles is disturbed by the bridge deck which results in the high-pressure field below the bridge. This results in high vertical and moment forces.

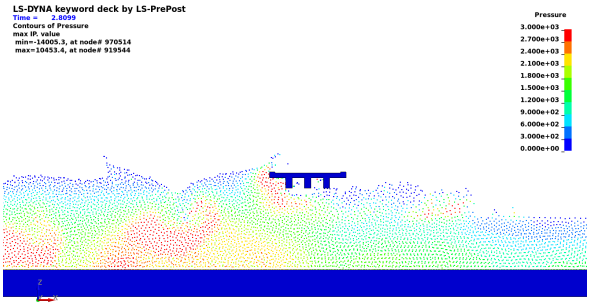

Figure 5.7. Pressure around bridge deck for d60h30 case

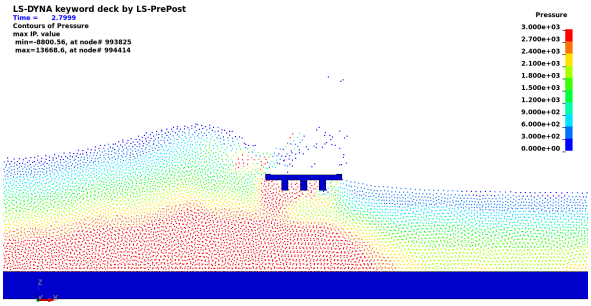

Figure 5.8. Pressure around bridge deck for d60h35 case

5.2.3. Movement of bridge deck

The bridge superstructure in the d60h35 case is clearly making a vertical lift after which the deck turns and makes a downward movement as shown in Figure 5.9. The d60h30case is sliding off the deck which is relatable to the large horizontal force which is created by the bore front. The d60h25 case results in a flow underneath the bridge deck. Sporadically a small wave hits the bridge deck which results in the uplift which takes place in a late stage. In Figure 5.10 the x-coordinate, acceleration in the x-direction and the horizontal force on the bridge deck are shown. As can be observed, the acceleration is a direct consequence of the forcing on the

bridge deck. Since the vertical forcing has its peak at the same moment as the horizontal forcing it is logical that the frictional force has little effect on the movement of the deck. Stated from this figure is that the deck starts moving directly when the peak force is hitting the deck. It is important to mention that the forces are extracted from a simulation with a constraint deck and the x-coordinates are extracted from a model with a moving deck.

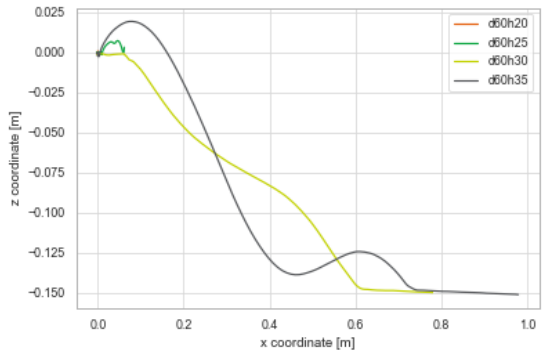

Figure 5.9. Movement of deck for different water levels in the basin.

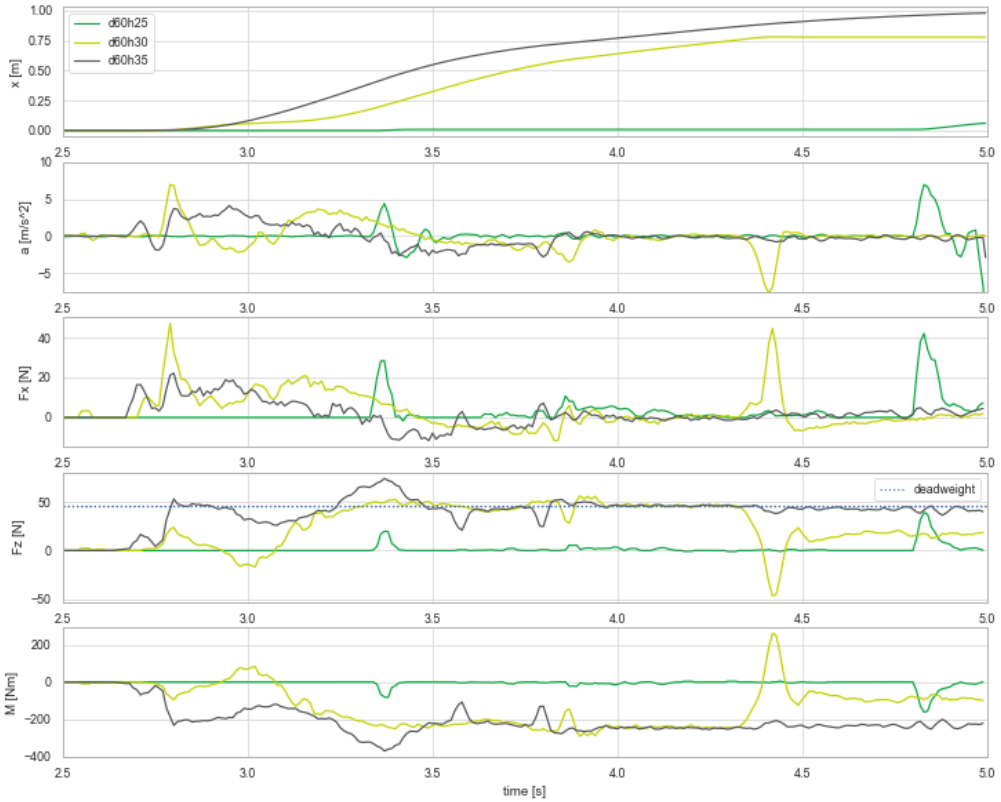

Figure 5.10. Forces on moving bridge deck for various basin heights.

Concluded from this analysis can be that the wave height does not have a direct effect on the wave force but that the phase of a nearshore wave is of importance in the determination of these forces. Also, the scale difference between impact force and quasi-steady force is different for a propagating bore and a surging wave.

In the lab test results, the d60h25 case also failed the bridge deck. Since this failure is rather a result of the flow resulting from the wave than from the wave itself, concluded has to be that in this case, 3D effects play a major role. The flume flow area is reduced and therefore the flow velocity and flow height is higher in the area of the bridge piers.

5.3. Analysis of the effect of shear keys

This analysis has been done for the lab tests in section 3.4. In this section, the results are presented regarding the numerical test results. The forcing on the bridge superstructure due to the wave hydrodynamics is similar to the wave forcing without shear keys. An interesting aspect is the movement of the bridge decks in case rigid shear keys are applied to the bridge. In the following animations, Figures 5.11 and 5.12 can be seen what the effect of the shear key is on the movement of the bridge deck. The first horizontal peak force can be withstood by the shear key. After this the vertical force will cause the rotation of the bridge deck, the horizontal quasi-steady force then contributes to this rotation. After the bridge deck rotated of the pier, the angle of the deck to the resulting flow is of influence for the path that the bridge deck will follow to the bottom.

5.3.1. Movement of bridge deck

In Figures 5.11 and 5.12 the difference is shown between a bridge with and without a shear key in snapshots of the simulation.

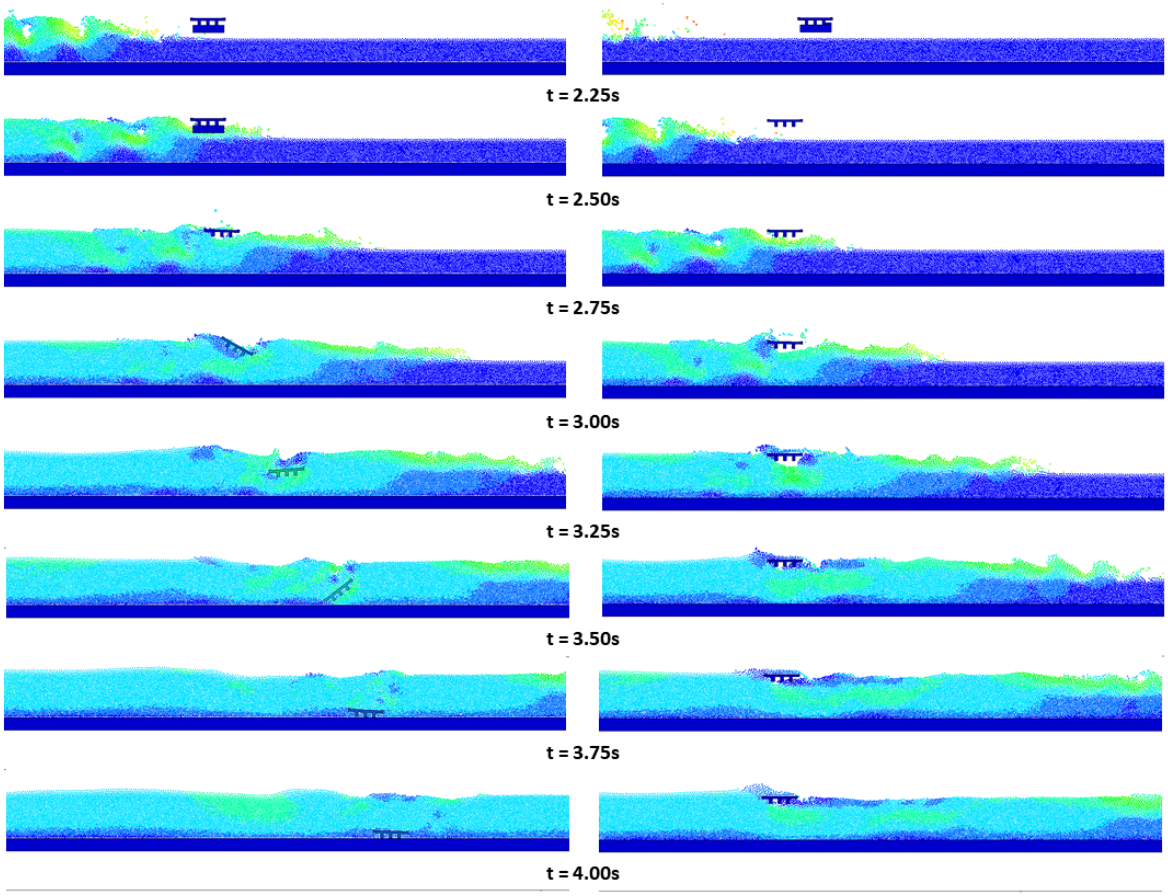

Figure 5.11. The failure of a bridge deck without shear key (left) and with a shear key (right) for the d60h30 case.

In Figure 5.12 it is clearly visible that the horizontal peak force is counteracted by the shear key. The vertical

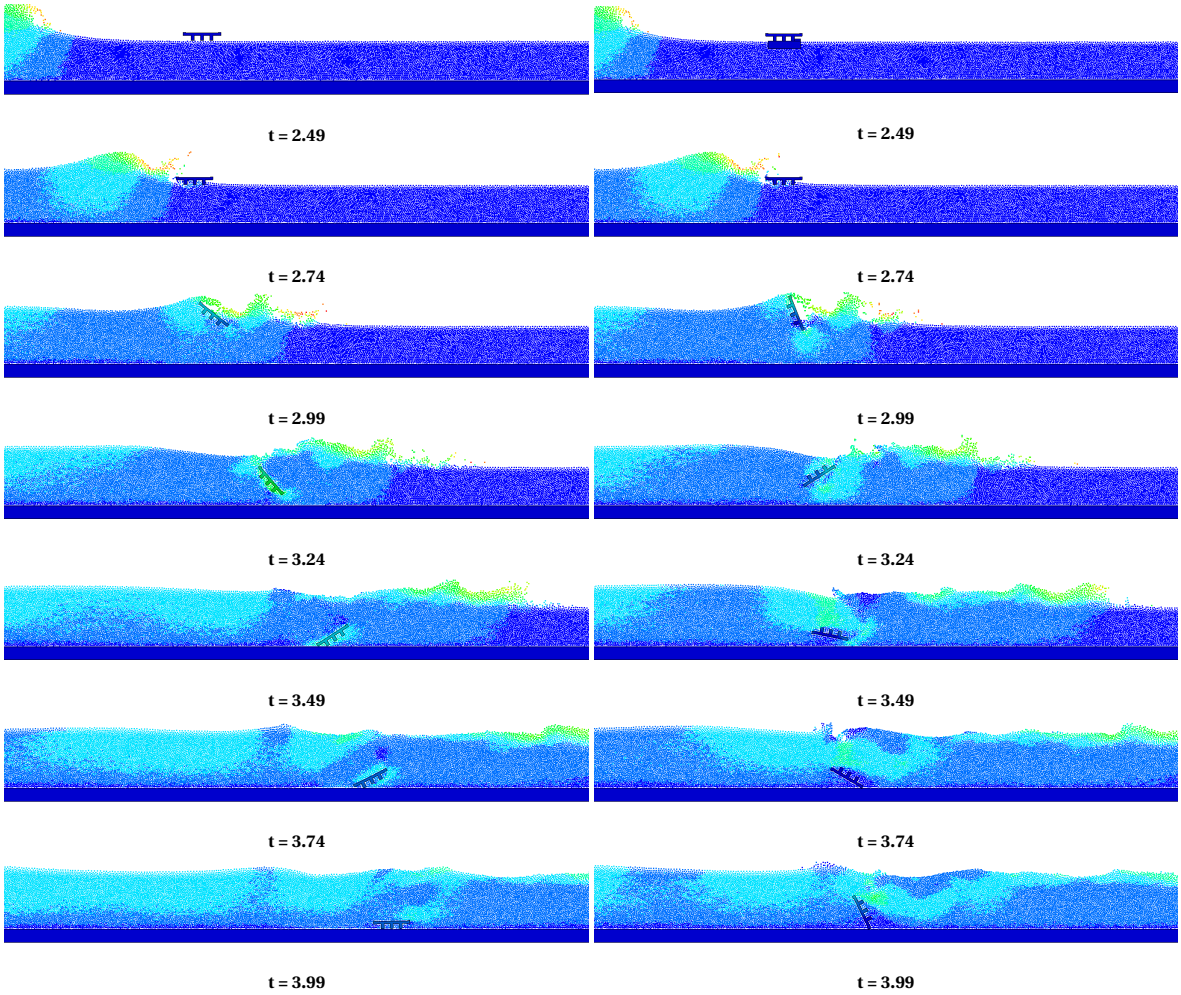

Figure 5.12. The failure of a bridge deck without shear key (left) and with a shear key (right) for the d60h35 case.

force has a substantial role and flips the deck in combination with the occurring quasi-static force. The acceleration on the deck is dependent on the forcing. Since the peak force is translated to the pier by the shear key, the acceleration of the bridge deck is induced only by the quasi-steady force. This results in a lower speed and therefore a smaller distance from the pier as can be observed in Figure 5.12.

The shear keys restrict the initial horizontal movement after which the vertical force is causing the rotation of the deck. When the shear key is behind the last girder, the deck has to make a 90 degrees angle before the horizontal movement can start. When internal shear keys are applied, this angles does not have to be 90 degrees. The difference in orientation when starting the horizontal movement has significant effects on the final location of the deck.

In Figure 5.14 is clearly seen what the effect of the shear key is on the movement of the bridge deck. The movement of the bridge deck in the d60h30 case was only horizontal which also followed from the resulting forces in Figure 5.10. The shear key resisted this horizontal force and the bridge only had a minor movement as a result of the incoming wavefront. For the d60h35 case, there was already an upward movement of the bridge deck. Since this vertical movement is not constraint by the shear key the deck still moves upward, only the horizontal movement is a constraint at impact, which results in less acceleration of the bridge deck and therefore the bridge deck did not travel as much horizontal distance.

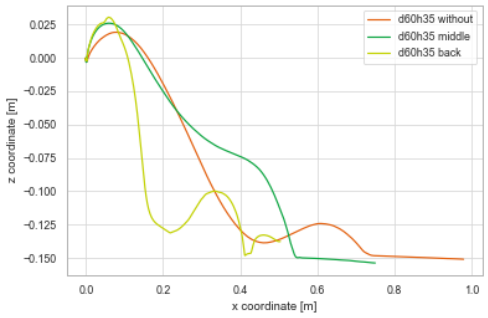

Figure 5.13. Movement of deck with different shear key layouts.

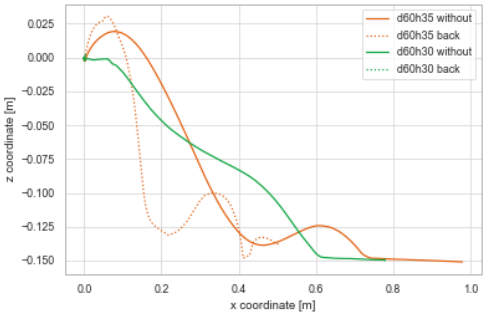

Figure 5.14. Movement of deck with or without shear key.

From this shear key analysis can be concluded that shear keys are a very good measure to constrain bridge deck movement from incoming wavefronts (d60h30). In case a non-breaking shallow water wave (d60h35) the resultant vertical forces are too large and the shear key does not have any effect on this.

5.3.2. Comparison conclusions laboratory results and model results

If the Figures 5.14 and 3.11 the results of the lab tests and numerical SPH model have a good fit. From the lab tests follows that the vertical movement in the case of the propagating bore (d60h30) is still present but not enough to result in a rotational movement.

The final statement that can be made about the shear keys, it is a good measure to withstand the horizontal movement of the bridge. Though it should be studied if the high forces due to the waves can be withstood by the shear key and if the shear key can withstand this if these forces can be transferred to the pier and the foundation without failure in these structures.

5.4. Analysis of the effect of a seawall behind the bridge

No physical lab tests have been done to the effect of seawalls behind a bridge. A single test has been done with a sea dike in front of the bridge, from this followed a supercritical flow over the bridge which did not interact with the bridge superstructure but only with the piers and foundation underneath. In this section, the effect of a seawall closely behind the bridge is investigated. In the following animation 5.15, it can be seen how the seawall is placed in all the cases and how the wave is confined between the bottom, the deck and the seawall which results in high forces on the superstructure.

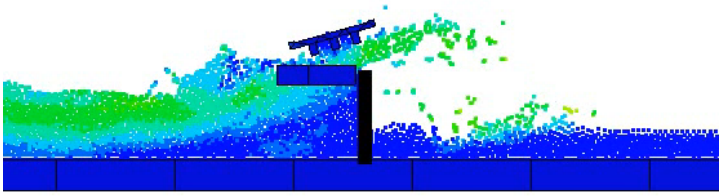

Figure 5.15. Movement of deck with or without shear key.

5.4.1. Wave forces on bridge deck

The forces from the waves on the bridge are displayed in Figure 5.16. The maximum forces on the bridge deck are significantly higher than in the cases without seawall displayed in Figure 5.10. These high forces occur because the wave is confined in the area underneath the bridge and before the seawall.

The maximum horizontal forces for the d60h25, d60h30 and d60h35 are respectively 53.76N, 49.75N and 32.24N. So, the largest wave does not result in the highest horizontal force. Meanwhile, when the vertical

forces are analyzed the maximum vertical forces for the d60h25, d60h30 and d60h35 are respectively 181.85N, 122.63N and 158.34N. In this case, there is a higher vertical peak force in case of a smaller wave. When analyzing the quasi-steady wave forces just after the initial peak force, the d60h35 case gives the highest forces. Since the water is already at the deck at the initial phase this cannot accelerate a lot before it hits the bridge deck. In the d60h30 case, the deck is pushed against the ground immediately after the seawall, this explains the low vertical forcing.

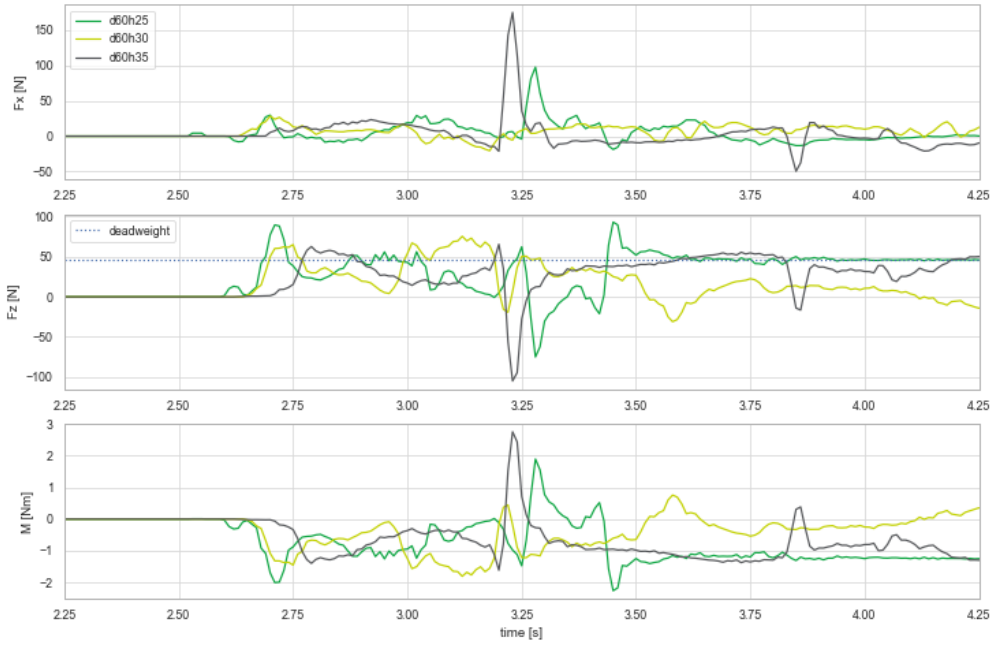

Figure 5.16. Forces on moving bridge deck for several wave cases including a seawall.

5.4.2. Movement of bridge deck

It is clearly visible in Figures 5.17, E.6 and E.7 that in all the cases the deck makes a vertical uplift before the deck moves horizontally along with the flow. Even with the smallest wave, the d60h25 case, the deck makes the largest vertical movement. This can all be explained from the forces which are displayed in the figures above.

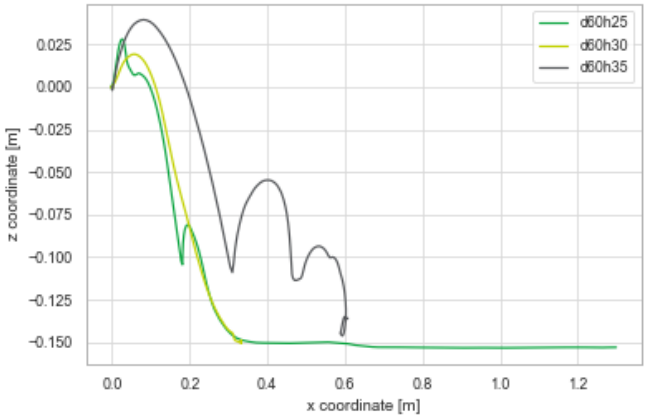

Figure 5.17. Movement of deck with different water levels in the basin with seawall.

Concluded can be that the seawall has an enormous effect on the forces on the bridge deck. Especially the vertical forces become significantly higher even in cases in which the bridge is barely affected by the wave when there was not a seawall.

The bridge moves upward after the initial hitting of the wave.

5.5. Analysis of the effect of an inclined bridge deck

For the purpose of this research, the deck has been inclined in two directions. A positive inclination means the landside of the deck is lifted by an amount that the total inclination is ten degrees. Negative inclination means the seaside of the deck is lifted till the point the inclination is 10 degrees. To gain an accurate conclusion the forces on the decks are plotted for two cases, the d60h30 wavefront case and the d60h35 surging wave case.

From Figure 5.18 follows that in the d60h35 case after the wave hits the negatively inclined bridge deck, the pressure distribution of the wave cannot proceed its natural direction. Above the bridge, an air bubble occurs which has no pressure. underneath the bridge locally a high-pressure field occurs which results in a high vertical force. In Figure 5.19 the pressure distribution with a positive inclination is given. The water extraction at the top of the deck is not as clear as in the case with negative inclination at the underside of the bridge deck, water particles still want to move upwards which results in a high-pressure field below the deck. This phenomenon is less severe than when the deck is flat or negative inclined. So the vertical forces are not as large.

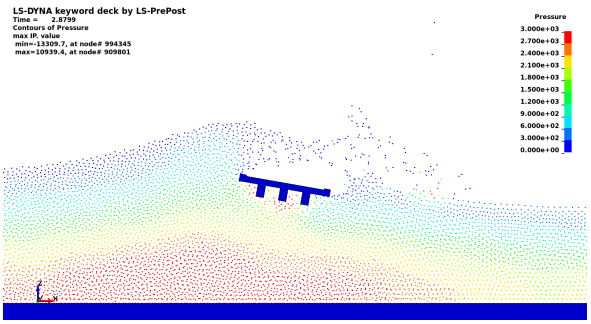

Figure 5.18. Negative inclination pressure after impact d60h35.

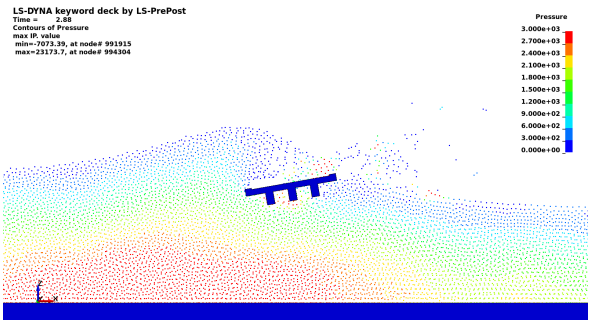

Figure 5.19. Positive inclination pressure after impact d60h35.

In Figure 5.20 and 5.21 it is clearly visualized that the initial vertical peak force is a lot higher when the bridge is negatively inclined (these forces are extracted from a constraint deck, so no movement of the deck is induced by the forces). In the case of positive inclination, the underside of the bridge deck is more exposed to the incoming wave which results in these high vertical forces. This can also be seen from Figure 5.18. Though

from a positive inclined deck can be stated that the downward force due to the following flow behind the wave. The horizontal forcing is not dependent on the inclination of the bridge deck.

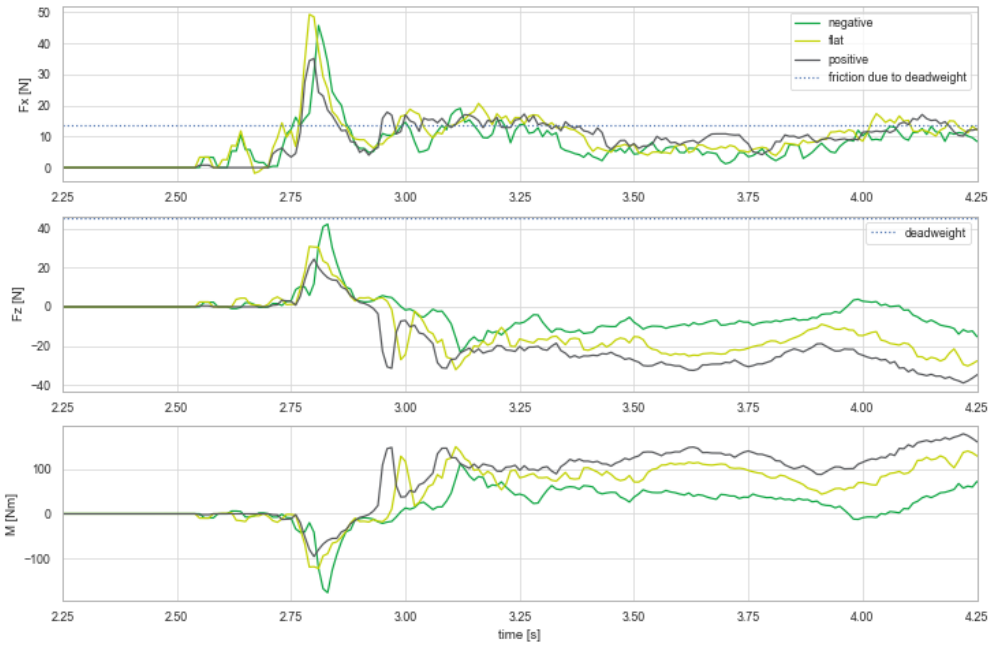

Figure 5.20. Forces on moving bridge deck for d60h30 case.

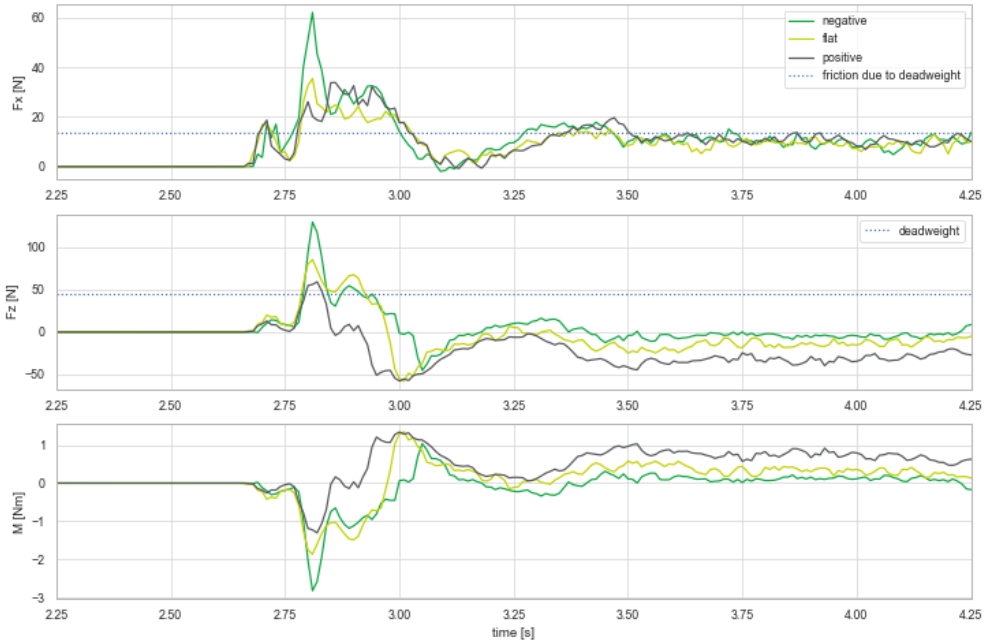

Figure 5.21. Forces on moving bridge deck for d60h35 case.

6

Possible solutions regarding the failure mechanism

In this chapter, some measures against failing of the bridge deck will be studied and new solutions will be introduced.

From the outcomes of the previous chapters can be concluded that not a single normative force can be determined. Different phases of the wave result in different forces in different directions. Though, some measures can be suggested in which the horizontal forces can be mitigated and transferred to vertical preferably downward forces, so the superstructure stays in place.

The simulations in which the countermeasures are tested are executed for two wave cases, one is the d60h30 case in which a breaking wave results in high horizontal forcing. The other case that is simulated is the d60h35 case in which the wave results in high vertical forces. Because of these varying force mechanisms, it is interesting to analyze both of these wave cases so the countermeasures are tested for both horizontal and vertical failure modes.

Different perspectives can be applied in preventing bridge deck failure. The first perspective is to mitigate the forces on the bridge deck, by changing the shape of the bridge so no large surface area is exposed to the wave forcing. The second perspective is to mitigate the peak force which accounts for the highest forces. A damper can be used to disperse this peak force over a longer amount of time. This way the shear keys or bridge abutments do not have to be designed for these very large impact forces. Another option is to construct a sacrificial beam which can be mounted on the bridge piers, when this is applied the horizontal forces will be transferred to the pier by the sacrificial beam and the bridge deck is relieved.

6.1. From conclusions of the hydrodynamics to a solution

From Chapter 5 follows that a shear key is a good solution for incoming wave bores. Though the forces on the shear key will become too large and mitigations have to be found for this. Geometries of the bridge deck will be changed and the effect this has on the forcing on the deck will be discussed. Another countermeasure could be a sacrificial beam, that can relieve the forcing on the bridge deck.

Another clear statement is that in the case of surging waves with a short wavelength the vertical force is the dominant forcing. Changes in geometry of the deck will probably not have much effect since the forces originate from confined water particles. Connections between the pier and the deck need to be made stronger and dampers could mitigate the highest impact forces.

6.2. Analysis of the effect of different geometries

The impact force on the bridge is for a great deal determined by the frontal area of the bridge deck. In order to see what effect the shape of the deck can have on the forcing on the bridge, different shapes in front of the bridge are formed to see the effect on the forcing. To compare the results of this thesis to the research of a

steady flow the same shapes have been taken as in the research of [Naderi, 2018]. It is also chosen to take a hollow box girder layout of the deck as a comparison in these tests. The forces are extracted from a model in which the bridge deck is constraint so the own weight of the deck is of no importance in this simulation. The frontal area of the deck is 30mm. The sizes of the wings are determined by this dimension. A schematic display of the deck is displayed in Figure 6.1 and Table 6.1.

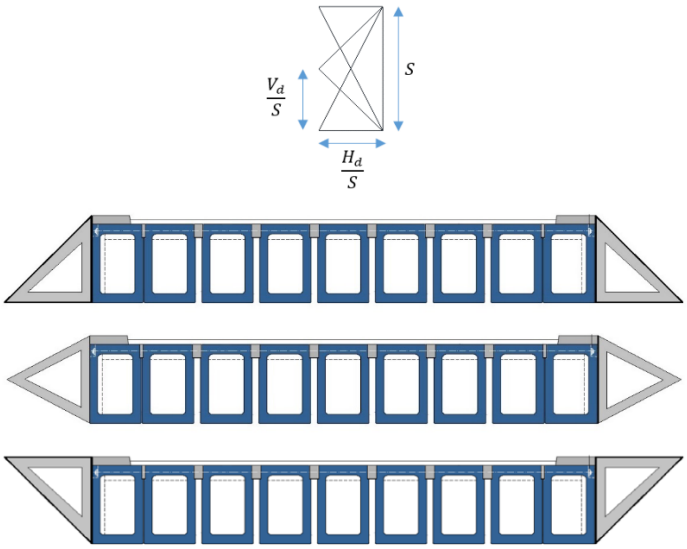

Figure 6.1. Schematic shape of the deck using wings for mitigating flood effect [Naderi, 2018].

Table 6.1. Dimensions on the side of the deck as countermeasure.

	scenario 0	scenario 1	scenario 2	scenario 3	scenario 4	scenario 5	scenario 6
Vd/S	0	1	0.5	0	1	0.5	0
Hd/S	0	0.5	0.5	0.5	1	1	1

Simulations are done for the d60h35 and the d60h30 case. Together with the research of [Naderi, 2018] comparisons can be made between steady flow, surging wave and propagating wavefront. The results for the surging wave case, d60h35, gave undesirable results. The differences between the various scenarios could not be observed. The reason for this could be the geometry of the underside of the deck. Instead of big girders, the underside is just a flat surface which lowers the horizontal forces.
The shape of the wave also has an effect on this force, since the wave is almost surging the water level rises quite gradually at the location of the bridge. Not a large impact is occurring at the front side of the bridge.

6.2.1. Propagating wave front

In the case of a propagating wavefront, it can be concluded that there is a difference in the forcing due to the different geometries of the deck. From Figure 6.2 can be concluded that scenario 5 is the scenario with the lowest horizontal force on the bridge deck (forces are extract from a model in which the movement of the deck is constraint). Scenario 6 has a very low horizontal force on the bridge deck. Though in a later stage a large vertical force is present, see Figure 6.2. This can be explained by the fact that the total horizontal surface area on the bottom of the bridge deck is larger compared to the other cases.

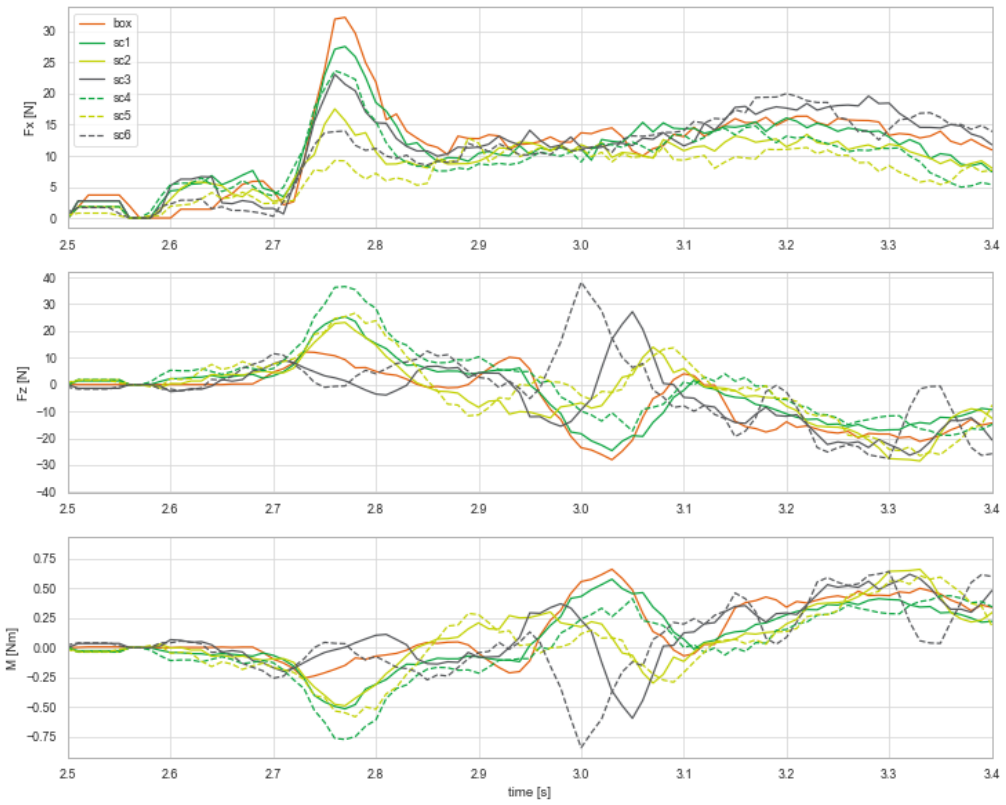

Figure 6.2. Forces on different constraint deck forms for the d60h30 wave case.

[Naderi, 2018] found out that in steady flow a bridge deck like scenario 6 has the largest resulting drag coefficient. From this research follows that this geometry results in the lowest vertical forces from a propagating surge but that it does not affect the forcing by a surging wave with a small wavelength.

6.3. Forces on shear keys

From section 4.7 follows that the forces obtained from the numerical simulations on a lab scale can be scaled by factors based on the Froude scaling. The total normative forces in the two different cases d60h30 and d60h35 can be determined.

The forcing on the bridge starts with a large peak force, if this peak force can be damped, the peak force can be dispersed into a smaller force over a larger time. This way the shear key does not have to be designed on the peak forces.

6.3.1. Design resistance of a shear key

The forces on the bridge in this researched are al calculated for a test on a 1:37 scale. It is shown that these forces can be reasonably accurately scaled to full-scale. The design of shear keys should be based on these full-scale models.

The d60h30 case has a maximum horizontal force of 67.16 N. When the forcing scale factor of 1369 is applied the total force on a 9.4m deck can be determined, namely 864kN.

The total friction force which follows from a friction factor of 0.29 in the lab tests, from literature follows a

friction factor between 0.2 and 0.33. When assuming a friction factor of 0.29 and the total horizontal friction force in case no vertical loads are applied on the bridge are 184kN. This is not enough to withhold the deck from sliding.

The total horizontal capacity that has to be transferred to the bridge by shear keys, if only shear keys are applied, is 864kN. With three girders six shear keys can be placed which results in a required horizontal capacity of 144kN per shear key for the d60h30 case.

In the case of the surging wave type in case d60h35, the normative forces from the hydrodynamics are the vertical forces on the bridge deck. It is hard to change the geometry of the deck in such a way that the vertical forces are mitigated. This can be done for waves with short wavelengths, though since surging tsunami waves have often very long wavelengths this will not be studied in this thesis.

6.3.2. Viscous dampers

In the seismic design of bridges, often viscous dampers are applied to transfer the loads to the piers. The main advantage of these dampers is that they can disperse high peak loads over a larger timespan which results in lower maximum forces at the substructure.

Another advantage is that these dampers can be attached to the slab of the bridge deck. This has the advantage that no large transverse loads exist on the girders which could lead to shear failure of the girders.

Large forces on the pier have to be avoided since this force has to be distributed to the foundation. The horizontal forces will result in high moments at the foundation. Therefore, isolation of the forces is needed between the bridge deck and the piers. There already is some isolation because of the rubber bearings. This ductility in the system can be upgraded by the viscous dampers.

6.3.3. Sacrificial beam

In this section, a sacrificial beam is placed in front of the bridge itself. The beam has the same shape which resulted in the least horizontal forcing from the analysis of different geometries. The beam has to be supported by the pier so the forces on the beam will not be passed to the deck but directly to the pier.

In Figure 6.4 the forces of the situation without sacrificial beam are given and the forces on the separate beam and deck parts of the situation including the sacrificial beam. The bridge deck did not fail in this simulation. From Figure 6.4 follows that the large peak force which is present in the case without a beam in front of the bridge is not present in the case with the beam. In this case with sacrificial beam, the deck has some movement but does not fail. The high peak load followed from the incoming bore is mitigated by the shape of sacrificial beam, the horizontal movement of the water is then pointed over and underneath the bridge deck instead of against it, which decreases the horizontal impact by a great amount. Concluded from this can be that the sacrificial beam is a functional measure against bridge deck failure.

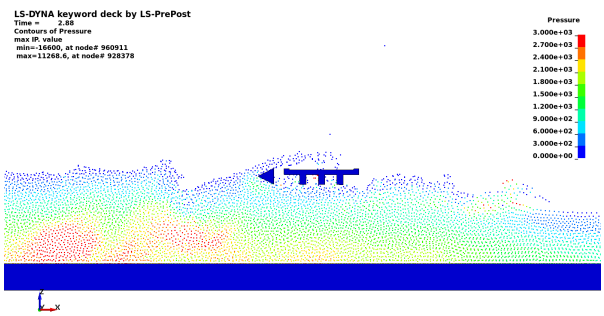

Figure 6.3. Pressure field of d60h30 case around bridge deck with sacrificial beam.

Figure 6.4. Forces on moving deck with a sacrificial beam for d60h30 case.

The d60h35 case has large vertical forces as the main reason for failure in the case without the sacrificial beam. These vertical forces are created by a surging wave with a relatively short wavelength. The sacrificial beam is mostly designed against horizontal forces. As can be seen in Figure 6.5 the vertical forces are barely mitigated by this measure which makes the sacrificial impact beam less suited in the use against surging waves.

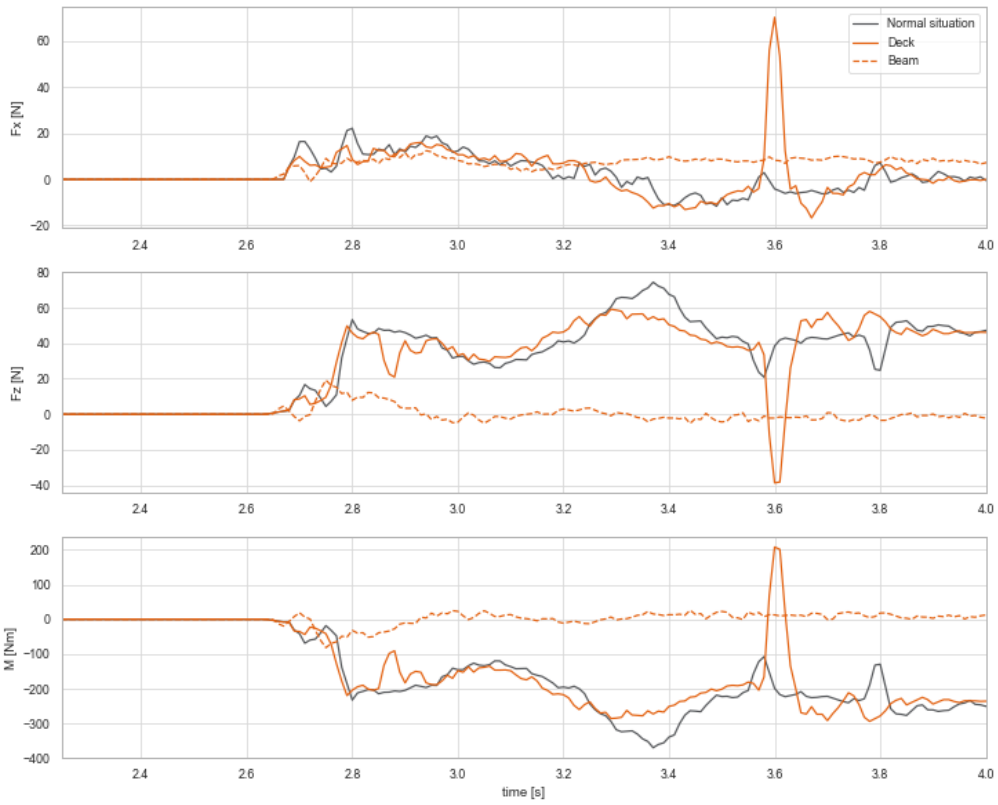

Figure 6.5. Forces on moving deck with a sacrificial beam for d60h35 case.

The d60h30 case results in large horizontal forces on the deck. Expected is that these horizontal forces will be received by the sacrificial beam. The vertical forces which were present in the d60h35 case will still exist and therefore this is not a solution for failure methods that are caused by rotation due to the vertical forces. It should also be mentioned that the shape of the impact beam is unbeneficial in constructing.

6.3.4. Geometry against vertical forcing

In the tests in this research with relatively short wavelengths, a geometry can be thought of which allows the rotational propagating motion of the wave to exist. This measure can only work in case the wavelengths are short. In regions like Otsuchi with wave periods in the order of hours, this measure would not work. Though the upward force cause of this reason should be smaller as well.

6.4. Feasibility of the supposed solutions

In practice, there are some photos of concrete lateral restrainers which are demolished after a flood or tsunami. In some cases, the bridge deck is totally replaced from the pier and in some cases, the bridge is still in place but the shear keys are damaged. Shear keys are often designed with a certain capacity, if the capacity is exceeded harm can be done to the substructure.

In the case of the sacrificial beam, large moments will exist in a horizontal direction by the horizontal forcing. A design needs to be made to withstand this forcing, decided can be at what force it is sacrificed.

What are the forces in the pier and the foundation due to these measures and is it worth it to design on these forces that only occur once in a 30 year when a tsunami occurs?

7

Discussion, conclusion and future research

7.1. Discussion

This section provides a discussion on different levels. First, the methodology is revised. Then the assumptions and limitations of the physical and the numerical model are discussed. Whereafter the proposed countermeasures will be argued. Lastly, this research is mirrored to reference projects and the literature review to investigate the applicability of the study.

7.1.1. Research method

This thesis is part of an interdisciplinary project that studied the reconstruction of Otsuchi in Iwate prefecture. In this thesis the failure mechanisms of bridge decks are analyzed which is part of a wider investigation of bridges struck by tsunamis and severe floods. In preceding studies, CFD and laboratory experiments were used to detect failure modes on bridges due to a steady flow. In this thesis, the numerical SPH simulation approach was used to investigate the effect of waves on the response of a bridge deck.

A possibility to do lab tests at the Waseda University in Tokyo was provided after the DIMI interdisciplinary project in Otsuchi. The physical lab tests were performed in an early stage of the research. With the gained knowledge in this research. In the next section, the execution of the lab tests will be discussed.

A large number of studies have investigated the tsunami induced failure modes of bridge decks which resulted in a wide variety of factors that potentially influence the behavior. Therefore, the parameters used in this study applicable to the SPH model were carefully chosen. Subsequently, further study is done on the influence of the shear-keys, inclination of the bridge deck and the seawall. It turned out that the more challenging modeling aspects of this research were the upscaling from the experimental scale to a realistic scale and performing simulations with a full 3D model.

7.1.2. Physical model

The lab test setup which is used in this research is meant to discover the propagation of tsunamis on shallow slope coasts including bottom roughness. The same setup is used in this research to study bridge superstructure failure since limited time was available to do lab tests. It is very valuable to analyze the properties of the wave and what effect different basin heights and tank heights have on these wave properties. However, this thesis primarily focuses on the effect of these waves on the bridge deck and not on the waves itself.

A dam break underflow test is used to find tsunami-induced failure mechanisms of bridge superstructures. It can be questioned in which way a dam break underflow method simulates a tsunami in a proper manner. The waves created by this dam break underflow have relatively short wavelengths and cannot be compared with a tsunami in a steep slope ria coast area such as the coast near Otsuchi. The propagating wavefront which is created in some cases is comparable to a tsunami in a shallow coast area.

During the lab test some physical model uncertainties were present. Firstly, the gate opening in all the tests should be executed with exactly the same procedure every time. The gate opened with the use of a concrete block in a steel frame attached via pulleys to the gate. The location of the steel frame was varying a little which

resulted in different distances of the rope between the concrete block to the gate door. When analyzing the movies of the tests in a later stage of the research it was unclear if the gate opened consequently with the same opening size. Secondly, water was leaking from the tank. Which resulted in inaccuracies of the water level. This leakage made it hard to keep the water height on the correct level and execute the tests exactly in the moments that the water levels were what they should be in both the tank and the basin. Thirdly, the wave height is determined by wave gauges using electric conductivity. If any air bubbles are present, the measurements are not 100% accurate. The total amount of water in the column is displayed as the water height. This means the water levels in the case of a breaking wave are not completely accurate as well.

Another uncertain factor is the bridge itself. Some individual tests were performed five times to see if the outcomes were constant. The bridge movement is never exactly the same since the deck-pier friction is dependent on the exact location of the bridge and the amount of moist between the different components. Also, the way a bore propagates is never exactly the same so the orientation of the wave relative to the deck is of great importance when analyzing these bridge forces and movements.

The bridge-deck in this research is placed on two bridge piers. Next to the bridge deck, there is still room for the fluid to flow, which in reality could never occur. The 3D effects are dependent on the amount of confinement of water between the bridge piers, the bottom and the deck. In reality, the confinement is dependent on the relationship between the flow area and the obstructed area by the piers. In the lab test this relationship is not fully accurate since the flume is smaller than two bridge segments. Also, no deck section is placed towards the walls of the wave flume, which has an influence on the 3D flows of the fluid.

The movement of the decks from the lab tests is extracted from the movies which where made with a high definition Nikon D5200 camera. In a later stage the videos are processed with the software 'Tracker, a video analysis and modeling tool'. Distances are determined with the help of scaling to a known distance in the movies.

7.1.3. Numerical model

The decision for LS-Dyna instead of Dualsphysics is based on the capabilities of the 2D fluid - rigid body interaction in both models. Run times for the models which are discussed in Appendix C were approximately the same. The rigid-body behavior in Dualsphysics was dependent on the particle size and the gap between particles with different properties. LS-Dyna was easier to work with and at the moment the decision had to be made in which model to continue with, LS-Dyna gave better results for the movement of the bridge deck. The author of this research was aware that both models could lead to a sufficient model that could lead to a good simulation of the lab tests. The capabilities of Dualsphysics to accelerate runtimes with the help of GPU could be a lot more convenient for larger models, the parallel running capabilities could have saved a lot of time.

The used hydrodynamic model is set up from scratch for this particular research. The exact measurements of the flume that is used in the lab tests are also used in the numerical simulations. This made it very convenient to validate the model.

The final particle size that is used in this research for all the 2D models is 5mm, which is relatively large in comparison to the 30 mm thick bridge deck. For the purpose of this research a 5mm particle size was proven to be sufficient. When applying smaller particle sizes, the accuracy of the simulations will increase. But the computational time will increase as well.

7.1.4. Interpretation of the simulation results

Numerical models always represent a simplification of reality. This is also the case for the bridge failure in the SPH model in this thesis. Consequently, it is important to interpret the model results qualitatively: the model is an excellent tool to determine the overall response of a bridge superstructure to a wave, but the exact predicted forcing and movement of the deck could still deviate from reality. Physical tests that were performed several times with the same circumstances have a deviation in results as well. From this fact have to be concluded that exact movement of the deck cannot yet be determined. Regardless of this, a lot of knowledge can be gained about the processes that take place in the case of movement of the bridge deck.

At a certain point in this research two main cases have been chosen to compare the shear-keys, inclination and seawall. These two main cases were the d60h30 case in which the wave broke a significant distance before the wave reaches the bridge structure, hereafter a propagating wavefront is created. The other case, the

d60h35 case, broke just before the bridge deck. The particles in this case still have their circular motion which plays an important role in creating the vertical forces. These differences turned out to be essential for the response of the bridge deck. Another important aspect is the difference of the initial water level which makes the hydrostatic pressures already different at wave impact. As described in previous research, inundation level plays an important role in failure methods of bridge decks. As mentioned before, the surging wave in this thesis cannot be compared to a real tsunami. However, the wave could represents a case in which a high tide is combined with an extreme storm surge. In this research a single wave is observed, on the contrary, in a storm surge series of waves will affect the bridge deck.

7.1.5. Feasibility of proposed countermeasures

The proposed counter measures in this research, the change of geometry of the deck and the aerodynamic impact beam. A main distinction is made between a propagating wavefront, which results in dominant horizontal forces and a surging wave which results in dominant vertical forcing. The propagating wavefront forces could be distributed by the shear keys. Other options to mitigate these forces is changing the geometry of the deck. When constructing a triangular structure which has one point aiming at the seaside the wave forcing is mitigated the most.

This shape is also used to construct a sacrificial beam. When this beam is constructed in front of the bridge deck, no shear keys are needed in the normative case for the propagating wave in front of this research to hold the deck in place. In the case of the surging wave, the sacrificial beam and the different geometry of the deck does not have much effect. The shape of the wave changes a bit but the circular motion of the particles that create the vertical force is not disturbed since these particles come from below.

7.1.6. Comparison with theory and reference projects

Wave forcing on the bridge deck can be calculated in an analytical manner in several ways defined by various literature. The scatter between these calculations was enormous and the outcome of the SPH model was not very close to any of these analytical outcomes. The model is validated by the movement of the deck and the movement of the bridge deck in the model matched the movement of the bridge deck in the lab tests in critical points.

When linking the main statements from this thesis to the case study of Utatsu, some statements can be supported. It has to be noted that the tsunami that interacted with the Utatsu bridge was a surging wave with a very long wave length. This scenario is not tested in this research. In the Utatsu case multiple factors played a role in the bridge failure and differed along the bridge length; seawall, inclination and shear-keys where three of them. For the deck before a seawall and with water depth below it (segment S10 from Figure 1.1) the shear-keys were still intact, the statement which is made that the bridge does not travel far if a rotation is made by the deck is supported. Segments over a larger water depth before a seawall (Segments 8 + 9) with a large width traveled far, which is supported by the statement that a seawall close to the bridge deck results in a large upward force and thus longer distance traveled and a larger chance of rotation as well as the statement that inclination leads to higher vertical forces on the deck. segments with less water underneath the decks, but with the seawall in front of the bridge (S3 to S7) were not rotated. The water level underneath the bridge is less than underneath S8 to S10 so this resulted in less vertical thus rotational forces. But did lead to high horizontal forces which results in the sliding failure mode.

It is important to state that the incoming tsunami was a surging wave with a long wavelength, which is not 1 to 1 comparable to the waves analyzed in this thesis.

7.1.7. Relation to the Otsuchi area

The main conclusion from this research is dependent on the case if the wave is broken or not. The difference between these two cases is substantial. Where a propagating wavefront result in dominant horizontal force, a surging wave (with a short wavelength) results in dominant vertical force. Countermeasures are treated in Chapter 6 with respect to the propagating bore, whereas it is harder to design countermeasures against the dominant vertical forces. To answer the question in which coastal regions these countermeasures can be effective is a study on its own. Hence, these measures would not be effective in all tsunami-prone areas. It is valuable to have knowledge about the location where the wave is breaking. The steep and ria type of coast at Otsuchi results in a surging wave with very long wavelengths. On the other hand, a shallow coast like the Sendai plane results in propagating wavefronts.

The surging waves treated in this research have a small wavelength, when comparing this to the Tohoku tsunami of 2011 this has completely different effects on the bridge structure. Waves with wavelengths in the order of the 2011 Tohoku tsunami near Otsuchi could best be simulated as steady flows or flows with slow acceleration.

7.2. Conclusions

In this section, the answer is given to the main question of this research: 'Looking for tsunami-induced failure mechanisms of bridge deck using SPH modeling'. This question is divided into several sub-questions stated in Chapter 1. In this section, each sub-question is treated separately.

What are the failure modes of a bridge deck with different tsunami wave impacts and what is the effect of shear keys, inclination or seawalls?

In line with the expectations, the bridge has two dominant failure modes that can be observed. The bridge deck can slide off its piers or it can rotate of its piers. In this research, it has been found that the waveform is of great influence on the different failure modes. In the case of a surging wave the fluid particles have a rotating movement and from this rotation not only horizontal but also very strong vertical forces will cause the bridge to uplift. Since the wavelengths in this research were relatively short, the vertical acceleration at the seaside of the bridge started earlier than the land side which results in a rotating movement of the deck. A propagating wave, on the other hand, result in very high horizontal impact forces, even when wave heights are lower than surging wave cases, the horizontal force is higher. This results in sliding of the bridge deck and not in a rotation.

Different water levels in the tank, a larger water level in the tank results in a faster wave and from this follows larger vertical and horizontal forcing. Also the phase of the wave is slightly dependent on the initial water level in the tank. The increased length and wave speed did not automatically mean that the bridge traveled a greater distance. The distance it travels seems random, although it seems like the angle of the deck with respect to the horizon determines in which direction the bridge accelerates.

Different water levels in the basin, when the water levels in the basin differed, the phases of the waves vary greatly at the location of the bridge. The location at which the wave brakes played a big role in the forcing that act on the bridge superstructure. A wave that breaks before the bridge and propagates as a wavefront result in a high horizontal impact force on the bridge. Therefore, in this case, sliding is the main failure mechanism. When the wave is still surging, and the fluid still has its clear circular motion, the wave results in dominant vertical forcing which results in uplift of the bridge deck. In combination with the horizontal forcing, this results in a rotating failure mode of the bridge deck.

Shear keys, rigid shear keys perform well against the horizontal forces which are created by the propagating wavefronts. The vertical forces in the case with a propagating wavefront are relatively low so the dead-load of the bridge itself withstand this uplifting force.

In the case of a surging wave, the vertical wave forces are dominant in the failure mode. The shear keys are able to resist the horizontal forcing but not the vertical motion which initiates rotation. The rotation of the bridge deck in this case is larger since the point of rotation is fixed. In this case, the horizontal force is not translated to acceleration, so the bridge undergoes a smaller displacement.

Inclination, in case of a propagating wavefront the inclination of the bridge deck does not significantly affect the horizontal forcing. In the case of a surging wave, it is remarkable that in the case of the positively inclined deck not a significant peak force is observed.

The inclination of the bridge deck does significantly influence the vertical force on the bridge deck. When the deck is negatively inclined, the vertical impact forces on the deck are increased substantial. When the deck is positively inclined the vertical forces are less than the case where no inclination is present. This applies for both the surging as the propagating wavefront situation.

Seawall, when a seawall is located straight behind the bridge. This results in confinement of the water which results in a high vertical force on the bridge deck. The vertical force causes the bridge to lift and rotate, yet, the downward supercritical flow behind the seawall results in a sudden movement of the bridge deck to the ground where it stays at its place.

Is smoothed particle hydrodynamics (SPH) a good way for analyzing tsunami-induced failure of bridges?

The final 2D SPH models with a particle size of 5mm and acceptable runtimes, which are discussed in Chapter 5, give a good resemblance of the executed lab tests at Waseda University. The forces were not measured in the lab tests but the movement of the deck gave matching results and the qualitative conclusions which followed from the lab tests and the SPH model were similar.

Can 2D SPH models simulate 3D effects accurately?

Since the waves from this research all had high impact forces, the threshold of motion could be simulated by a 2D model in a proper way since the impact force is not dependent on the 3D effects. What happens after wave impact is different in 2D and 3D models. A 3D model can resemble the movement of the deck in a more accurate manner. The qualitative conclusions as given in this section are based on a 2D model model approach and give satisfying results.

When analyzing single wave forces of a known wave on a single structure, where not many different simulations are needed, 3D models with a small particle size would be advised since this increases the ultimate accuracy of the model.

Based on the results of the SPH model, what kind of countermeasures can be proposed to counteract the failure mechanism of a bridge deck due to tsunami waves?

Two countermeasures are proposed,a sacrificial beam that can withstand the horizontal peak forces, but does not work against the vertical forces of a surging wave. The other countermeasure is the change of geometry of the bridge deck. When a triangular shape is used the horizontal forces are mitigated by a great amount.

Finally the main research topic will be treated.

Looking for tsunami-induced failure mechanisms of bridge deck using SPH modeling

One of the goals of this research is to create a forensic tool that could determine the failure mode of a bridge deck by only knowing its final location and position. From this thesis follows that a deck could rotate before reaching the ground in case shear keys are present. When a surging wave is present and the deck gets lifted of the pier, the deck still reaches the bottom in the same orientation as it started. once on the ground the deck rotates due to the steady flow created behind the incoming wave. The force of this flow is strongly dependent on initial water level on the bottom, and the water level difference between basin and tank.

7.3. Recommendations for further research

7.3.1. Physical model

The setup of a different research to the effect of waves on overtopping of structures is used as starting point for the setup of this research. The modeling of the rough bed was something that cannot be done in an easy manner in the SPH model. Also the bridge deck is located far from the top of the slope. The wave characteristics change along the path of the false bottom. To create surging waves at the location of the bridge deck the bridge deck could be placed closer to the top of the slope. In practice, in a steep coast area, it is often not possible te relocate bridges to inland locations.

7.3.2. Numerical model

The SPH model that has been used to obtain the results of this research regarding the forces and movement of a bridge superstructure is useful for qualitative analysis of the relative response of the different wave characteristics and measures which are investigated. The model is an excellent tool to provide the answers to the research questions. No absolute values can be extracted with the purpose of designing such structures.

In this research, it is chosen to run the final models using the software of LS-Dyna. This has the capability of solving on 32 cores at the same time. DualSPHysics is able to use GPU computing which could run SPH models in a more efficient manner with lots of parallel processes.

In SPH modeling it is difficult to implement local refinement of particles. This could be an interesting function. For this setup the forming of the wave could be calculated with a relative course particle size and the interaction between fluid and structure could be calculated with small particle sizes. An other option could be to split the model in half, the forming of the wave which you can calculate once. Save this and create a dy-

namic boundary from which the saved wave can flow in. This way the wave does not have to be recalculated every run.

Validation of the SPH model is now done based on the bridge deck movement. Literature that was found was not sufficient to calculate the forces on the deck in an analytical manner. Recommended will be the use of a load cell in the physical tests to measure the forces when this kind of research will be executed.

As an answer to the subquestion, concluded can be that the 2D model represents waves with high impact forces in a proper manner since the wave is still an 2D phenomenon at the moment of impact. When analyzing failure caused by flows these 3D effects are more dominant and 3D models would be suggested.

The commercial potential of SPH models is certainly present, though the runtimes are long compared to already integrated CFD models. In some cases like in this thesis, it is profitable to use a particle model, since the bridge deck movement can be computed without remeshing.

A relatively new technique in CFD modeling is over-set mesh. This means that a structure can have a mesh that moves over a set mesh. In this case no computational remeshing in every time-step has to be done, which means this could also be a good model for the purpose of this thesis.

7.3.3. Bridge deck failure

This research is limited on a three-girder-slab bridge deck with a span of 9.4 meters. Deviations can already occur when more girders are used or a longer span is applied. The geometry of the bridge is an important aspect which is also shown in Chapter 6. Factors that are treated in the literature review of this research but not studied with the SPH model are: different bridge types, entrapped air pockets, distance to the top of the slope, submergence of the bridge deck, distance to channel floor, debris effects. All these factors can be studied in further research.

Especially the wave phases are important for the dominant wave forcing. The wave breaks on the flatbed in the model. The bridge could also be relocated towards the top of the slope. When the slope is removed completely and the opening of the gate is also taken as a variable, the water level difference between the basin and the tank will be larger and therefore, longer (surging) waves can be created which resemble realistic tsunamis in a better way.

The research of the effect of nearshore topographies on tsunamis are important in determining what properties a wave has when it arrives at the shore. When this is known, specific countermeasures per area can be designed on the wave characteristics.

Waves could be classified by Froude number in case the waves are in a similar wave phase, velocity could be stated as the wave front velocity.

It is assumed that shear keys could be constructed that can handle the forces on the bridge deck. For seismic purposes, shear keys are designed in such a way that the shear keys fail before the forces on the deck get too high which will save the bridge pier. When these measures are planned to be applied, a complete analysis of forces has to be made including internal pier and foundation force schemes. Subsequently, concrete-reinforcement designs can be made.

From the lab tests and numerical runs follows that apart from the failure mode on the deck, a deck is likely to rotate after it is failed and located on the bottom. When it slides off the piers and is located on the bottom with the deck-side up. The resulting flow behind the wave together with the bottom friction results in a moment force that flips the deck in almost every case.

The 2D models are representing cases well when the initial impact of the wave plays a great deal in the failure of the superstructure. When the flow which occurs after the wavefront is causing the failure, 3D effects play a bigger role in the failure mechanism. Concluded has to be that these cases are not simulated in an accurate manner by an 2D SPH model. When computational times become even lower after the development of HPC and GPU. This research could be redone with only 3D models.

In this research only one 3D model is displayed, which had a incoming propagating bore. This model gave significantly more accurate results than the 2D model. Future research should look into the accuracy of the 3D model for surging waves as well.

7.3.4. Countermeasures against wave impact

The sacrificial impact beam is functional in mitigating the horizontal impact force in case of incoming wave fronts. To design this beam in concrete the geometry is really impractical. The beam does not have to bear any vertical loads and the choice for material can be investigated in further research.

Dampers that can be used to mitigate the impact forces have to be mounted to the structural elements. The forces have to be translated over the whole structure so it makes a difference if these dampers are fixed to the girder or the pressure zone in the bridge. This can be researched.

Bibliography

Azadbakht, M. and Yim, S. C. (2014). Simulation and Estimation of Tsunami Loads on Bridge Superstructures. *Journal of Waterway, Port, Coastal, and Ocean Engineering*, 141(2):04014 031.

Bea, R., Xu, T., Stear, J. and Ramos, R. (1999). Wave forces on decks of offshore platforms. *journal of waterway, port, coastal and ocean engineering*, 125(June):136–144.

Bi, K. and Hao, H. (2015). Modelling of shear keys in bridge structures under seismic loads. *Soil Dynamics and Earthquake Engineering*.

Bricker, J. D. and Nakayama, A. (2014). Contribution of Trapped Air, Deck Superelevation, and Nearby Structures to Bridge Deck Failure during a Tsunami. *Journal of Hydraulic Engineering*, 140(5):05014 002. URL http://ascelibrary.org/doi/10.1061/{%}28ASCE{%}29HY.1943-7900.0000855.

Bricker, J. D., Nakayama, A., Takagi, H., Mitsui, J. and Miki, T. (2015). *Mechanisms of damage to coastal structures due to the 2011 Great East Japan Tsunami*. Elsevier Inc. URL http://dx.doi.org/10.1016/B978-0-12-801060-0.00019-8.

Byron, I. (2019). Wave Energy and Wave Changes with Depth. URL https://manoa.hawaii.edu/exploringourfluidearth/physical/waves/wave-energy-and-wave-changes-depth.

Cosmec (). Elastomeric bearings. URL http://www.cosmecinc.com/ElastomericBearings.

Cuomo, G., Tirindelli, M. and Allsop, W. (2007). Wave-in-deck loads on exposed jetties. *Coastal Engineering*, 54(9):657–679.

Domingues, J. M., Crespo, A. J., barreiro Aller, A., Gesteira, M. G., Feal, O. G., Canelas, R. and Altomare, C. (2018). Users Guide for DualSPHysics code. (May):1–146.

Esteban, M., Glasbergen, T., Takabatake, T., Hofland, B., Nishizaki, S., Nishida, Y., Stolle, J., Nistor, I., Bricker, J., Takagi, H. and Shibayama, T. (2017). Overtopping of Coastal Structures by Tsunami Waves. *Geosciences*, 7(4):121. URL http://www.mdpi.com/2076-3263/7/4/121.

Gingold, R. A. and Monaghan, J. J. (1977). Smoothed particle hydrodynamics: theory and application to non-spherical stars. Technical report.

Hallquist, J. O. (2006). LS-Dyna theory manual. Technical Report March.

Hamakareem, M. I. (). Bridge Bearings -Types of Bearings for Bridge Structures and Details. URL https://theconstructor.org/structures/bridge-bearings-types-details/18062/.

Hiraki, Y., Shoji, G., Fujima, K. and Shigihara, Y. (2011). Evaluation of tsunami fluid force acting on a bridge deck subjected to breaker bores. *Procedia Engineering*, 14:1079–1088.

Hobbs, D. (). Computational Astrophysics.

Hofste, G. (2012). *Stevin Outlet Sluices wave impact under a beam*. Ph.D. thesis.

Istrati, D., Buckle, I. G., Itani, A., Lomonaco, P. and Yim, S. (2017). Large-Scale Fsi Experiments on Tsunami-Induced Forces in Bridges. *16th World Conference on Earthquake, 16WCEE*, (Paper N° 2579).

Kallaka, T. and Wang, C.-j. (2011). Efficient Numerical Model for Studying Bridge Pier Collapse in Floods. 5(12):710–715.

Kawashima, K. (2012). damage of bridges due to the 2011 great east Japan earthquake. 12(4):319–338.

Kawashima, K. and Matsuzaki, H. (2012). Damage of Road Bridges by 2011 Great East Japan (Tohoku) Earthquake. *15th World Conference on Earthquake Engineering (15WCEE)*, 2.

Kerenyi, K., Sofu, T. and Guo, J. (2009). Hydrodynamic Forces on Inundated Bridge Decks. *Report No. FHWA-HRT-09-028*, (May):48. URL http://www.fhwa.dot.gov/publications/research/infrastructure/hydraulics/09028/.

Kjeldsen, S. and Myrhaug, D. (1979). Breaking Waves in Deep Water and Resulting Wave Forces.

Liu, G. and Liu, M. (2003). Smoothed particle hydrodynamics, a meshfree particle method.

Lomonaco, P., Istrati, D., Buckle, I. G., Yim, S. C., Maddux, T., Buckle, I., Yim, S. and Xiang, T. (2016). Large scale testing of tsunami impact forces on bridges. URL https://www.researchgate.net/publication/303699917.

LSTC (2019a). Contact modeling in LS-DYNA. URL https://www.dynasupport.com/tutorial/ls-dyna-users-guide/contact-modeling-in-ls-dyna.

LSTC (2019b). contact parameters. URL https://www.dynasupport.com/tutorial/contact-modeling-in-ls-dyna/contact-parameters.

Lucy, L. B. (1977). Numerical approach to testing of fission hypothesis. 82(12):1013–1024.

Mainichi (2018). Ship smashes into Kansai airport bridge as typhoon hits Japan. URL https://mainichi.jp/english/articles/20180904/p2g/00m/0dm/065000c.

Maruyama, K., Hosoda, A., Tanaka, Y., Kosa, K., Arikawa, T. and Mizutani, N. (2017). Tsunami force acting on bridge girders. (January).

Mase, H., Kimura, Y., Yamakawa, Y., Yasuda, T., Mori, N. and Cox, D. (2013). Were coastal defensive structures completely broken by an unexpectedly large tsunami? A field survey.

McConnell, K., Allsop, W. and Cruichshank, I. (2004). Piers, jetties and related structures exposed to waves.

Megally, S. H., Silva, P. F. and Seible, F. (2002). Seismic Response of Sacrificial keys in bridge abutments. Technical Report 59.

Michael Henry, A. (). Wave forces on bridge decks and damping techniques to reduce damages Recommended Citation. Technical report. URL https://digitalcommons.lsu.edu/gradschool{_}theses.

Monaghan, J. J. (1992). Simulating free surface flows with SPH.

Mori, N., Takahashi, T., Yasuda, T. and Yanagisawa, H. (2011). Survey of 2011 Tohoku earthquake tsunami inundation and run-up.

Naderi, N. (2018). *Numerical Simulation of Hydrodynamic Forces on Bridge Decks*. Ph.D. thesis.

NTNU (2014). General Modelling and Scaling Laws used in model testing. (1). URL http://www.ivt.ntnu.no/imt/courses/tmr7/lecture/Scaling{_}Laws.pdf.

Okamoto, T., Fortes, C. J. and Basco, D. R. (2008). Bore propagation speed at the termination of wave breaking. pages 1–14.

Oudenbroek, K. (2018). *Experimental research on hydrodynamic failure of river bridges on spread footings*. Ph.D. thesis.

Salem, H., Mohssen, S., Kosa, K. and Hosoda, A. (2014). Collapse Analysis of Utatsu Ohashi Bridge Damaged by Tohuku Tsunami using Applied Element Method. *Journal of Advanced Concrete Technology*, 12(10):388–402. URL http://jlc.jst.go.jp/DN/JST.JSTAGE/jact/12.388?lang=en{&}from=CrossRef{&}type=abstract.

max Sheppard, D. and Marin, J. (2009). Final report wave loading on bridge decks. (December).

The Trelleborg Group (2017). Everyday ingenuity fuels progress Trelleborg Engineered Products.

Tokura, S. (2014). Comparison of Particle Methods : SPH and MPS. *13th International LS-DYNA Users Conference*, (1):1–10.

Wu, K., Yang, D. and Wright, N. (2016). A coupled SPH-DEM model for fluid-structure interaction problems with free-surface flow and structural failure.

Yim, S. C. and Azadbakht, M. (2013). Tsunami Forces on Selected California Coastal Bridges. Technical report.

Yreux, E. (2018). Fluid Flow Modeling with SPH in LS-DYNA ®. *15th International LS-Dyna Users conference*.

List of Figures

List of Tables

List of Abbreviations

2D	two dimensional
3D	three dimensional
ALE	arbitrary lagrangian eularian methods
DBC	dynamic boundary condition
DEM	discrete element method
DIMI	Delta's, Infrastructures and mobility initiative
dp	delta particle (particle size)
CFD	computational fluid dynamics
CPU	central processing unit
FEM	finite element method
GPU	graphics processing unit
HPC	high performance computing
ICFD	incompressible computational fluid dynamics
MPP	massively parallel processing
SPH	smoothed particle hydrodynamics
UPD	unseating prevention device
VM	velocity meter
WCSPH	weakly compressible smoothed particle hydrodynamics
WG	wave gauge

A

Overview Waseda test

case	d	h [cm]		WG1		WG6		clean		comments	WG1		WG6		phase key back		WG1		WG6		phase key middle		comment	WG1		WG6		negative inclination		comment	WG1		WG6		positive inclination		comments
				h		h		failure			h		h		failure		h		h		failure			h		h		failure			h		h		failure		
breaking shallow wave wave	50	20	propagating/soni	0.839	0.128	0.868	0.143	none			0.115	0.126	0.143	none			0.119	0.129	0.129	none			0.178	0.129	0.129	none			0.125	0.141	0.150	none					
		25	propagating/soni	0.780	0.143	0.773	0.155	none			0.126	0.143	0.139	none			0.133	0.133	0.133	none			0.157	0.136	0.136	none			0.141	0.138	0.138	none					
		30	propagating/soni	0.715	0.155	0.715	0.167	none			0.143	0.155	0.139	none			0.133	0.133	0.133	none			0.136	0.133	0.133	none			0.133	0.133	0.133	none					
		35	shallow wave waves	0.686	0.155	0.657	0.167	sliding			0.155	0.155	0.139	none			0.139	0.139	0.139	none			0.139	0.139	0.139	none			0.139	0.139	0.139	none					
		35	propagating/soni	0.714	0.178	movement					0.178	0.178	0.163	none			0.081	0.124	0.124	rotational movement			0.078	0.121	0.121	tilt and slide			0.080	0.177	0.122	more 1 step up					
		20	propagating/soni	0.825	0.139	none																															
				0.760	0.143	none																															
				0.946	0.151	none																															
				0.760	0.143	none																															
			propagating/soni	0.752	0.139	sliding				ground turn																											
				0.752	0.137	sliding				ground turn																											
				0.657	0.154	sliding				ground turn																											
				0.760	0.143	sliding				ground turn																											
				0.141	0.151	sliding				ground turn																											
		25	propagating/soni	0.115	0.126	slide/noise				clearly an uplift bocce	0.110	0.134	rotational failure			0.122	0.125	uplift - swap ground rotation rear			0.112	0.126	slide													
breaking shallow wave wave		30	breaking shallow wave wave	0.893	0.142	sliding				ground turn	0.866	0.171	rotational movement			0.178	0.195	none			0.157	0.172	none			0.145	0.127	slide/up/slide			0.142	0.143	tilt slide ground rotate		
				0.869	0.146	uplift - sliding ground rotation										0.127	0.203	none																		
				0.857	0.206	none										0.140	0.197	none																		
				0.857	0.203	none										0.136	0.191	none																		
				0.855	0.197	none										0.122	0.125	uplift - swap ground rotation rear																		
				0.871	0.148	movement - rock																															
				0.869	0.146	uplift - sliding ground rotation																															
				0.855	0.139	uplift - sliding ground rotation																															
				0.863	0.137	uplift - sliding ground rotation																															
				0.145	0.134	uplift - sliding ground rotation																															
	60	20	propagating/soni	0.832	0.187	none																															
				0.855	0.220	rotational movement																															
		25	propagating/soni	0.138	0.134	none																															
				0.127	0.203	none																															
				0.140	0.207	none																															
				0.136	0.191	none																															
				0.122	0.125	uplift - swap ground rotation rear																															
		30	breaking shallow wave wave	0.110	0.134	rotational failure					0.157	0.155	none			0.153	0.169	movement slide			0.154	0.177	step up													
																0.153	0.169	slide																		
																0.153	0.166	slide and rotate																		
																0.155	0.157	slide																		
																0.157	0.155	slide																		
																0.140	0.155	slide																		
		35	breaking shallow wave wave								0.122	0.125	uplift - swap ground rotation rear			0.112	0.126	slide		ground rotate																	
	70	20	propagating/soni	0.839	0.128	0.868	0.143	none			0.115	0.126	0.143	none			0.119	0.129	0.129	none			0.178	0.129	0.129	none			0.125	0.141	0.150	none					
			propagating/soni	0.780	0.173	sliding				ground turn	0.126	0.143	0.139	none			0.133	0.133	0.133	none			0.157	0.136	0.136	none			0.141	0.138	0.138	none					
		25															0.133	0.133	0.133	none			0.136	0.133	0.133	none			0.133	0.133	0.133	none					
																	0.139	0.139	0.139	none			0.139	0.139	0.139	none			0.139	0.139	0.139	none					
																	0.081	0.124	0.124	rotational movement			0.078	0.121	0.121	tilt and slide			0.080	0.177	0.122	more 1 step up					
		30	breaking shallow wave wave	0.893	0.142	sliding				ground turn	0.866	0.171	rotational movement			0.178	0.195	none			0.157	0.172	none			0.145	0.127	slide/up/slide			0.142	0.143	tilt slide ground rotate		
																0.127	0.203	none																		
																0.140	0.207	none																		
																0.136	0.191	none																		
																0.122	0.125	uplift - swap ground rotation rear																		
		35	breaking shallow wave wave	0.141	0.132	slide/noise				clearly an uplift bocce ground turn																												

Figure A.1. Waveheights at WG1 with different particles sizes compared to lab test.

B

K-file LS-Dyna

The LS-Dyna simulations are run with a main file in which all the important parameters are stored. This is called the k-file. The k-file of the d70h30 case is displayed in this appendix.

```
$# LS-DYNA Keyword file created by LS-PrePost(R) V4.5.16 - 23Mar2018
$# Created on Mar-29-2019 (16:45:00)
*KEYWORD
*TITLE
$#                                                                         title
LS-DYNA keyword deck by LS-PrePost
*CONTROL_BULK_VISCOSITY
$Q1 0.001
$Q2 1.0 E-12
$#      q1        q2      type     btype
     0.0011.0000E-12         1         0
*CONTROL_SPH
$#    ncbs     boxid        dt      idim    memory      form     start      maxv
         1         11.00000E20         3      -100        16       0.0      50.0
$#    cont     deriv       ini     ishow     ierod     icont     iavis     isymp
         0         0         2         1         1         1         0        50
$#    ithk
         0
*CONTROL_TERMINATION
$#  endtim    endcyc     dtmin    endeng    endmas     nosol
        5.0         0       0.0       0.0       0.0         0
*CONTROL_TIMESTEP
$#  dtinit    tssfac      isdo    tslimt     dt2ms      lctm     erode     ms1st
        0.0      0.45         0       0.0       0.0         0         0         0
$#  dt2msf   dt2mslc     imscl    unused    unused     rmscl
        0.0         0         0                             0.0
*DATABASE_RCFORC
$#      dt    binary      lcur     ioopt
       0.01         1         0         1
*DATABASE_SPHOUT
$#      dt    binary      lcur     ioopt
       0.1         2         0         1
*DATABASE_BINARY_D3PLOT
$#      dt      lcdt      beam     npltc    psetid
      0.01         0         0         0         0
$#   ioopt
         0
*BOUNDARY_SPH_SYMMETRY_PLANE
$#     vtx       vty       vtz       vhx       vhy       vhz
      -4.5       0.0       0.0       0.0       0.0       0.0
*BOUNDARY_SPH_SYMMETRY_PLANE
$#     vtx       vty       vtz       vhx       vhy       vhz
       0.0       0.0       0.0       0.0       0.0       1.0
*LOAD_BODY_Z
$#    lcid        sf    lciddr        xc        yc        zc       cid
         1       1.0         0       0.0       0.0       0.0         0
*CONTACT_AUTOMATIC_NODES_TO_SURFACE_MPP_ID
$#     cid                                                                 title
         1SPH to GATE
$#  ignore    bucket  lcbucket  ns2track  inititer    parmax    unused    cparm8
         0       200         0         3         2    1.0005                 0
$#    ssid      msid     sstyp     mstyp    sboxid    mboxid       spr       mpr
         1         8         3         3         0         0         0         0
$#      fs        fd        dc        vc       vdc    penchk        bt        dt
       0.0       0.0       0.0       0.0       0.0         0       0.01.00000E20
$#     sfs       sfm       sst       mst      sfst      sfmt       fsf       vsf
       0.0       0.5       0.0       0.0       1.0       1.0       1.0       1.0
$#    soft    sofscl    lcidab    maxpar     sbopt     depth     bsort    frcfrq
         1       0.1         0     1.025       2.0         2         0         1
*CONTACT_AUTOMATIC_NODES_TO_SURFACE_MPP_ID
$#     cid                                                                 title
         2SPH to false bottom
$#  ignore    bucket  lcbucket  ns2track  inititer    parmax    unused    cparm8
         0        50         0         3         2    1.0005                 0
$#    ssid      msid     sstyp     mstyp    sboxid    mboxid       spr       mpr
         1         3         3         3         0         0         1         2
$#      fs        fd        dc        vc       vdc    penchk        bt        dt
       0.5      0.05     -0.01       0.0       0.0         0       0.01.00000E20
$#     sfs       sfm       sst       mst      sfst      sfmt       fsf       vsf
       0.0       0.5       0.0       0.0       1.0       1.0       1.0       1.0
$#    soft    sofscl    lcidab    maxpar     sbopt     depth     bsort    frcfrq
         1       0.1         0     1.025       2.0         2         0         1
*CONTACT_AUTOMATIC_NODES_TO_SURFACE_MPP_ID
```

```
$#     cid                                                              title
         3SPH to Deck
$#  ignore    bucket  lcbucket  ns2track  inititer    parmax    unused    cparm8
         0        50         0         3         2    1.0005                 0
$#    ssid      msid     sstyp     mstyp    sboxid    mboxid       spr       mpr
         1        10         3         3         0         0         0         0
$#      fs        fd        dc        vc       vdc    penchk        bt        dt
       0.0       0.0       0.0       0.0       0.0         0       0.01.00000E20
$#     sfs       sfm       sst       mst      sfst      sfmt       fsf       vsf
       0.0       0.5       0.0       0.0       1.0       1.0       1.0       1.0
$#    soft    sofscl    lcidab    maxpar     sbopt     depth     bsort    frcfrq
         1       0.1         0     1.025       2.0         2         0         1
*CONTACT_AUTOMATIC_SURFACE_TO_SURFACE_ID
$#     cid                                                              title
         4deck to bottom
$#    ssid      msid     sstyp     mstyp    sboxid    mboxid       spr       mpr
        10         3         3         3         0         0         0         0
$#      fs        fd        dc        vc       vdc    penchk        bt        dt
       0.9       0.9       0.0       0.0       0.0         0       0.01.00000E20
$#     sfs       sfm       sst       mst      sfst      sfmt       fsf       vsf
       1.0       1.0       0.0       0.0       1.0       1.0       1.0       1.0
$#    soft    sofscl    lcidab    maxpar     sbopt     depth     bsort    frcfrq
         1       0.1         0     1.025       2.0         2         0         1
*CONTACT_AUTOMATIC_SURFACE_TO_SURFACE_ID
$#     cid                                                              title
         5deck to pier
$#    ssid      msid     sstyp     mstyp    sboxid    mboxid       spr       mpr
        10        11         3         3         0         0         0         0
$#      fs        fd        dc        vc       vdc    penchk        bt        dt
     0.295      0.05       0.0       0.0       0.0         0       0.01.00000E20
$#     sfs       sfm       sst       mst      sfst      sfmt       fsf       vsf
       1.0       1.0       0.0       0.0       1.0       1.0       1.0       1.0
*PART
$#                                                                      title
SphWater
$#     pid     secid       mid     eosid      hgid      grav    adpopt      tmid
         1         1         1         1         0         0         0         0
*SECTION_SPH_TITLE
SPH
$#   secid      cslh      hmin      hmax    sphini     death     start
         1      1.25       1.0       1.0       0.01.00000E20       0.0
*MAT_NULL_TITLE
water
$mu = 0.001
$#     mid        ro        pc        mu     terod     cerod        ym        pr
         1    1000.0  -50000.0      0.01       0.0       0.0       0.0       0.0
*EOS_MURNAGHAN
$#   eosid     gamma        k0        v0
         1       7.0  150000.0       0.0
*PART
$#                                                                      title
falsebottom
$#     pid     secid       mid     eosid      hgid      grav    adpopt      tmid
         3         2         2         0         0         0         0         0
*SECTION_SOLID_TITLE
rigidsolid
$#   secid    elform       aet
         2         1         0
*MAT_RIGID_TITLE
rigid
$#     mid        ro         e        pr         n    couple         m     alias
         2    1000.0       2.0      0.25       0.0       0.0       0.0
$#     cmo      con1      con2
       1.0         7         7
$#lco or a1        a2        a3        v1        v2        v3
       0.0       0.0       0.0       0.0       0.0       0.0
*PART
$#                                                                      title
gate
$#     pid     secid       mid     eosid      hgid      grav    adpopt      tmid
         8         2         2         0         0         0         0         0
*PART
$#                                                                      title
```

```
bridge deck
$#     pid     secid       mid     eosid      hgid      grav    adpopt      tmid
         10         2         3         0         0         0         0         0
*MAT_RIGID_TITLE
rigidmovement
$Q1 0.001
$Q2 1.0 E-12
$#     mid        ro         e        pr         n    couple         m     alias
         3    2350.01.70000E10      0.17       0.0       0.0      0.00
$#     cmo      con1      con2
       1.0         2         6
$#lco or a1        a2        a3        v1        v2        v3
       0.0       0.0       0.0       0.0       0.0       0.0
*PART
$#                                                                         title
bridge pier
$#     pid     secid       mid     eosid      hgid      grav    adpopt      tmid
         11         2         2         0         0         0         0         0
*RIGIDWALL_PLANAR_ID
$#      id                                                                 title
          1
$#    nsid    nsidex     boxid    offset     birth     death     rwksf
          0         0         0       0.0       0.0 0.01.00000E20       1.0
$#      xt        yt        zt        xh        yh        zh      fric      wvel
       8.0       0.0       0.0      -1.0       0.0       0.0       0.0       0.0
*DEFINE_BOX_TITLE
box
$#   boxid       xmn       xmx       ymn       ymx       zmn       zmx
         1      -5.5      7.05      -1.0       1.0      -1.0       3.0
*DEFINE_CURVE_TITLE
Gravity
$#    lcid      sidr       sfa       sfo      offa      offo    dattyp     lcint
         1         0       1.0       1.0       0.0       0.0         0         0
$#               a1                  o1
                0.0                 0.0
               0.05                9.81
             1000.0                9.81
*ELEMENT_SOLID
$#   eid     pid      n1      n2      n3      n4      n5      n6      n7      n8
       7       3    6925    6965    5713    5670    6945    6985    5644    5641
       8       3    6984    6944    6921    6923    7004    6964    6922    6924
       9       3    6926    6966    6965    6925    6946    6986    6985    6945
      10       3    6983    6943    6944    6984    7003    6963    6964    7004
      11       3    6927    6967    6966    6926    6947    6987    6986    6946
      12       3    6982    6942    6943    6983    7002    6962    6963    7003
      13       3    6928    6968    6967    6927    6948    6988    6987    6947
      14       3    6981    6941    6942    6982    7001    6961    6962    7002
      15       3    6929    6969    6968    6928    6949    6989    6988    6948
      16       3    6980    6940    6941    6981    7000    6960    6961    7001
      17       3    6930    6970    6969    6929    6950    6990    6989    6949
      18       3    6979    6939    6940    6980    6999    6959    6960    7000
      19       3    6931    6971    6970    6930    6951    6991    6990    6950
      20       3    6978    6938    6939    6979    6998    6958    6959    6999
      21       3    6932    6972    6971    6931    6952    6992    6991    6951
      22       3    6977    6937    6938    6978    6997    6957    6958    6998
      23       3    6933    6973    6972    6932    6953    6993    6992    6952
      24       3    6976    6936    6937    6977    6996    6956    6957    6997
      25       3    6934    6974    6973    6933    6954    6994    6993    6953
      26       3    6975    6935    6936    6976    6995    6955    6956    6996
      27       3    6935    6975    6974    6934    6955    6995    6994    6954
      33       8    7609    7619    7622    7611    7605    7613    7616    7608
      34       8    7612    7624    7621    7610    7607    7618    7615    7606
      35       8    7619    7620    7623    7622    7613    7614    7617    7616
      36       8    7624    7623    7620    7621    7618    7617    7614    7615
      91       3  218093  218099  218100  218095    6921    6922    6924    6923
      92       3  218096  218100  218099  218094  218091    6924    6922  218090
    2764       3    5671    5714    5640    5637    5647    5690    5639    5638
    2765       3    5732    5689    5643    5646    5708    5665    5666    5709
    2766       3    5672    5715    5714    5671    5648    5691    5690    5647
    2767       3    5731    5688    5689    5732    5707    5664    5665    5708
    2768       3    5673    5716    5715    5672    5649    5692    5691    5648
    2769       3    5730    5687    5688    5731    5706    5663    5664    5707
    2770       3    5674    5717    5716    5673    5650    5693    5692    5649
```

C

Crossvalidation of the numerical models

In this appendix, the accuracy of both models at a certain point in the research is displayed. Based on these results the decision has been made to continue to work with one model.

Validation

The data from the physical model tests consists of wave-gauge data from several points in the wave flume. The distances between these points are known and therefore the wave speed can be determined. Velocity meters were also placed in the flume but in the turbulent waves, these measurements were not useful. During the physical model tests, the bottom was covered with grains of a particle size between 2 and 5mm. This results in a decrease in wave speed due to turbulence at the bottom. This phenomenon will be more significant if the water level is low.

Accuracy during the lab tests

When these models were made it was thought that the opening of the gate was 20 cm. The opening in reality, is 15 cm. Though the discussion still stands.

The opening of the gate is an important variable in the forming of the wave. This opening was 20 cm high and the gate should open this opening completely. When analyzing the videos in a later phase of the research it was discovered that the gate did not open this opening fully, it is not clearly visible how big this opening was during the tests, only estimates can be made. The difference of the opening thus the discharge through the opening results in other wave heights than expected by the model with an opening of 20cm.

Because it is not sure how large the opening exactly was in the tests at least the Numerical models are related as closely as possible to each other to make a distinction. The distance between the lowest and highest particle in the opening of the gate is set to 0.18m. With a particle size of 0.005, this corresponds to an opening of 0.185 m.

Inaccuracies in the numerical model

In the Dualsphysics SPH model, there is a gap between the boundary particles and the fluid particles. This causes the opening in the gate to be less than the 20cm which was applied in the physical model tests. Therefore the size of the opening underneath the gate is widened manually with 2 times the particle size.

Outcomes dualsphysics model

The dualsphysics results are shown in figures C.1 and C.10 for the case in which the water in the tank was 70cm and the water in the basin is 30cm. The animations show that the wave is propagating on a realistic way through the gate and on the slope. The wave shoals on the slope before it breaks on the flatbed.

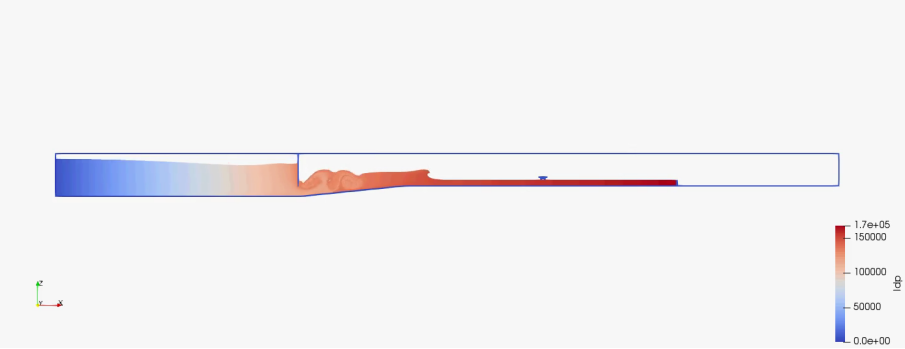

Figure C.1. Dualsphysics model overview

Figure C.2. Dualsphysics model zoom

From this animation is determined at what location the wave is breaking. The distance is determined on the moment that the first water particle in the wave hits the lower water level in front of the wave. In this Dualsphysics model, this happens at 1.5s at 0.84m from the top of the slope(WG1).

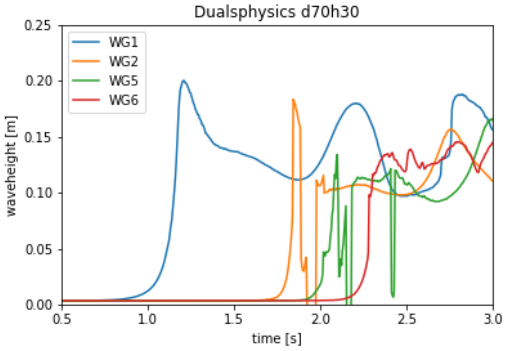

Figure C.3. Dualsphysics waveheight

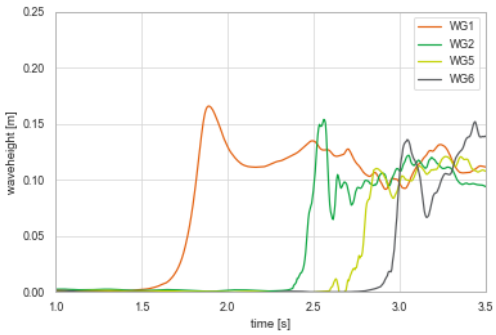

Figure C.4. Waseda waveheight

The maximum water height in the Dualsphysics simulation at the location of WG1 is 0.20 m, wave velocity between WG1 and WG2 is 2.28 m/s and the wave velocity between WG2 and WG5 is 2.16 m/s.

To compare the Dualsphysics model to the Waseda lab tests the times of the first wave peak are interpolated to see the changes in the wave propagation between the two cases. When plotted in the same window also the difference in wave height is easily observed.

The main observations that can be made are:

- Wave height in the Dualsphysics model is bigger than in the lab tests.

- Wave speed in the Dualsphysics model is larger, though it is logical that there is a higher wave speed in case there is a bigger wave height.

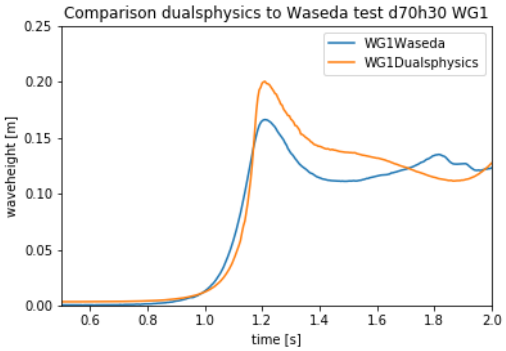

Figure C.5. WG1 comparison

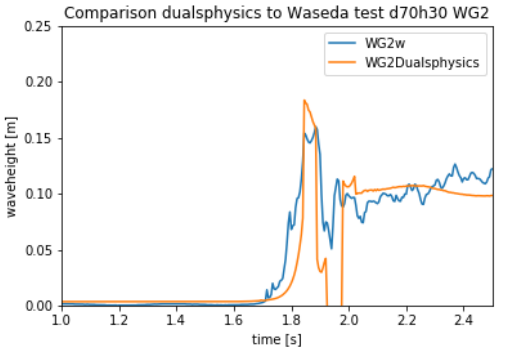

Figure C.6. WG2 comparison

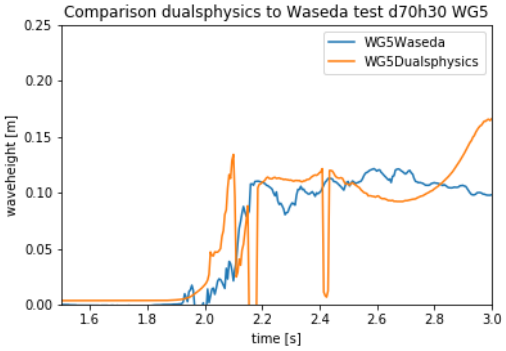

Figure C.7. WG5 comparison

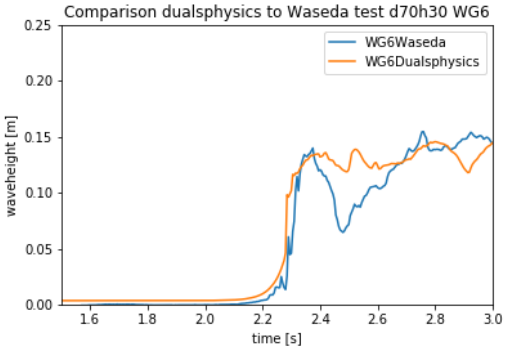

Figure C.8. WG6 comparison

Discussion

In the above graphs is clearly visible what the differences are between the lab tests and the numerical model. One clear difference is the wave height near WG1. A possible explanation is some inaccuracies in the model.

One insecurity as mentioned earlier is the difference in opening size in the gate. This has a direct effect at the discharge thus at the wave height and propagation speed of the wave.

In the Dualsphysics model, the first particles are not located at the bottom. The lowest particles on top of the false bottom are located 1 dp from this false bottom. This means that in reality the water level should be measured from 20cm +0.5 dp so the water level is 0.0025m lower in case of a dp of 0.005m.

Differences in the measurements can also occur while the graphs are constructed in different ways. In Dualsphysics the point is plotted in which the density in an area is 50% of the full density of the fluid, therefore it is assumed that this will be the free surface. In LS-Dyna the maximum z value of the particles is plotted per time step in which the x value is between 0.005 before or after the location of the wave-gauge.

The analysis of the validation has to be done carefully. Different wave characteristics account for varying 3D phenomena. In the d60h25 case is clearly visible that the final formed fluid flow is responsible for the failure of the deck. the depth (and velocity) of this flow is higher in the location of the bridge piers since the total flow area is smaller. Though in this case, it is interesting to see that the initial impact force is not responsible for the bridge failure.

Artificial parameters

Viscobound, the visco bound parameter is a multiplier of the viscosity to the boundaries. In the model, this phenomenon can be observed in a form that the fluid particles connected to the bounds have less movement across the boundary. Though no turbulence is formed in these areas. In the case of large particle size, this parameter has a larger influence than in the case of a bigger particle size, therefore it is hard to make use of this parameter in a proper manner.

Outcomes LS-Dyna model

The model which is constructed in the LSTC software LS-Dyna will be validated in this section.

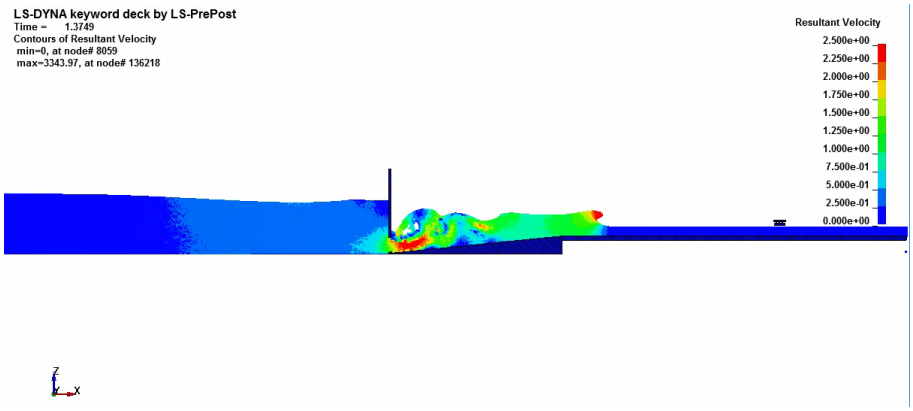

Figure C.9. LS-Dyna model overview

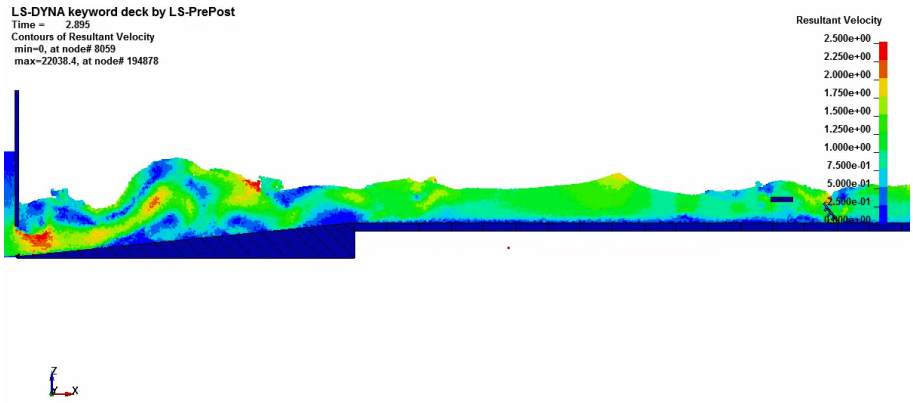

Figure C.10. LS-Dyna model zoom

From this animation is determined at what location the wave is breaking. The distance is determined on the moment that the first water particle in the wave hits the lower water level in front of the wave. In this model, this happens at 1.5s at 0.78m from the top of the slope(WG1).

Hydrodynamics of the model, in the figures below, an analysis is shown of the wave heights at multiple locations in the model. A visual analysis states that some processes of the 2D model do not represent reality. Directly after opening in the region behind the gate turbulence occurs in which air is visible in the whirls. In reality, some vacuums will occur and this will limit the size of water whirls. In future models, this can be counteracted with the use of two-phase modeling in which air particles can be modeled and air entrapment in the water will be accounted for.

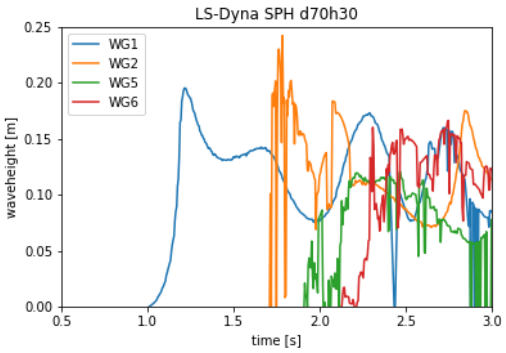

Figure C.11. LS-Dyna output

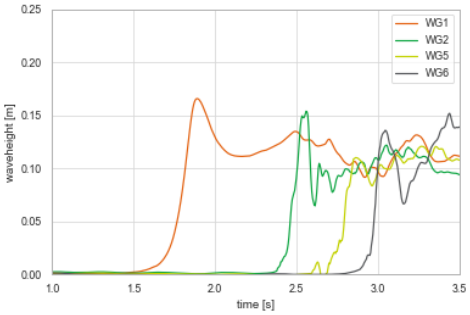

Figure C.12. Waseda output

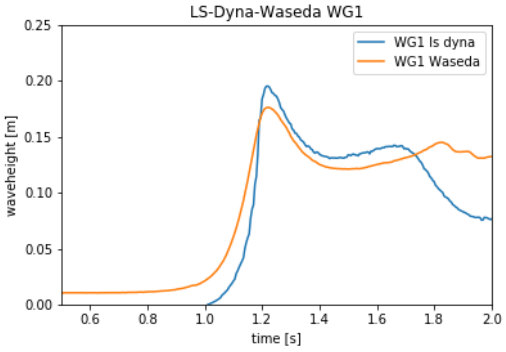

Figure C.13. WG1 comparison

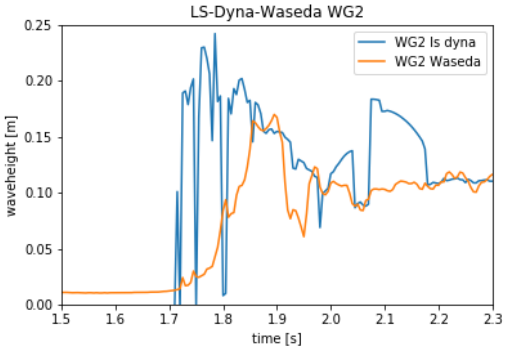

Figure C.14. WG2 comparison

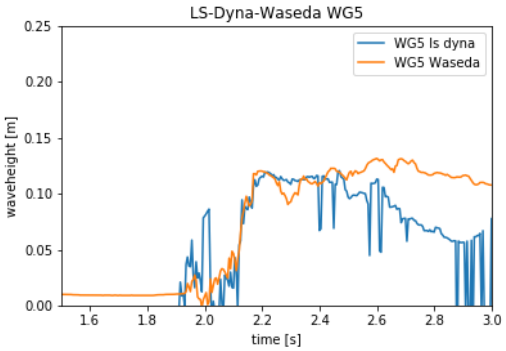

Figure C.15. WG5 comparison

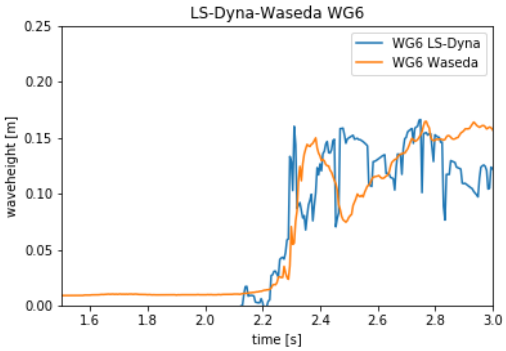

Figure C.16. WG6 comparison

In the LS-Dyna simulation, the maximum water level at the location of WG1 is 0.205m and the maximum water level at WG2 is 0.221m. The wave velocity between these wave gauges is determined on 2.68 m/s.

In figure C.20 in which the data for WG2 is displayed, the difference between the 2 lines is big. This is exactly the location where particles reach the highest level after the splash of the wave breaking. The water height data from the LS-Dyna model is extracted from the model in a way that the highest particle determines the water height in the model. In this timestep, there are some particles that reach higher points than the initial wave height due to splashing up after the breaking of the wave.

Comparisson SPH models

In this last section, the outcomes of the Dualsphysics and LS-Dyna model are compared.

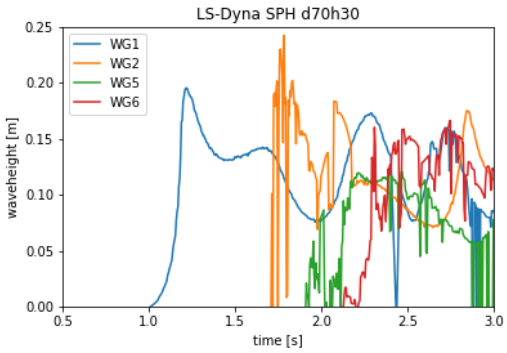

Figure C.17. LS-Dyna output

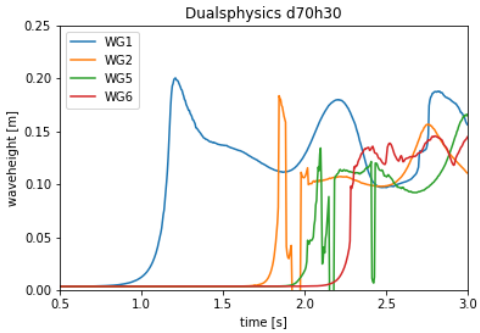

Figure C.18. Dualsphysics output

The data output from the LS-Dyna software is a bit noisier due to the different determination of the water height. Though the outcomes are pretty similar in both cases regarding the outcomes in the later wave gauges.

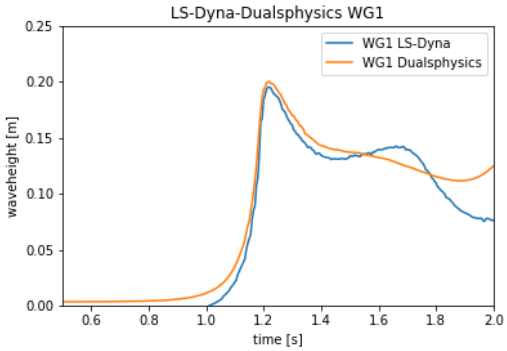

Figure C.19. WG1 comparison

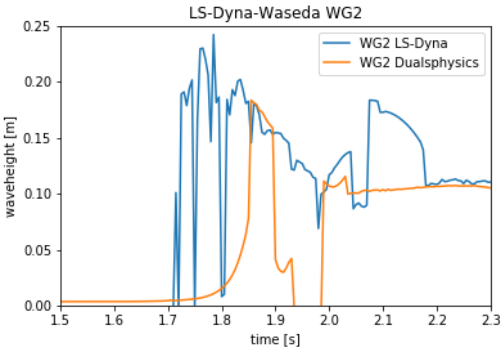

Figure C.20. WG2 comparison

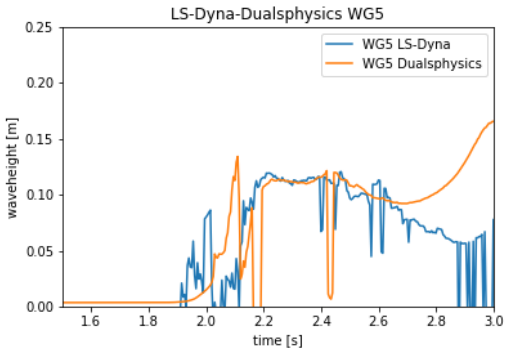

Figure C.21. WG5 comparison

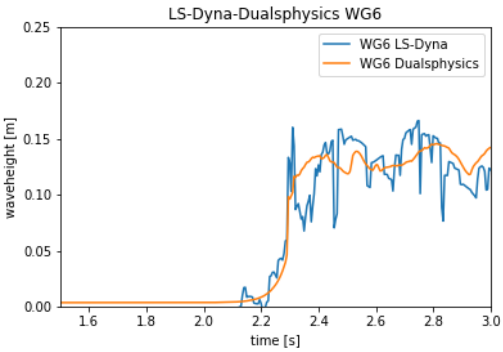

Figure C.22. WG6 comparison

Movement of the deck

The wave properties in the models are not 100% accurate, though when comparing the movement of the deck during the Waseda tests and in the LS-Dyna model, the similarities are remarkable. In LS-Dyna the deck is modeled as a rigid mesh and the contact friction between the deck and the pier which is determined in section 3.1.1 is applied. The density in the model is similar to the model tests.

Discussion regarding overall results

In this chapter, the exact same conditions are tried to be reproduced from both models. Both models have a particle distance of 0.005m. Both models have a viscosity multiplier near the bound of 10. The shape of the geometry is the same in both cases.

In LS-Dyna the gate has an opening of 18cm. In Dualsphysics this opening is 0.195cm with the gaps between the boundaries and the fluid the distance between the upper and lower particle in the gate is also 18cm.

A difference in both models is the setup of the geometry, while the shapes are the same in both the models. The boundaries are made of particles in the Dualsphysics model whereas it is constructed of solids in LS-Dyna. In LS-Dyna the boundary is a rigid body where no intrusion is possible in the solids. In Dualsphysics the boundary particles also have properties given to them. So the SPH principle also works between the boundary and the fluid particles.

A disadvantage of this is that the boundaries are constructed in a cartesian grid. Which as a consequence have a stepped slope. In LS-Dyna the slope is smooth.

There is also some difference in the definition of the equation of state (section 2.12.4) whereas in LS-Dyna there are given parameters for k_0 and γ are constants respectively $1.5 * 10^5$ and 7.0. In Dualsphysics the k_0 value is determined with respect to the speed of sound and the reference density (equations 2.59 and 2.60).

D

Scale model

Figure D.1. Yabitsu bridge [Oudenbroek, 2018].

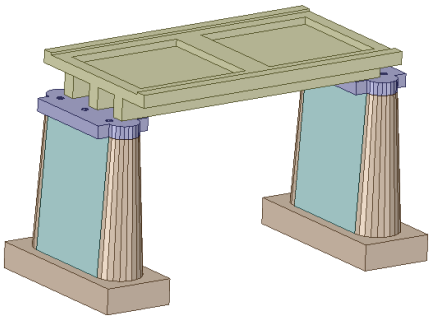

Figure D.2. Yabitsu bridge scale model.

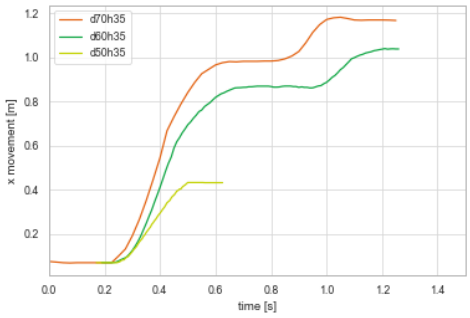

Figure D.3. Waseda lab tests varying d, h35 bridge x coordinate.

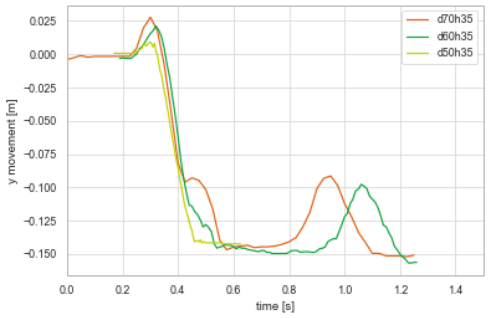

Figure D.4. Waseda lab tests varying d, h35 bridge y coordinate.

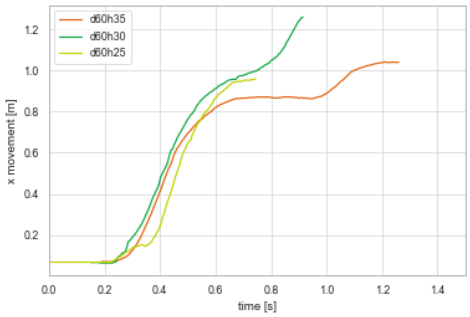

Figure D.5. Waseda lab tests d60hvary bridge x coordinate.

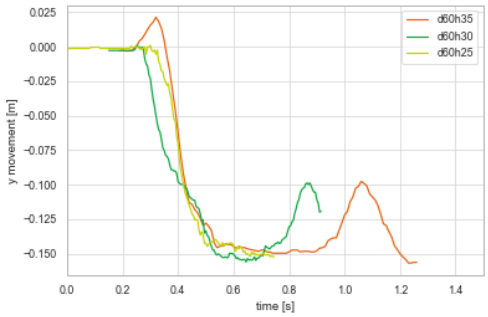

Figure D.6. Waseda lab tests d60hvary bridge y coordinate.

Table D.1. Dimensions of bridge model used in lab test and numerical simulation.

	Real bridge [mm]	1:37 scale model [mm]
Given dimensions		
length of a single deck segment	9400	254
Width of the road	4500	122
Height of a deck segment	1100	30
Estimated dimensions (deck)		
Width of the full deck	5273	143
Width of the deck sides	387	10
Height of a girder	695	19
Width of a girder	436	12
Distance between girder	843	23
Distance between girder and deck edge	1125	30
Height of the railing	700	19
Estimated dimensions (pier)		
Width of the foundation	2258	61
Height of the foundation	802	22
Minimum width of the base of the pier	1052	28
Maximum width of the base of the pier	1515	41
Height of the base of the pier	4362	118
Width of the top of the pier	1813	49
Height of the top of the pier	390	11
Average length of the pier	4500	122
Length of the foundation	5440	147

E

SPH additional figures

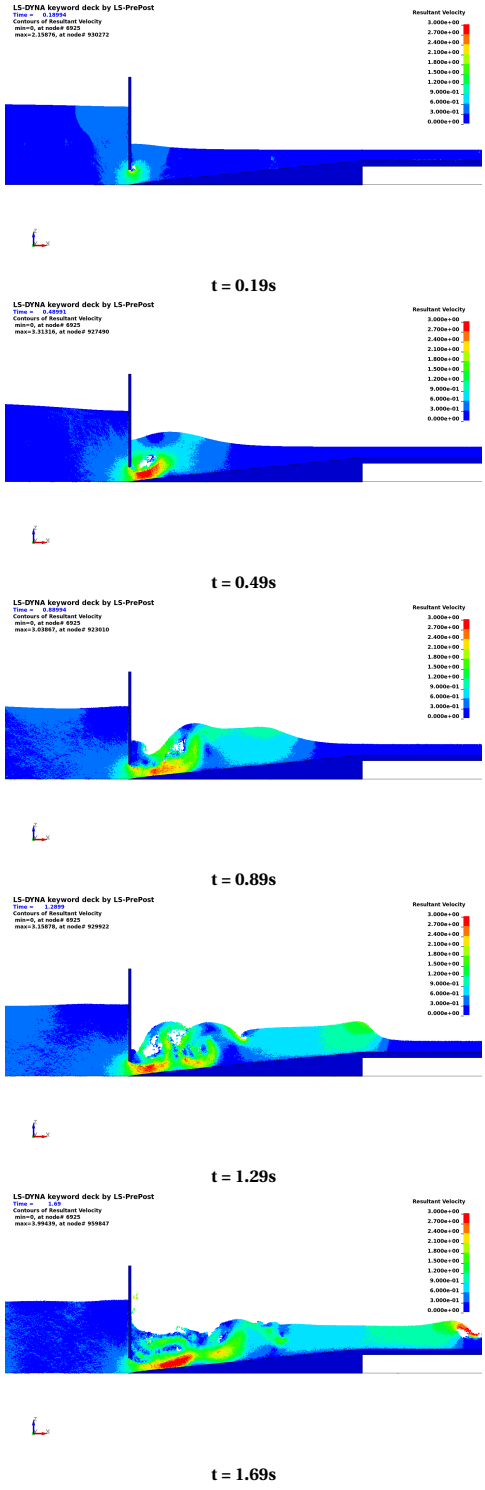

Figure E.1. Hydrodynamic behaviour in around the gateopening

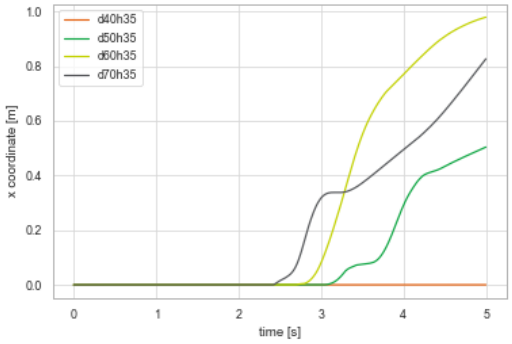

Figure E.2. X coordinates of deck for different tank heights.

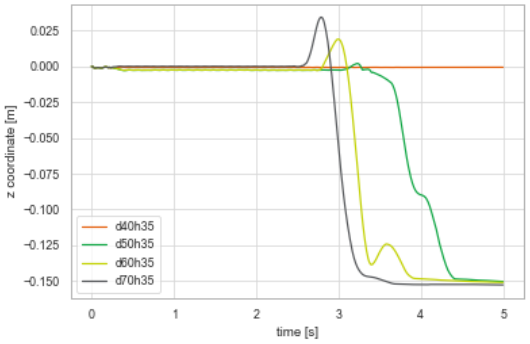

Figure E.3. Y coordinates of deck for different tank heights.

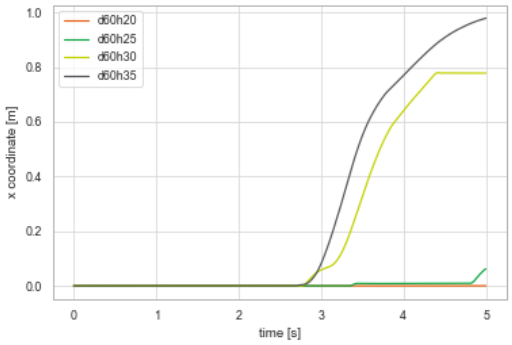

Figure E.4. x coordinates of deck for different basin heights.

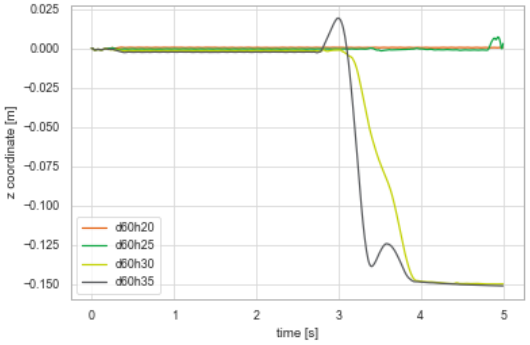

Figure E.5. y coordinates of deck for different basin heights.

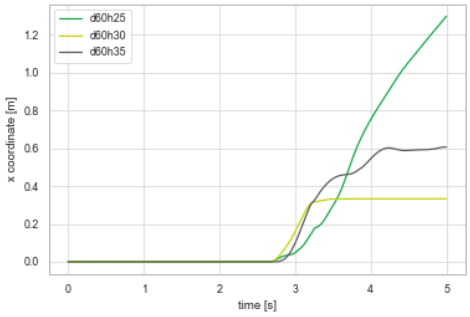

Figure E.6. x coordinates of deck with different basin heights with seawall.

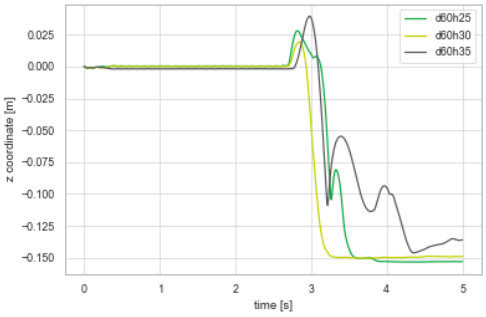

Figure E.7. y coordinates of deck with different basin heights with seawall.